Detection and Manipulation of Complex Electric and Magnetic Dipole Textures in Three- and Two-dimensional Crystals

by

Xiangpeng Luo

A dissertation submitted in partial fulfillment
of the requirements for the degree of
Doctor of Philosophy
(Physics)
in the University of Michigan
2024

Doctoral Committee:

Associate Professor Liuyan Zhao, Chair
Professor Steven T. Cundiff
Associate Professor John T. Heron
Associate Professor Robert Hovden
Professor Kai Sun

Xiangpeng Luo

xpluo@umich.edu

ORCID iD: 0000-0002-5471-053X

ACKNOWLEDGEMENTS

Throughout my PhD journey, no one has had a greater impact on me or provided more support than my advisor, Liuyan Zhao. From the very first summer day I stepped into her office in West Hall, I have from time to time felt that my academic accomplishments pale in comparison to the invaluable guidance and help she has given me. This reflection I hold at the current moment does not mean I feel any regret or disappointment about my past years, but rather deepens my appreciation of Liuyan as an outstanding mentor, both academically and personally. During my PhD course, her guidance was meticulous: from the details of preparing scientific figures to patiently showing me how to align lasers (after I ruined Wencan's whole setup!). She consistently maintained weekly discussions with me, despite her busy schedule filled with various meetings. I am deeply grateful for her unwavering support and the precious time she has devoted to mentoring me.

Consciously or not, I often strive to emulate Liuyan and learn from her as an excellent faculty member and scholar. In the Rackham annual PhD survey, I have always been particularly sensitive to the question: do you consider yourself more of a knowledge consumer or a knowledge producer? In the early years of my PhD, I consistently felt like a passive student. It was through numerous discussions with Liuyan and the various networking opportunities she supported me with that I began to feel like I was leaning towards the knowledge producer a bit in recent years. From her, I learned how to identify key features in messy data, how to be decisive when faced with multiple degrees of freedom, and even how to manage time to focus on the most critical tasks (something I am still learning for sure). It is commonly believed, that one of the most important tasks of a PhD advisor is to transform students into scholars. In this regard, Liuyan has been exceptional.

I am also extremely grateful to two other professors who have been crucial to my PhD research. Prof. Rui He and her research group consistently undertook the laborious and challenging low-temperature Raman measurements for us. Their diligence and dedication often left me in awe and feeling humbled. Many of the beautiful data in my work are a direct result of their contributions. Prof. Kai Sun has been involved in every aspect of my research. His extensive knowledge of condensed matter physics and his expertise in modeling with Mathematica have repeatedly impressed me. I vividly remember the discussions among

Liuyan, Kai, and myself in various settings—different platforms, offices, and even cities. As an experimental person myself, I feel each discussion with theorist Kai has been an enlightening experience that broadens my knowledge.

I would also like to thank my colleagues in the Zhao lab, a diverse group of outstanding researchers. Without their daily support and encouragement, my PhD experience would not have been as enjoyable. I particularly want to acknowledge Dr. Wencan Jin, who, despite my frequent interruptions (and sometimes disruptions), provided me with the most guidance in developing my initial experimental skills. I must also thank Dr. Hongchao Xie. Without his invaluable CrI3 samples, our two fruitful papers would not have been possible. Additionally, I am grateful to Xiaoyu Guo and Dr. Zeliang Sun. During the post-pandemic period and as friends gradually left, their companionship in both work and life has been a crucial source of motivation for me. I'd also like to extend my special thanks to other members of the group—Elizabeth Drueke, Rachel Owen, Siwen Li, Austin Kaczmarek, Youngjun Ahn, June Ho Yeo, Weizhe Zhang, and Suhan Son. I feel so fortunate to be able to work with this group of wonderful people.

This thesis is dedicated to all those who have supported me in every possible way, and to my beloved parents Jiabin Luo and Hua Xie, to whom I owe everything.

TABLE OF CONTENTS

CHAPTER

LIST OF FIGURES

LIST OF TABLES

ABSTRACT

This dissertation presents the research of complex ordered states—textures of electronic or magnetic dipoles—in crystalline solids, with a particular focus on the ferro-rotational charge density wave (CDW) and the non-collinear magnetic structures arising from Moiré engineering. Using a combination of advanced nonlinear, ultrafast optical spectroscopy and inelastic light scattering, this research provides novel insights into the dynamic and tunable properties of such orders in relevant quantum materials.

The first part of the dissertation investigates the ferro-rotational nature of the commensurate charge density wave (CCDW) in $1T$-TaS_2. We establish that a higher-order electric-quadrupole (EQ) second-harmonic generation (SHG) presents and its rotation anisotropy (RA) pattern senses the breaking of the mirror symmetry—a hallmark of the ferro-rotational order—due to the formation of the CCDW. With optical pumping, our experiments further reveal ultrafast modulations of this ferro-rotational CDW, characterized by the breathing and rotation of the EQ RA-SHG patterns at specific frequencies. These findings demonstrate the capability of nonlinear SHG coupling to the ferro-rotational CDW order as well as the dynamic control of it, and highlight the potential for photo-induced transient CDW phases, applicably expanding our understanding of multipolar orders in quantum materials.

In the following parts we present a multivarious optical study of the magnetic material CrI_3. We start by examining the magnetism in bulk CrI_3 using circularly polarized Raman Scattering. By revealing diverging antiferromagnetic (AFM) magnon branches in the known bulk ferromagnetism (FM), we propose a novel mixed state of layered AFM and bulk FM in this material. When polarizing the surface AFM into FM at a critical magnetic field, we also discover a first-order, rhombohedral-to-monoclinic structural phase transition by detecting

the symmetry change of exemplary phonons. Our results demonstrate the intricate interplay between magnetism and the crystalline structures in this material.

We then present the exploration of the complex magnetic orders in twisted double-bilayer CrI$_3$. The tunability of the layered-magnetism-assisted magneto-Raman phonons is first studied. We confirm the successful Moiré engineering in this system by showing a comprehensive twist angle dependence of such modes. By examining the magnetic field dependence, we also identify a novel magnetic ground state at an intermediate twist angle of 1.1°, which is distinct from natural untwisted four-layer or bilayer systems. Further with the help of the theoretical simulation, we propose the formation of non-collinear spin texture upon twisting as well as its twist angle dependence. By conducting the magnetic circular dichroism measurements and attributing the signal to collinear spin and non-collinear spin contributions, we experimentally demonstrate the maximum of both the non-collinearity and an emergent net magnetization at the intermediate twist angle. Such studies manifest the vast opportunities for exploring complex magnetic orders with Moiré engineering in two-dimensional magnets.

In conclusion, this dissertation advances the optical study of specific complex electronic and magnetic orders in 1T-TaS$_2$ and CrI$_3$, respectively. The findings have implications for both the future development, utilization of advanced optical probes, and the deeper understanding of complex orders together with the control or application of them.

CHAPTER 1

Introduction

In this chapter we briefly introduce "quantum materials" in the sense of contemporary condensed matter physics, with special focuses on the complex orders and properties of different materials studied in this thesis. Following the introduction, we will describe the overall organization of the thesis. The publications of the research conducted for this thesis are also listed at the end of this chapter.

1.1 Quantum materials

The field of "quantum materials" originated from condensed matter physics (formerly known as solid state physics) and has evolved into a multidisciplinary frontier [1]. This field has primarily been focusing on a broad class of materials and physics systems where electron correlation interactions are significant, or where certain form of electronic order (such as charge ordering or magnetic ordering) exists. It also includes systems exhibiting peculiar electronic properties due to the geometric phase of their wavefunctions (such as topological insulators and graphene-like Dirac electron systems), and other systems where macroscopic collective properties are governed by quantum behavior (such as ultracold atoms, superconductivity). A common characteristic of quantum materials is the phenomenon of "emergence", where the collective behavior of a many-body system composed of many individual units cannot be simply extrapolated from the properties of single particles [2]. At each level of complexity, new physical concepts, laws, and principles emerge, with the overall properties

far exceeding the physics of individual units. The core of quantum materials research is to study and utilize these cooperative phenomena that emerge in such many-body systems.

The concept of "quantum materials" is thus rapidly evolving in that sense. Its evolution can be traced back to the series of revolutionary discoveries in correlated electron materials that emerged in the 1980s, which set the direction for subsequent developments in the field of quantum materials. In the 1960s and 1970s, the main themes in solid state physics were to study different electronic ordered states within the framework of Landau-Fermi liquid theory [3, 4] and symmetry-breaking theory [5], using order parameters and correlation functions to describe various phases and their responses to external fields. This research paradigm persisted until the 1980s when two critical advancements—high-temperature superconductivity [6] and the (fractional) quantum Hall effect [7, 8]—challenged this classical framework and significantly stimulated interest in strongly correlated electron systems. Strong electron correlation refers to a significant scientific problem where the strong Coulomb repulsion between electrons in a system cannot be effectively simplified [9]. This is a natural scientific extension of the classical band theory and Landau-Fermi liquid theory frameworks. This is also why the concept of "quantum materials" initially appeared as a synonym for correlated electron systems. In recent years, with the findings of new emergent quantum phenomena in topological materials [10], low-dimensional materials [11, 12], and the explosive development in such fields, the scope of quantum materials has expanded from correlated electron systems to a much broader range of material systems [13–18]. The rapid deepening of understanding in systems represented by two-dimensional twisted bilayer graphene and three-dimensional topological insulators has made it increasingly clear that this broad and wide-ranging paradigm of "quantum materials" continues to call for both new material candidates and state-of-the-art experimental techniques.

1.2 Complex orders in quantum materials

Many of the phenomena observed in quantum materials reflect some specific kind of ordering of the system. As the building blocks of a system—say electrons in a crystalline solid—can have multiple degrees of freedom, there are several ways that a system can be ordered. For atoms, the simplest order is positional order, such that in a lattice atoms are not randomly positioned. If we associate the spin vectors with those spatially ordered atoms or ions we also observe magnetic orders. With the efforts in searching for universality or the organizing principles in many-body physics, thanks to Lev Landau, most of the so-called phases of matter can be mapped to corresponding orders, which are further described by order parameters and their symmetry properties [5, 19, 20]. From one phase to another, a spontaneous breaking of the continuous symmetry is necessarily accompanied by a bosonic excitation [21, 22]. In the presence of degenerate symmetry broken phases, gapped excitations such as defects or continuous textures can also appear as a consequence of the non-trivial topology in the order parameter space [23, 24]. A great number of new physical properties can be understood based on such considerations. Table 1.1 presents a few examples of them.

Phenomena	Broken symmetry	Elementary excitation	Topological defect
Crystallization	Translation	Phonon	Dislocation
Liquid crystal	Rotation	Nematic state	Disinclination
Superconductivity	U(1) gauge invariance	—[1]	Vortex
Charge crystallization	Translation	Amplitudon, phason	Discommensuration
(Anti-)Ferromagnetism	Time-reversal	Magnon	Domain wall
(Anti-)Ferroelectricity	Space inversion	Optical phonon	Domain wall

Table 1.1: Symmetry breaking examples in condensed matter physics.

The manifestation of an order can be complicated. For example, Fig. 1.1 considers the

---

[1]The excitation is gapped due to the Anderson-Higgs mechanism

transformation behavior of a vectorial order under space inversion (SI) or time reversal (TR) and lists four possible scenarios. Electric polarization $\mathbf{P}$ and magnetization $\mathbf{M}$ are common physical quantities studied in condensed matter physics. As a polar vector $\mathbf{P}$ is SI-odd and TR-even, while $\mathbf{M}$ is axial and thus SI-even. With a magnetic origin $\mathbf{M}$ must be TR-odd. Less common are those described in the second and four quadrants in Fig. 1.1. For a loop of joined polar vectors, they behave as both SI- and TR-even, whose transformation property is then the same as the cross product of two polar, TR-even vectors $\mathbf{r} \times \mathbf{P}$. For a loop of joined axial vectors however, it is both SI- and TR-odd, and transforms like $\mathbf{r} \times \mathbf{M}$.
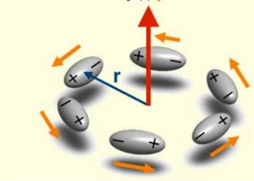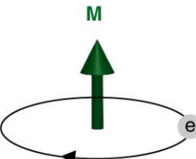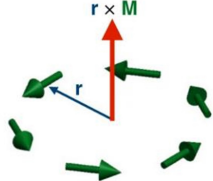
Figure 1.1: Categorizing vector order parameters with respect to time-reversal (TR) and spatial-inversion (SI) symmetries. Figure adapted from [25].

When a moment mentioned above forms and align together in every cell of the crystal, a ferroic order appears. Common examples are ferroelectricity with $\mathbf{P}$ as the order parameter, and ferromagnetism with $\mathbf{M}$ as the order parameter. With the help of their conjugate fields—electric field $\mathbf{E}$ for $\mathbf{P}$ and magnetic field $\mathbf{B}$ for $\mathbf{M}$—one can couple to those orders and explore their properties. But for the other two cases, where people define ferro-rotation or ferro-axis with order parameter transforming like $\mathbf{r} \times \mathbf{P}$, and ferro-toroid with order parameter transforming like $\mathbf{r} \times \mathbf{M}$, it becomes challenging to experimentally generate their

conjugate fields. As a matter of fact, the direct observations of the ferro-toroidal [26, 27] and ferro-rotational [25] orders in quantum materials did not occur until this century.

In [25], second-harmonic generation (SHG), a nonlinear process in which the frequency of light incident on the sample is doubled through its second-order nonlinear interactions, has been demonstrated to have the capability to couple to the ferro-rotational order. One notes that the transformation properties of the vector $\mathbf{r} \times \mathbf{P}$ can be described by the antisymmetric off-diagonal components of a second-rank, polar tensor, such as an electric quadrupole (EQ) tensor. Through the development of high-sensitivity, rotational-anisotropy (RA) SHG instrumentation, it becomes feasible to detect the SHG from higher-order multipolar (such as the EQ) radiations, even in spatial-inversion symmetry preserved phases. The EQ RA-SHG study on a ferro-rotational charge density wave (CDW) in $1T$-TaS_2 will be presented in Chapter 3.

Complex orders can also reside in magnetic materials, through a dispersed alignment of the magnetic moments in a possibly large magnetic unit cell. As shown in Fig. 1.2 there could be various types of orderings of spins that come with very different magnetic properties [28]. Simply in a ferromagnet (FM) we can use an overall magnetization vector to represent the ferromagnetic order. For an anti-ferromagnet (AFM) there are two spatially separated lattices with opposite magnetizations, both of which are needed to describe the order. Through the discovery the two-dimensional (2D) magnetic material [29] and the emergence of twistronics [30], the field has seen interest in creating and studying novel magnetic orders by introducing twist into simple FM or AFM films. The term moiré magnetism [18, 31] describes the versatile tuning of the magnetic exchange interaction leading to non-trivial spin textures. A thorough study on this topic in multiple forms of the CrI_3 system will be covered in Chapter 4 and 5.
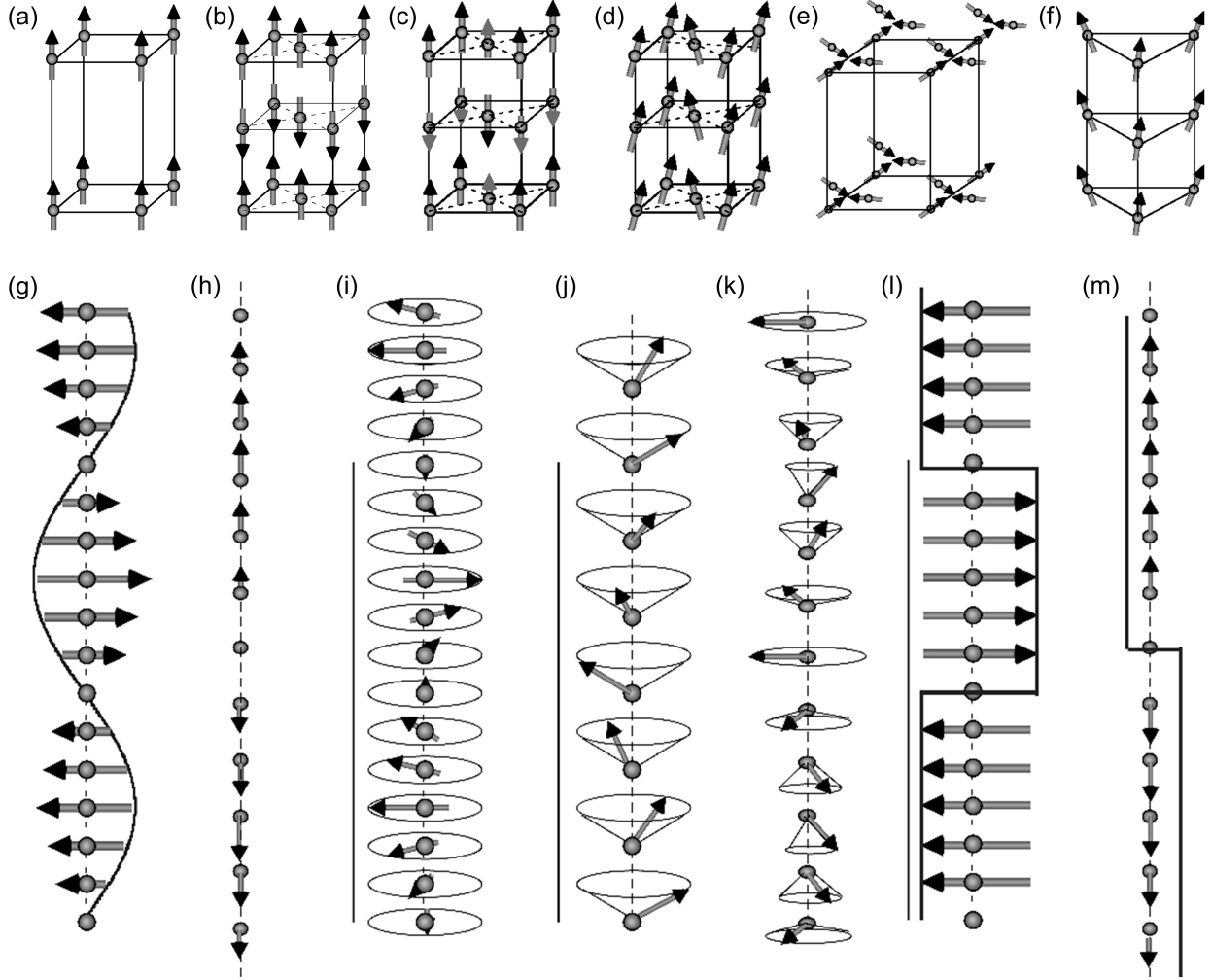
Figure 1.2: Schematics of ferromagnetic (a), antiferromagnetic (b), ferrimagnetic (c), canted ferromagnetic (d), triangular (e), umbrella (f), sinusoidally modulated (g) and (h), helical (i), conical (j), complex spiral (k), squared-up (l) and (m) orderings. Figure adapted from [28].

1.3 Outline of the thesis & publications

The outline for this work is as follows. Following this Introduction, Chapter 2 discusses the experimental optical techniques used for the research conducted for this thesis. Specifically, I will describe the principles of three optical probes: SHG, Raman Scattering, and magnetic circular dichroism (MCD), with an emphasis on the symmetry considerations in those optical measurements.

Chapter 3 studies the ferro-rotational CDW order in $1T$-TaS$_2$. I will firstly review the

CDW orders in $1T$-TaS$_2$ and explain the symmetry properties associated with the charge order. Then I demonstrate through temperature dependent RA-SHG that this CDW breaking mirror symmetry manifests itself as a rotation of the RA-SHG patterns. I then present the temporal dependence of full RA-SHG after optical pumping, realized in time-resolved (tr-) RA-SHG measurements. The ultrafast modulation of the CDW order is revealed and discussed.

Chapter 4 presents the magneto-Raman Scattering results of bulk CrI$_3$ with temperature and magnetic field dependence. I will show the magnon scattering data and through identifying three magnon branches, introduce our proposed coexistence of bulk FM and surface AFM orders in 3D CrI$_3$. I will also examine the magneto-phonon scattering, through which a magnetic field induced structural phase transition is revealed. By comprehending those phenomena from the strong magnetoelastic coupling in CrI$_3$, this chapter paves the way for realizing moiré engineering of the spin systems in twisted CrI$_3$ samples.

Chapter 5 provides a detailed exploration and characterization of moiré magnetism achieved in twisted double-bilayer (tDB) CrI$_3$ systems. For the first half of this study, I will begin by demonstrating the successfully moiré coupling in our tDB samples by TEM imaging the moiré superlattice. I then establish that the core of moiré engineering in spin systems is the stacking order dependent interlayer exchange interaction. With the help *ab*-inito calculations, a continuous distribution of such interlayer exchange interaction for the moiré interface is obtained. I then show our simulated, twist angle dependent magnetic ground states under this moiré engineered exchange interaction.

The second half of Chapter 5 is about the optical characterization of the moiré engineered magnetic states in tDB CrI$_3$ systems. I will revisit the magnetism-coupled phonon modes in Raman Scattering measurements and show how their intensity variation as well as the selection rule change can be utilized to understand the new layered magnetic order in tDB CrI$_3$. I then resort to the magnetic field dependent MCD measurements and propose a two-component fitting model to provide indicators for understanding the collinear and non-

collinear spins co-existing in moiré magnetism. Special emphasis is being put on the maximal prevalence of the non-collinear spin textures in tDB CrI_3 with intermediate twist angles.

The research presented in this thesis was performed under the supervision of my adviser Prof. Liuyan Zhao at the University of Michigan. This thesis reuses and reproduces content from the following published research papers with permission

[32] S. Li*, Z. Ye*, X. Luo*, G. Ye, H. H. Kim, B. Yang, S. Tian, C. Li, H. Lei, Adam W. Tsen, K. Sun, and L. Zhao. Magnetic-field-induced quantum phase transitions in a van der Waals magnet. *Physical Review X*, 10(1):011075, 2020.
Copyright © 2020 American Physical Society

[33] X. Luo, D. Obeysekera, C. Won, S. H. Sung, N. Schnitzer, R. Hovden, S. -W. Cheong, J. Yang, K. Sun and L. Zhao. Ultrafast modulations and detection of a ferro-rotational charge density wave using time-resolved electric quadrupole second harmonic generation. *Physical Review Letters*, 127(12):126401, 2021.
Copyright © 2021 American Physical Society

[34] H. Xie*, X. Luo*, G. Ye*, Z. Ye, H. Ge, S. H. Sung, E. Rennich, S. Yan, Y. Fu, S. Tian, H. Lei, R. Hovden, K. Sun, R. He, and L. Zhao. Twist engineering of the two-dimensional magnetism in double bilayer chromium triiodide homostructures. *Nature Physics*, 18(1):30–36, 2022.
Copyright © 2022 Springer Nature

[35] H. Xie*, X. Luo*, Z. Ye*, Z. Sun*, G. Ye, S. H. Sung, H. Ge, S. Yan, Y. Fu, S. Tian, H. Lei, K. Sun, R. Hovden, R. He, and L. Zhao. Evidence of non-collinear spin texture in magnetic moiré superlattices. *Nature Physics*, 19(8):1150–1155, 2023.
Copyright © 2023 Springer Nature

CHAPTER 2

Techniques

2.1 Second-harmonic generation (SHG)

2.1.1 SHG as lowest-order nonlinear optics

Optical response of a material can be most generally described by a response function, in which the incident electric field $E(t)$ generates a electric dipole (ED) $P(t)$ through $P(t) = \varepsilon_0 \chi E(t)$. In this formalism, without further assumptions on the susceptibility χ, a time harmonic incident wave of $\mathrm{e}^{-\mathrm{i}\omega t}$ with frequency ω will induce a polarization that is also oscillating with frequency ω. Radiation theory states that this polarization will then create reflected electromagnetic wave that is of the same frequency. Many optical phenomena not involving the significant change of frequency can be understood with this framework, including transmission, reflection, birefringence, and even quasi-elastic Rayleigh scattering.

In non-linear optics, the above relation is usually generalized by including a power series expansion with respect to the incident field [36]

$$P(t) = \varepsilon_0 \chi^{(1)} E(t) + \varepsilon_0 \chi^{(2)} E^2(t) + \varepsilon_0 \chi^{(3)} E^3(t) + \cdots \tag{2.1}$$

In the equation above, the terms on the right hand side will each have $\mathrm{e}^{-\mathrm{i}\omega t}$, $\mathrm{e}^{-2\mathrm{i}\omega t}$, $\mathrm{e}^{-3\mathrm{i}\omega t}$, ... phase factors, which essentially represent dipoles that are oscillating with ω, 2ω, 3ω, ... frequencies. This indicates that they will radiate light at harmonic frequencies of the funda-

mental light. For this reason, the process from the second term $\varepsilon_0 \chi^{(2)} E^2(t)$ corresponding to the creation of light with double fundamental frequency is called second-harmonic generation. Similarly the term $\varepsilon_0 \chi^{(3)} E^3(t)$ will give third-harmonic generation (THG).

The harmonic generation can be firstly understood from a classic perspective. Start with an electron residing in a potential with $\sim \omega_0 x^2$ dependence, namely a harmonic potential well. If we drive it with an electric field of $\sim E\mathrm{e}^{-\mathrm{i}\omega t}$, this is essentially a Lorentz oscillator model, or forced vibration [37]. Its steady state solution is no more than a harmonic vibration with frequency ω, and no other frequencies are expected. Thus up to the dipole solution $P(t) \propto x(t)$, harmonic potential does not allow the SHG or THG process. It is the inclusion of a non-harmonic potential such as terms like $\sim x^3$ that will give higher-order frequency components, as can be seen from the Fourier transform of the dynamic equation. This is saying that the non-harmonic potential is the origin of the high-harmonic generations. Specifically, potential correction terms like $\sim x^3$ is responsible for SHG, and terms like $\sim x^4$ for THG.

This classical understanding already implies a few important features for SHG/THG processes. First, the correction for the potential becomes needed when the electron is pulled far enough from its equilibrium position. For an estimation, this would occur when the strength of the incident electric field is comparable to that of the atomic electric field [38]

$$E_{\mathrm{atom}} = \frac{e}{4\pi\varepsilon_0 a_0^2} = 6 \times 10^{11} \mathrm{V/m} \tag{2.2}$$

where a_0 is the Bohr radius. This electric field corresponds to an intensity of $\frac{1}{2}\varepsilon_0 c E_{\mathrm{atom}}^2 = 4 \times 10^{16}$ W/cm^2, therefore very intense light is needed to observe the high-harmonic generation. In this sense femto-second pulsed lasers serve as the best equipment for generating high-harmonic radiation. Secondly, in a centrosymmetric environment the potential does not allow odd terms like $\sim x^3$. This means ED SHG should not be present in centrosymmetric materials. This is the most prominent feature of ED SHG. Meanwhile, it is known that

10

the surface of a crystal will modify the potential landscape and introduce significant non-harmonic corrections [39]. Therefore one would expect ED SHG from the surface of a sample. This feature can also be understood in the sense that a surface always lacks centrosymmetry. In light of such considerations, we can incorporate more detailed symmetry analysis in a SHG measurement.

2.1.2 Applying symmetry on SHG susceptibility tensors

Noting the vector nature of electric polarization and the electric field, the appropriate way to write down, for example the ED SHG process, must take the tensor notation into account

$$P_i = \chi_{ijk}^{(2),\text{ED}} E_j E_k \tag{2.3}$$

where $\chi_{ijk}^{(2),\text{ED}}$ is a third-rank tensor, and the summation over repeating indices like j and k in this equation is always understood within this section. With the help of those indices, the tensor $\chi_{ijk}^{(2),\text{ED}}$ can inherit symmetry information. This will be briefly explained in the following.

Firstly, one examines how the tensor transforms under a symmetry operation. This is done by noting that, apart from the frequency-doubling dynamics behind Eq. (2.3), this notation also explicitly defines the transformational property of the tensor $\chi_{ijk}^{(2),\text{ED}}$ through its relation with **P** and **E**. Note **P** and the two copies of **E** all transform like a polar (namely SI-odd) and TR-even vector: $P_i' = R_{ii'} P_{i'}$ and $E_i' = R_{ii'} E_{i'}$. Their transformation behavior is denoted as V using the Jahn symbol [40]. Then according to the definition of the tensor $\chi_{ijk}^{(2),\text{ED}}$ in Eq. (2.3), it must transform as

$$\chi_{ijk}'^{(2),\text{ED}} = R_{ii'} R_{jj'} R_{kk'} \chi_{i'j'k'}^{(2),\text{ED}} \tag{2.4}$$

which is then called V3. Here matrix R_{ij} denotes a general transformation matrix defined on a V tensor (that is, a TR-even polar vector). Also in Eq. (2.3) the two electric fields represent

the same incident field, therefore one would require indices j and k to be commutable. This changes the Jahn symbol of $\chi_{ijk}^{(2),\text{ED}}$ to V[V2], where $[\cdot]$ means the indices inside are symmetric.

In condensed matter physics, we usually deal with point group symmetries. The corresponding symmetry operations only involve improper and proper rotations. Noting that any improper rotations can always be treated as inversion times a proper rotation, we can express any transformation matrix R_{ij} in terms of a rotation matrix. For a general proper rotation, about an axis given by a unit vector $\mathbf{k}$ with a rotation angle φ, the rotation matrix is given by the Rodrigues' formula [41]

$$R(\mathbf{k}, \varphi) = I + \sin\varphi K + (1 - \cos\varphi)K^2, \quad \text{where } K = \begin{bmatrix} 0 & -k_z & k_y \\ k_z & 0 & -k_x \\ -k_y & k_x & 0 \end{bmatrix} \quad (2.5)$$

Suppose if the system to study has G point group symmetry. Then we could apply, for each symmetry operation $g \in G$

$$\begin{aligned} \chi'^{(2),\text{ED}}_{ijk} &= R(g)_{ii'}R(g)_{jj'}R(g)_{kk'}\chi^{(2),\text{ED}}_{i'j'k'} \\ &= \chi^{(2),\text{ED}}_{ijk} \end{aligned} \quad (2.6)$$

By associating the equations for all i, j, k and $g \in G$, we can reach a succinct form of tensor $\chi_{ijk}^{(2),\text{ED}}$. In practice, the TENSOR application in Bilbao Crystallographic Server [40] provides an convenient automated algorithm to obtain the final tensor form when feeding it with a point group and the transformation property (in Jahn symbol).

2.1.3 Multipolar radiation in SHG

The light-matter interaction is not limited to inducing dipoles. When light travels in a medium, it can create higher-order multipoles that radiate. The radiation of light can be understood from the following general wave equation, obtained by eliminating $\mathbf{B}$ and $\mathbf{H}$ in

Maxwell's equations [42]

$$\nabla^2 \mathbf{E} - \mu \varepsilon_S \frac{\partial^2}{\partial t^2} \mathbf{E} - \boldsymbol{\nabla}(\boldsymbol{\nabla} \cdot \mathbf{E}) = \mathbf{S} \tag{2.7}$$

where on the right hand side, the source term can be expressed up to the second-order multipoles [43]

$$\mathbf{S} = \mu \frac{\mathrm{d}^2 \mathbf{P}}{\mathrm{d}t^2} + \mu \boldsymbol{\nabla} \times \frac{\mathrm{d}\mathbf{M}}{\mathrm{d}t} - \mu \boldsymbol{\nabla} \frac{\mathrm{d}^2 \tilde{\mathbf{Q}}}{\mathrm{d}t^2} \tag{2.8}$$

We note that the ED contribution $\propto \mathbf{P}$ is typically λ/a times stronger than the following magnetic dipolar (MD) contribution $\propto \mathbf{M}$ and EQ contribution $\propto \tilde{\mathbf{Q}}$ terms [44], where λ is the incident light wavelength and a is the multipole length scale. For studying crystallined solids a is the lattice constant and with a visible light wavelength λ/a is roughly 10^3. Therefore when ED is allowed it usually dominates in the scattered light.

However, in a centrosymmetric material where an ED is forbidden by the presence of inversion, EQ radiation becomes the leading order contribution (in the absence of magnetism) to SHG, the process of which is given in analogy to Eq. (2.3) by

$$S_i \propto \chi_{ijkl}^{(2),\mathrm{EQ}} E_j \partial_k E_l \tag{2.9}$$

For symmetry considerations only, we have omitted the constant coefficients. Now we have a fourth-rank SHG susceptibility tensor which transforms as V2[V2]. With monochromatic plane incident wave we can further replace $\boldsymbol{\partial}$ by the wavevector $\mathbf{k}$. With those vectors being specified and the symmetry-adapted susceptibility tensor form obtained, we can associate the SHG models in Eqs. (2.3) or (2.9) with actual SHG RA measurements performed in the following geometry.

2.1.4 SHG RA experimental geometry

Figure 2.1(a) illustrates the typical geometry for an oblique incident SHG RA measurement. The term RA essentially describes an "angular" scan of the SHG intensity: recording

the SHG intensity as a function of the azimuth angle ϕ of the scattering plane on the sample surface. With respect to each instantaneous angular position of the reflection plane, parallel (P) and perpendicular (S) polarizations are defined for both the incident fundamental and the reflected SHG light. Then the SHG intensity in four different polarization channels—S_{in}-S_{out}, S_{in}-P_{out}, P_{in}-S_{out} and P_{in}-P_{out}—are measured. At the end of a measurement four curves of $I^{SHG}(\phi)$ are obtained. In the special case of normal incidence shown in Fig. 2.1(b), S_{in}-S_{out} versus P_{in}-P_{out}, and S_{in}-P_{out} versus P_{in}-S_{out} datasets would only differ by a rotation of 90°. In this sense only two polarization channels—parallel ($\parallel$) and crossed ($\perp$)—are needed to access the full RA information.
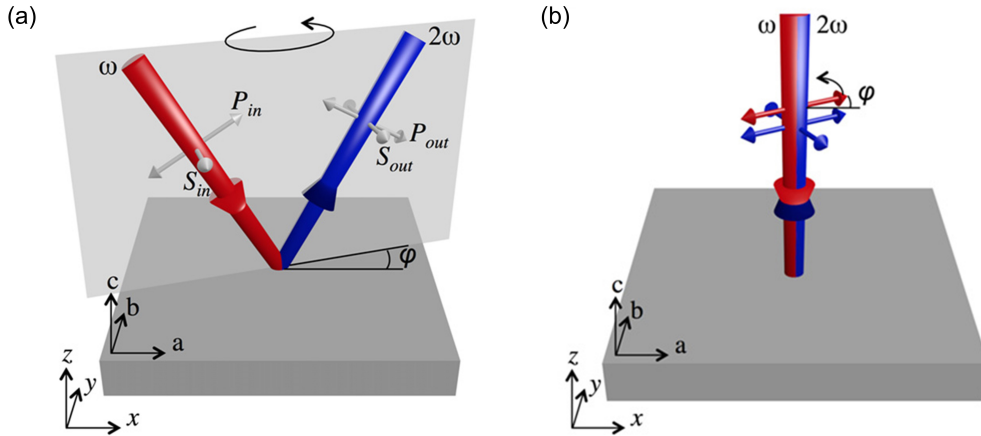
Figure 2.1: Schematic of the geometry of SHG RA measurements with oblique (a) and normal (b) incidence. Figure adapted from [45]

We establish the connection between this geometry and the models in Eqs. (2.3) or (2.9). Firstly we build up the lab coordinate system x-y-z affixed to the sample with z-direction being the surface normal. Then we specify the point group of the sample and obtain the symmetry-adapted SHG susceptibility tensor form. This tensor is almost always defined in its own lattice coordinate system a-b-c. In the case where the coordinate system a-b-c does not align with x-y-z, we perform three Euler rotations to align them up [41]. The associated rotation matrices for the Euler rotations must then be applied to the SHG susceptibility tensor as described in Eq. (2.4) for ED SHG tensors or in a similar fashion for EQ tensors.

14

This way we obtain a symmetry-adapted tensor form with local x-y-z coordinates. Then, taking S_{in}-P_{out} as an example, one can write down the vectors $\hat{s}_{in}$ and $\hat{k}_{in}$ as functions of ϕ in the x-y-z system, and replace the $\mathbf{E}$ and $\boldsymbol{\partial}$ vectors in Eqs. (2.3) or (2.9) with them, respectively. The $\mathbf{S}$ vector, essentially the electric field vector of the reflected SHG, is thus obtained. We then dot product it with $\hat{\mathbf{p}}_{out}$ and take the modulus square, to get the final $I_{SP}^{SHG}(\phi)$ function, with symmetry information embedded. By fitting the experimental data with this function, we can examine the proposed symmetry of the studied system. An example of this simulation in presented in the study of $1T$-TaS_2 in Chapter 3.

2.2   Raman spectroscopy

Raman scattering is an inelastic process of light scattered by the excitations in a medium [46]. Its inelastic essence can be readily understood by its quantum description. During a Raman process, an incident photon excites the electron into a virtual intermediate state. Instead of a real excited state which tends to fully absorb the light, the virtual state is short-lived such that the excited electron quickly transits back to a low-energy state by the emission of a new photon. This new state could be of higher energy than the original state, for which the emitted photon must possess less energy than the incident one. This is called a Stokes process. The opposite situation can also occur where the electron transits back to an even lower energy state, emitting a photon with larger energy than the incident one. This is called an anti-Stokes process. For a given excited state and the ground state, the existence of those two processes indicates that a pair of peaks symmetric with respect to the elastic reflection (referred to as the Rayleigh line) will appear in the Raman spectrum. They correspond, however, to the very same energy of that excitation.

Apart from the energy information, Raman Scattering measurements are usually conducted with controlled polarizations. Namely similar to SHG measurements explained in the previous section, the Raman spectrum is obtained with given polarizations of the inci-

dent and scattered light. In a similar fashion, this will give symmetry information of the system studied. In this section we present deduction for the differential cross section of Raman Scattering, with a special emphasis on the symmetry properties.

2.2.1 Cross section of Raman Scattering

Similar to the discussion in Section 2.1.1, a plain dispersion relation $P = \varepsilon_0 \chi E$ does not predict the change of frequency if the system's response χ does not have a frequency dependence. To create inelastic scattering, one assumes for an incident light $\mathbf{E} \sim \mathrm{e}^{-\mathrm{i}\omega_I t}$

$$
\begin{aligned}
\mathbf{D} &= \big[\varepsilon + \varepsilon_0 \alpha(\omega_I, \omega)\big]\mathbf{E} \\
&= \varepsilon_0\mathbf{E} + \underbrace{\varepsilon_0\chi\mathbf{E}}_{\mathbf{P}} + \underbrace{\varepsilon_0\alpha(\omega_I, \omega)\mathbf{E}}_{\mathbf{P}_{\mathrm{sc}}}
\end{aligned}
\tag{2.10}
$$

where $\varepsilon_0\alpha(\omega_I, \omega)$ represents a perturbative correction of the susceptibility of the medium [46], in the presence of a spatially and temporally modulating mode with frequency ω.

The induced dipole $\mathbf{P}_{\mathrm{sc}}$ thus carries the additional frequency of ω and radiates. The wave equation for this is essentially the same as Eq. (2.7)

$$
\nabla^2\mathbf{E} - \mu\varepsilon\frac{\partial^2}{\partial t^2}\mathbf{E} - \boldsymbol{\nabla}(\boldsymbol{\nabla}\cdot\mathbf{E}) = \mu\frac{\partial^2}{\partial t^2}\mathbf{P}_{\mathrm{sc}}
\tag{2.11}
$$

We would assume the scattered light is transverse and get rid of the third divergence term on the left hand side of Eq. (2.11). What is left is essentially an inhomogeneous Helmholtz equation, the solution of which is give by [47]

$$
\mathbf{E}(\mathbf{r}, t) = -\frac{\mu}{4\pi}\int\frac{\mathrm{d}^3r'}{|\mathbf{r}-\mathbf{r}'|}\left[\frac{\partial^2}{\partial t'^2}\mathbf{P}_{\mathrm{sc}}(\mathbf{r}', t')\right]_{\mathrm{ret}} + \mathbf{E}_0(\mathbf{r}, t)
\tag{2.12}
$$

where $[\cdot]_{\mathrm{ret}}$ denotes the retarded time and $\mathbf{E}_0$ is the general solution to the homogeneous version of Eq. (2.11). The general solution describes merely the propagation of the unscattered light and is not of our interest. To proceed we switch to the frequency domain by

substituting

$$\mathbf{P}_{sc}(\mathbf{r}',t') = \mathbf{P}_{sc}(\mathbf{r}',\omega_S)e^{-i\omega_S t'} \tag{2.13}$$

$$\mathbf{E}(\mathbf{r},t) = \mathbf{E}(\mathbf{r},\omega_S)e^{-i\omega_S t} \tag{2.14}$$

into Eq. (2.12) where the scattered light frequency $\omega_S = \omega_I \pm \omega$. After some calculation we would arrive at the scattering amplitude

$$\mathbf{E}(\mathbf{r},\omega_S) = \frac{\omega_S^2}{4\pi\varepsilon c^2}\frac{e^{ik_S r}}{r}\int e^{-i\mathbf{k}_S\cdot\mathbf{r}'}\mathbf{P}_{sc}(\mathbf{r}',\omega_S)\mathrm{d}^3 r' \tag{2.15}$$

With the scattering amplitude expression we can write down the energy flux after selecting it with a polarizer at $\hat{\mathbf{e}}_S$

$$
\begin{aligned}
I_S &= \frac{1}{2}\varepsilon\frac{c}{n}\left\langle \left|\hat{\mathbf{e}}_S\cdot\mathbf{E}(\mathbf{r},\omega_S)\right|^2\right\rangle \\
&= \frac{\varepsilon cV}{2nr^2}\left(\frac{\omega_S^2}{4\pi\varepsilon c^2}\right)^2\int e^{i\mathbf{k}_S\cdot(\mathbf{r}_1-\mathbf{r}_2)}\left\langle\left[\hat{\mathbf{e}}_S\cdot\mathbf{P}_{sc}^*(\mathbf{r}_1,\omega_S)\right]\left[\hat{\mathbf{e}}_S\cdot\mathbf{P}_{sc}(\mathbf{r}_2,\omega_S)\right]\right\rangle\mathrm{d}^3(r_1-r_2)
\end{aligned}
\tag{2.16}
$$

where the angular brackets $\langle\cdot\rangle$ represent an average over fluctuations. In obtaining the second line above, the translational invariance of the system is assumed. Similarly we have the incident energy flux

$$I_I = \frac{1}{2}\varepsilon_I\frac{c}{n_I}|\mathbf{E}_I|^2 \tag{2.17}$$

Thus we obtain the differential cross section from

$$
\begin{aligned}
\frac{\mathrm{d}^2\sigma}{\mathrm{d}\Omega\mathrm{d}\omega_S} &= r^2\frac{I_S/\hbar\omega_S}{I_I/\hbar\omega_I} \\
&= \frac{\omega_I\omega_S^3 nV}{(4\pi\varepsilon_I c^2)^2 n_I|\mathbf{E}_I|^2}\int e^{i\mathbf{k}_S\cdot(\mathbf{r}_1-\mathbf{r}_2)} \\
&\quad \left\langle\left[\hat{\mathbf{e}}_S\cdot\mathbf{P}_{sc}^*(\mathbf{r}_1,\omega_S)\right]\left[\hat{\mathbf{e}}_S\cdot\mathbf{P}_{sc}(\mathbf{r}_2,\omega_S)\right]\right\rangle\mathrm{d}^3(r_1-r_2)
\end{aligned}
\tag{2.18}
$$

17

2.2.2 Raman tensors and Raman selection rules

We now correlate the additional electric susceptibility, or Raman polarizability, α in Eq. (2.10) with the quasi-particles in the crystal. First we retrieve the two subscript indices for α_{ij} (just like a susceptibility tensor) which have been omitted in the previous section for a succinct look of the derivation. Then we represent an excitation that is responsible for α_{ij} by a general dynamic variable $X(\mathbf{r}, t)$. We seek to expand the Raman polarizability in a power series of the excitation

$$\alpha_{ij} = \alpha_{ij}\big|_0 + \frac{\mathrm{d}\alpha_{ij}}{\mathrm{d}X}\bigg|_0 X + \cdots \tag{2.19}$$

The first term on the right hand side above only gives a homogeneous correction to the general susceptibility χ in Eq. (2.10) and does not incur inelastic scattering. Plugging the second term and the relation between $\mathbf{P}_{\mathrm{sc}}$ and α_{ij} into the cross section in Eq. (2.18), finishing the spatial Fourier transform we have

$$\frac{\mathrm{d}^2\sigma}{\mathrm{d}\Omega\mathrm{d}\omega_S} = \frac{\varepsilon_0^2\omega_I\omega_S^3 nV}{(4\pi\varepsilon_I c^2)^2 n_I}\left|\hat{\mathbf{e}}_S \cdot \frac{\mathrm{d}\tilde{\boldsymbol{\alpha}}}{\mathrm{d}X} \cdot \hat{\mathbf{e}}_I\right|^2 \left\langle X(\mathbf{q}, \omega)X^*(\mathbf{q}, \omega)\right\rangle \tag{2.20}$$

The equation above reveals important features for a Raman measurement. Firstly, it is seen that the scattering intensity is proportional to the susceptibility derivative $(\mathrm{d}\tilde{\boldsymbol{\alpha}}/\mathrm{d}X)^2$. In this sense the Raman intensity proves a measure of how strongly the excitation modulates the susceptibility. Secondly, from the perspective of symmetry, the product between $\hat{\mathbf{e}}_S$, $\hat{\mathbf{e}}_I$, and the derivative $\mathrm{d}\tilde{\boldsymbol{\alpha}}/\mathrm{d}X$ which we shall call a Raman tensor gives a scaler, which must be invariant under the symmetry operations of the system. With the language of group theory, this scaler must transform as the trivial irreducible representation (irrep) Γ_1. To make this happen the Raman tensor must transform as an irrep Γ that is contained in the decomposition of $\Gamma_V^* \otimes \Gamma_V$, where Γ_V is the representation for a SI- and TR-even vector such as $\hat{\mathbf{e}}_{S,I}$.

In light of the second observation, for a given point group symmetry where Γ_V is known, the allowed forms of the Raman tensor are limited. The complete collection of all the possible Raman tensors for 32 point groups can be found in, for example, the Bilbao Crystallographic Serve [48]. Generally, by varying the combination of $\hat{\mathbf{e}}_{S,I}$ one can implicitly access the form of the Raman tensor for a given mode, and thus the possible point group symmetry of the system. Or the other way around, with a known mode one specifically choose the polarization channel to maximize the its Raman intensity for better observation. Both philosophies will be used in the later Raman studies of the CrI_3 systems in Chapter 4 and 5.

2.3 Magnetic circular dichroism

In this section I will briefly review light propagation in anisotropic materials [49, 50]. The main goal in this section is to prove in the system like CrI_3 with an out-of-plane magnetic order, the circular dichroism signal is proportional to the M_z component.

We start with the wave equation with an anisotropic permittivity tensor ε_{ij}. Note at optical frequency the permeability μ can always be treated as isotropic or a pure number [51]. For a monochromatic plane wave $\mathbf{E}, \mathbf{H} \sim e^{i(\mathbf{k}\cdot\mathbf{r}-\omega t)}$, the two inhomogeneous Maxwell's equations can be written as

$$\mathbf{k} \times \mathbf{E} = \omega\mu\mathbf{H} \tag{2.21}$$

$$\mathbf{k} \times \mathbf{H} = -\omega[\epsilon]\mathbf{E} \tag{2.22}$$

By eliminating $\mathbf{H}$ from the two equations we obtain

$$\mathbf{k} \times (\mathbf{k} \times \mathbf{E}) + \omega^2\mu[\varepsilon]\mathbf{E} = \mathbf{k}(\mathbf{k} \cdot \mathbf{E}) - k^2\mathbf{E} + \omega^2\mu[\varepsilon]\mathbf{E} = 0 \tag{2.23}$$

Note different from the free space case we cannot assume $\mathbf{k} \cdot \mathbf{E} = 0$. This is because in the presence of a tensor form $[\varepsilon]$, the Gauss's law $\mathbf{k} \cdot \mathbf{D} = \mathbf{k} \cdot [\varepsilon]\mathbf{E} = 0$ can no longer be further

19

simplified. In fact, in an anisotropic medium the electric field $\mathbf{E}$ is generally not transverse with respect to the wavevector $\mathbf{k}$.

Upon the formation of an out-of-plane magnetization, the trigonal symmetry of CrI_3 dictates that the permittivity tensor must take the following form [40]

$$[\varepsilon] = \begin{bmatrix} \varepsilon_{xx} & \varepsilon_{xy} & 0 \\ -\varepsilon_{xy} & \varepsilon_{xx} & 0 \\ 0 & 0 & \varepsilon_{zz} \end{bmatrix} \qquad (2.24)$$

Due to the presence of magnetism all the elements in $[\varepsilon]$ can be complex. Assuming normal incident $\mathbf{k} = \dfrac{\omega}{c} n\hat{\mathbf{z}}$ where the refraction index n for now is merely a number to be determined, Eq. (2.23) becomes

$$\begin{bmatrix} \varepsilon_{xx} - n^2 & \varepsilon_{xy} & 0 \\ -\varepsilon_{xy} & \varepsilon_{xx} - n^2 & 0 \\ 0 & 0 & \varepsilon_{zz} \end{bmatrix} \begin{bmatrix} E_x \\ E_y \\ E_z \end{bmatrix} = 0 \qquad (2.25)$$

These are the homogeneous linear equations for $\mathbf{E}$. For non-trivial solutions to exist, the determinant of the coefficient matrix must vanish. This gives both the "eigen" refraction indices and the "eigen" polarization modes

$$\begin{aligned} n_L^2 &= \varepsilon_{xx} + \mathrm{i}\varepsilon_{xy}, \ \mathbf{E}_L = \begin{bmatrix} 1 \\ \mathrm{i} \end{bmatrix} \\ n_R^2 &= \varepsilon_{xx} - \mathrm{i}\varepsilon_{xy}, \ \mathbf{E}_R = \begin{bmatrix} 1 \\ -\mathrm{i} \end{bmatrix} \end{aligned} \qquad (2.26)$$

where the z-component is ignored since the eigen polarizations only lie in the x-y plane[1].

From Eqs. (2.26) one already sees the "eigen" modes being left- and right-circularly polarized. To see the dichroism we set $n_{L,R} = \eta_{L,R} + \mathrm{i}\kappa_{L,R}$, therefore the eigen traveling waves carry the factor $\mathrm{e}^{-\kappa_{L,R}z}$ which describes the absorption along z direction. We then define the circular dichroism as the absorption coefficient difference and calculate based on Eqs. (2.26)

$$\mathrm{CD} = \kappa_L - \kappa_R = \frac{\eta\varepsilon'_{xy} + \kappa\varepsilon''_{xy}}{\eta^2 + \kappa^2} \qquad (2.27)$$

---

[1]Note $\mathbf{E}$ being transverse with respect to $\mathbf{k}$ here is special, because for the $[\varepsilon]$ in Eq. (2.24) the wavevector $\mathbf{k} \propto \hat{\mathbf{z}}$ we chose is actually along the optical axis.

where $\eta = (\eta_L + \eta_R)/2$ and $\kappa = (\kappa_L + \kappa_R)/2$. In the case of weak resonance [52] it satisfies $\eta \gg \kappa$, then the above equation becomes

$$\text{CD} = \kappa_L - \kappa_R = \frac{\varepsilon'_{xy}}{\eta} \tag{2.28}$$

To complete the final piece of the puzzle, one notes the Onsager's relation [53] together with Eq. (2.24) requires $\varepsilon_{xy}(-\mathbf{M}) = \varepsilon_{yx}(\mathbf{M}) = -\varepsilon_{xy}(\mathbf{M})$. This implies ε_{xy} is an odd function of the magnetization $\mathbf{M}$. To the lowest order of linear dependence, we have demonstrated CD $\propto \varepsilon'_{xy} \propto \mathbf{M}$. From this section, we prove that in CrI_3 the circular dichroism measurements conducted in the presence of the magnetic order should directly sense the magnetization $\mathbf{M}$. The full utilization of this capability will be discussed later in Chapter 5.

CHAPTER 3

Ultrafast Modulation of the Ferro-Rotational CDW in $1T$-TaS$_2$

3.1   Introduction to CDW in $1T$-TaS$_2$

$1T$-TaS$_2$ is an excellent prototypical material exhibiting complex CDW behavior from symmetry perspective, characterized by a rich phase diagram dependent on temperature [54–58] and other external parameters [59–62]. Despite extensive research on this system for many years, $1T$-TaS$_2$ has recently continued to gain significant interest and attention. Traditionally, its ground state being a Mott insulator together with the CDW order [56, 63, 64], emergent superconductivity upon doping [65–67] or pressure [60, 68], make it a great platform for studying strong correlation physics [56, 69, 70]. Theory and experimental works also hint its quantum spin liquid candidacy [71–75]. Besides such classic questions in condensed matter physics, recent explorations have also been focusing on the ultrafast optical engineering of the lattice or electronic properties of $1T$-TaS$_2$ [76–84], thanks to its various CDW orders and the strong electron-lattice coupling.

This rest of this section provides a brief overview of the CDW orders in $1T$-TaS$_2$, and the experimental techniques used to detect these CDW phases.

3.1.1 CDW phases in $1T$-TaS$_2$

The pristine $1T$-TaS$_2$ at high temperature has $P\bar{3}m1$ symmetry with $a = b = 3.38$ Å, $c = 6.95$ Å. Its structure can be described from a layered perspective where each layer consists of Ta atoms sandwiched between two adjacent layers of S atoms, forming an octahedral coordination as shown in Fig. 3.1(a). The Ta atoms in the a-b plane form a triangular lattice as shown in Fig. 3.1(b). The prefix T denotes the trigonal symmetry and the number 1 indicates a single layer in the unit cell. This reflects that the layers stack along the c-axis without a lateral slide. The structure hence has a centrosymmetric point group D_{3d} which consists of one threefold rotational axis along c-axis, and three vertical mirrors at every $120°$ marked by the orange dashed lines in Fig. 3.1(b).
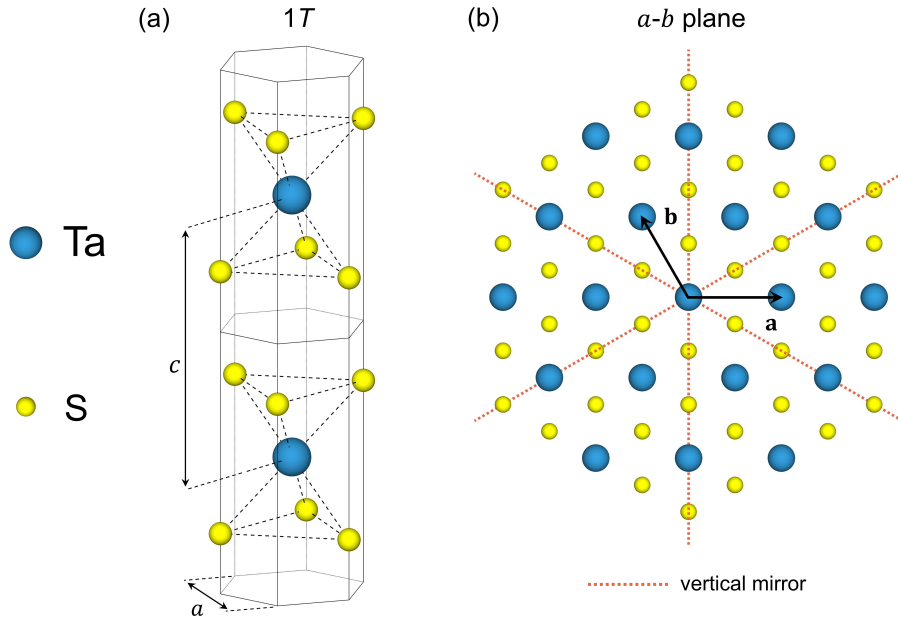
Figure 3.1: Crystal structure of $1T$-TaS$_2$. (a) Schematic of the $1T$ polytype of two Ta-S octahedra. (b) Top view of $1T$-TaS$_2$ lattice in the a-b plane. The crystal axes **a** and **b** are marked with black arrows.

$1T$-TaS$_2$ undergoes several phase transitions as the temperature is lowered, leading to different CDW states. At high temperatures, $1T$-TaS$_2$ is metallic and exhibits an incom-

mensurate CDW (ICCDW) phase [54, 85]. In this phase, the Fermi surface is only partially gapped and the CDW modulation wave vector does not match the periodicity of the underlying lattice. Without a locking between the charge order and the lattice, this phase retains the high symmetry of the pristine lattice.
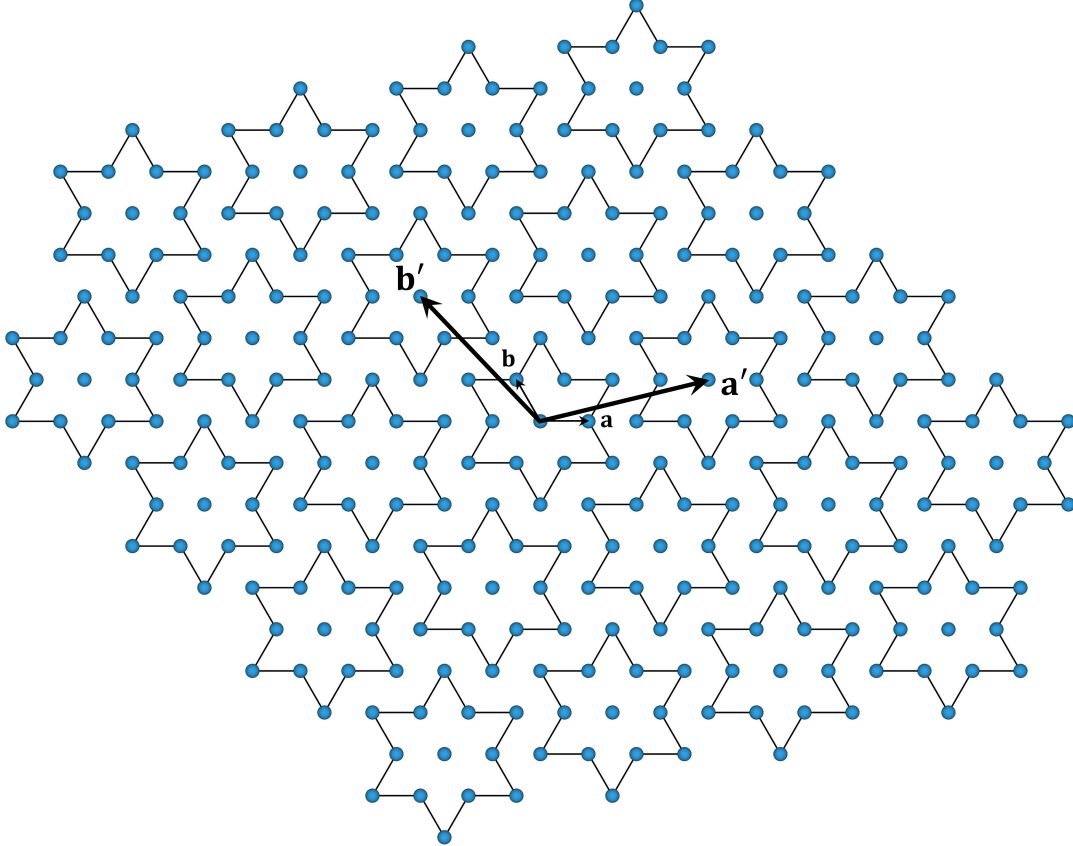
Figure 3.2: Sketch of the ordering of star-of-David clusters in the (N)CCDW phase. The $\sqrt{13} \times \sqrt{13}$ superlattice axes $\mathbf{a}'$ and $\mathbf{b}'$ (thick arrows) rotate away from the pristine crystal axes $\mathbf{a}$ and $\mathbf{b}$ (thin arrows). Only Ta atoms are plotted in the figure.

As the temperature decreases to around $T_{\mathrm{NCCDW}} = 355$ K, the material transitions into the nearly-commensurate CDW (NCCDW) phase. This phase is characterized by commensurate CDW (CCDW) domains separated by ICCDW domain walls [86, 87]. With further cooling down to approximately $T_{\mathrm{CCDW}} = 183$ K, the commensurate domains expand and become coherent, essentially eliminating the separating incommensurate domain walls. This marks that the system enters the CCDW phase. Similar to many systems with concomitant

lattice instability, the CCDW in $1T$-TaS$_2$ also features its own lattice reconstruction, which manifests itself as the formation of the stars-of-David through each 13 Ta atoms aggregating towards the center [88]. This way, the CDW wavevector or the lattice vector rotates $\sim 13.9°$ away from the original undistorted direction and achieves a new $\sqrt{13} \times \sqrt{13}$ unit cell [55], as shown in Fig. 3.2.

Note that the formation of the periodic stars-of-David is fully commensurate with the pristine lattice. The new periodicity of those stars-of-David in the NCCDW and CCDW phases reduces the point group from D_{3d} to S_6, remarkably by losing the three vertical mirrors. As a result, polar electric dipoles become allowed for each broken mirror. With the existence of the threefold axis, such dipoles shall from a head-to-tail loop arrangement which, as introduced in Fig. 1.1 in Chapter 1, is of ferro-rotational nature in symmetry.

3.1.2   Probing CDW in $1T$-TaS$_2$

Detecting the CDW in $1T$-TaS$_2$ can usually be achieved by static experimental probes. This includes using X-ray or electron diffraction [54, 55] to construct the new reciprocal lattice, or Scanning Tunneling Microscopy [58, 86, 89] to render real-space topographic images for direct visualization of the atomic distribution in the CDW state. Electronically, Angle-Resolved Photoemission Spectroscopy [90, 91] can also be employed to probe the folded bands and Fermi surface gapped out by the formation of CDW.

In addition to the techniques above, the collective excitations of a CDW provide new opportunities for characterizing the order. As sketched in Fig. 3.3, a typical one-dimensional CDW can give rise to two types of collective excitations: the amplitude mode (Amplitudon) which is the coherent oscillation of the charge density magnitude similar to a breathing motion, and the phase mode (phason) which corresponds to the coherent shift of the charge density distribution. With a parallel analogy to the collective excitations of a lattice, namely phonons, one could postulate that the amplitude mode is massy and has an energy gap at $\mathbf{k} = 0$ just like an optical phonon, while the phase mode is gapless and disperses like an

acoustic phonon [92–94]. The former observation enables the optical detection of the CDW amplitude mode through dynamic probes, such as Raman Scattering [95], ultrafast optical pump-probe [96, 97] and time-resolved diffraction [98, 99] measurements.
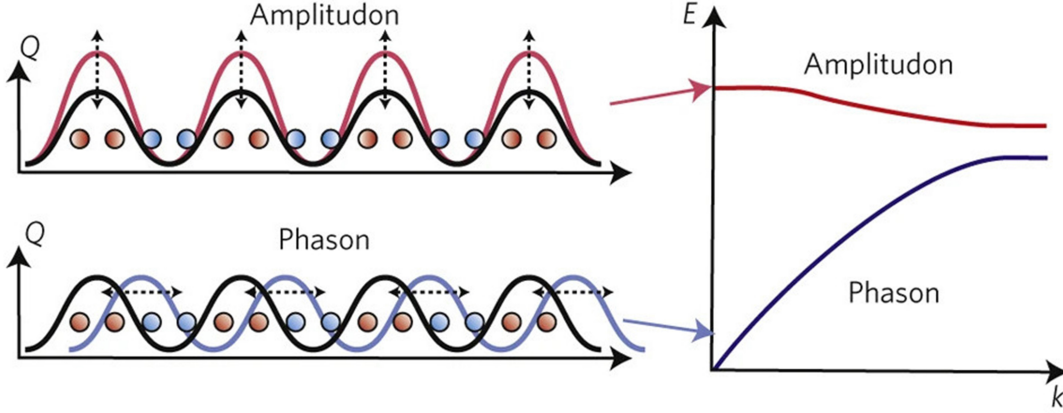
Figure 3.3: Schematics of the amplitude (upper left) and phase (bottom left) modes in an one-dimensional CDW. The amplitude mode represents the overall oscillation of the charge density magnitude and the phase mode corresponds to the sliding motion of the charge density. The amplitude mode exhibits an optical phonon-like dispersion while the phase mode dispersion is acoustic phonon-like and gapless. Figure adapted from [94].

In the following sections I present our nonlinear EQ RA-SHG detection of the CCDW order by sensing the breaking of the mirror symmetries. Then adopting a pump-probe scheme, I will show the successful ultrafast modulation of the CDW through optical pumping in time-resolved (tr-) RA-SHG measurements. Careful spectroscopic analysis and pump fluence dependent results further hint that time-resolved nonlinear optics helps reveal a hidden triplet mode and a possible transient CDW phase at high pump fluence.

3.2 Static RA-SHG measurements of the ferro-rotational (N)CCDW

We experimentally confirm the ferro-rotational nature of the (N)CCDW in $1T$-TaS$_2$ by performing temperature dependent static RA-SHG measurements. With normal incidence,

the experiments are conducted with the geometry as shown in Fig. 2.1(b). While rotating the polarization of the incident fundamental light at 800 nm, namely ϕ as the angle between the incident polarization and the crystal axis **a**, the reflected SHG intensity is recorded with an analyzer always perpendicular to the incident polarization. We denote the signal in this crossed polarization channel as $I_{\perp}^{2\omega}(\phi)$. The main panel of Fig. 3.4(a) displays the polar plots of RA-SHG data taken at 280 and 120 K, above and below T_{CCDW}, respectively. Compared with the crystal axes **a** and **b** determined by electron diffraction [100, 101], it is apparent that the RA patterns at both temperatures rotate away, evidencing mirror symmetry breaking that are prescribed by the ferro-rotational point group S_6 [102]. On a side note, a similar measurement on a heat-treated sample with equal fraction of clockwise-rotation and counterclockwise-rotation domains shows the RA pattern symmetric with respect to the crystal axes [101], indicating that the original of RA-SHG pattern rotation is due to the formation of ferro-rotational CDW.
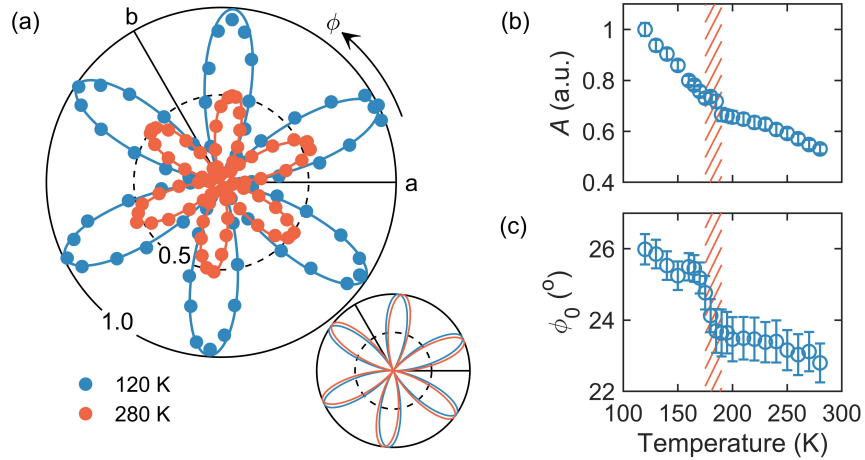
Figure 3.4: (a) Polar plots of RA-SHG data taken at 120 K in the CCDW phase (blue) and at 280 K in the NCCDW phase (orange). Solid lines are fits to the calculated EQ RA-SHG functional form $I_{\perp}^{2\omega}(\phi) = A\cos^2 3(\phi - \phi_0)$. Inset shows the 120 and 280 K fits normalized to their own maxima to illustrate the increased rotation ϕ_0 at the lower temperature. (b)–(c) Temperature dependence of RA-SHG pattern amplitude A (b) and angle of rotation from **a** axis ϕ_0 (c) in a cooling cycle. The transition from the NCCDW to CCDW phase is captured at around 185 K (marked as orange vertical strips). Error bars stand for 1 standard error of the fits to extract A and ϕ_0.

Performing the simulation outlined in Section 2.1.4, the S_6 point group symmetry dictates that the RA-SHG signal is from EQ radiation and takes the functional form $I_\perp^{2\omega}(\phi) = A \cos^2 3(\phi - \phi_0)$, where A and ϕ_0 correspond to the amplitude and angular orientation of the RA-SHG pattern, respectively, and relate to the bulk EQ susceptibility tensor χ_{ijkl}^{EQ} via

$$A = \sqrt{\chi_{xxzx}^2 + \chi_{yyzy}^2}, \quad \phi_0 = \frac{1}{3} \arctan \frac{\chi_{xxzx}}{\chi_{yyzy}} \tag{3.1}$$

The surface ED contribution can be convincingly ruled out by thickness dependent RA-SHG measurements [103].

The RA-SHG data at both temperatures fit well to this simulated function [solid lines in Fig. 3.4(a) main panel]. The fits show a clear enhancement in the amplitude A, and a resolvable increase in the orientation ϕ_0 at the lower temperature. The two features are visible in the main panel and inset of Fig. 3.4(a), respectively. Furthermore, the thorough temperature dependence of EQ RA-SHG retains the threefold rotational symmetry between 280 and 120 K. Across the phase transition at T_{CCDW}, A shows a kink of changing slopes and ϕ_0 exhibits a sudden increase, as shown in Fig. 3.4(b) and (c). Both behaviors are consistent with the enhancement of the ferro-rotational order parameter across the transition, from NCCDW with short-range ordered star-of-David patches, to CCDW with long-range ordered uniform domains [86], where a rotation of superlattice wavevectors by $\sim 2°$ is also observed by diffraction techniques [55]. We also comment that our experiments are conducted in cooling cycles such that no signature of the triclinic CDW phase is observed. This phase is reported to exist between 220 and 280 K only in heating cycles [58].

3.3 Time-resolved SHG measurements of the ferro-rotational CCDW

We present the dynamics of the ferro-rotational order by firstly pumping the NCCDW and CCDW phases with femto-second optical pulses at 720 nm that create a transient imbalance of photo-induced electrons and holes [77, 104] and then probing the temporal evolution of both phases by the SHG intensity, measured with 800 nm fundamental normal incident light pulses in the crossed channel at an azimuth angle $\phi = 69.3°$. The pump and fundamental probe beams are both at 200 kHz repetition rate and incident collinearly onto the sample.
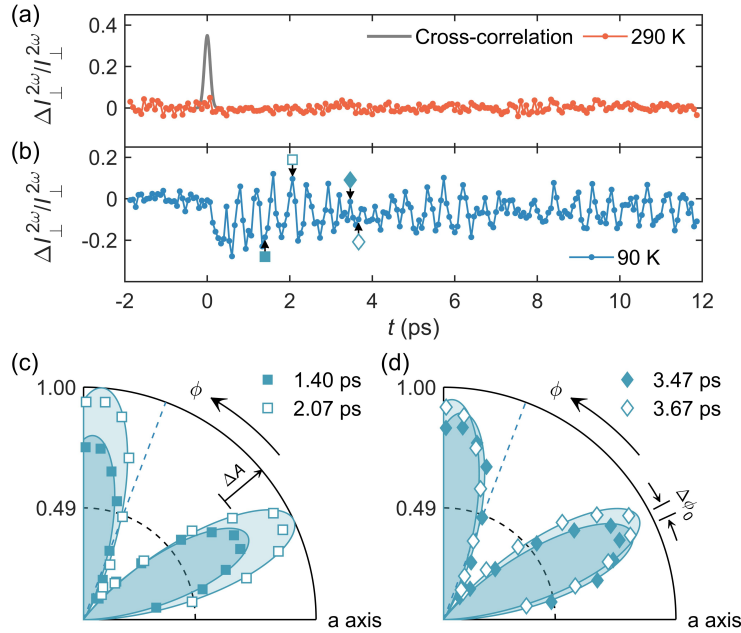
Figure 3.5: (a) Normalized tr-SHG intensity (orange) at $\phi = 69.3°$ taken at 290 K in the NCCDW phase. The cross-correlation function (gray) between pump and probe pulses is shown to mark time zero and time resolution. (b) Normalized tr-SHG trace (blue) at $\phi = 69.3°$ taken at 90 K in the CCDW phase, showing both the slow recovery process after the sudden suppression at time zero, and the fast coherent oscillations with a beating profile. (c-d) Comparisons between transient RA-SHG patterns at two pairs of delay time marked by black arrows in (b). The dashed blue radial line represents the polarization angle $\phi = 69.3°$ at which the tr-SHG trace in (b) was measured. The dashed black arc at 0.49 represents the pre-time-zero SHG intensity level in (b). The comparisons in (c) and (d) demonstrate the change in SHG are manifested in both the RA-SHG amplitude and orientation.

Figures 3.5(a) and (b) plot the relative change in the SHG intensity after pumping, $\frac{\Delta I_\perp^{2\omega}(t)}{I_\perp^{2\omega}(t<0)}$, taken at 290 K for the NCCDW and 90 K for the CCDW. The time zero $t = 0$ ps and the temporal resolution $t_{\text{res}} = 0.09$ ps are determined by the peak and the full width at half maximum of the cross-correlation function between the pump and probe pulses [gray solid line in Fig. 3.5(a)]. The SHG intensity for the NCCDW does not show any time-dependent change as in Fig. 3.5(a), which is expected due to the strong suppression and damping of the excitations in short-range orders [86, 105]. In contrast, the tr-SHG trace for the CCDW shows two prominent features: the slow recovery after the sudden suppression at time zero and the fast coherent oscillations with a beating profile [Fig. 3.5(b)]. To identify the sources of both time-dependent features, two pairs of RA-SHG patterns at different delays [marked by black arrows in Fig. 3.5(b)] are measured and compared. The two RA-SHG patterns at $t = 1.40$ and 2.07 ps show a clear change in the amplitude [ΔA as marked in Fig. 3.5(c)], whereas those at $t = 3.47$ and 3.67 ps display a notable change in the orientation [$\Delta\phi_0$ as marked in Fig. 3.5(d)]. It is noted that the ferro-rotational order parameter for this CCDW is encoded through the SHG susceptibility tensor elements in Eq. (3.1), which enter into both A and ϕ_0 and thus the full RA-SHG pattern [Fig. 3.4(b) and (c)]. Such observations suggest that we track the time dependence of both the RA-SHG amplitude and orientation, $A(t)$ and $\phi_0(t)$, to get a comprehensive characterization of the dynamic modulation of this ferro-rotational CCDW.

3.3.1 Time-resolved RA-SHG and spectroscopic analysis

To acquire $A(t)$ and $\phi_0(t)$, the full azimuth angle ϕ dependent RA-SHG measurements are performed at every delay time t, which construct the map of tr-RA-SHG—the SHG intensity $I_\perp^{2\omega}$ as functions of t and ϕ—taken in the crossed polarization channel at 90 K [Fig. 3.6(a)]. In this map, a horizontal slice is a tr-SHG trace akin to Fig. 3.5(b), and a vertical cut is a transient RA-SHG pattern in analogy to Fig. 3.4(a). We fit the individual RA-SHG pattern at every delay time t with $I_\perp^{2\omega}(\phi, t) = A(t)\cos^2 3(\phi - \phi_0(t))$ and obtain the

time dependence of both the amplitude and orientation, $A(t)$ and $\phi_0(t)$. Their changes with respect to the pre-time-zero ($t < 0$) values are plotted in Fig. 3.6(b) after a normalization $\frac{\Delta A(t)}{A(t < 0)}$, and in Fig. 3.6(c) in absolute size $\Delta\phi_0(t)$, respectively. Two differences are noted. First, it is evidently present in the amplitude but absent in the orientation channel that a sudden suppression happens right upon the pump excitation (i.e., $t = 0$) and recovers slowly over a couple of pico-seconds. Second, the beating profiles of the fast coherent oscillations show distinct phases and frequencies between the two traces, which corroborates with the difference in their fast Fourier transformation (FFT) spectra shown in Fig. 3.6(d).
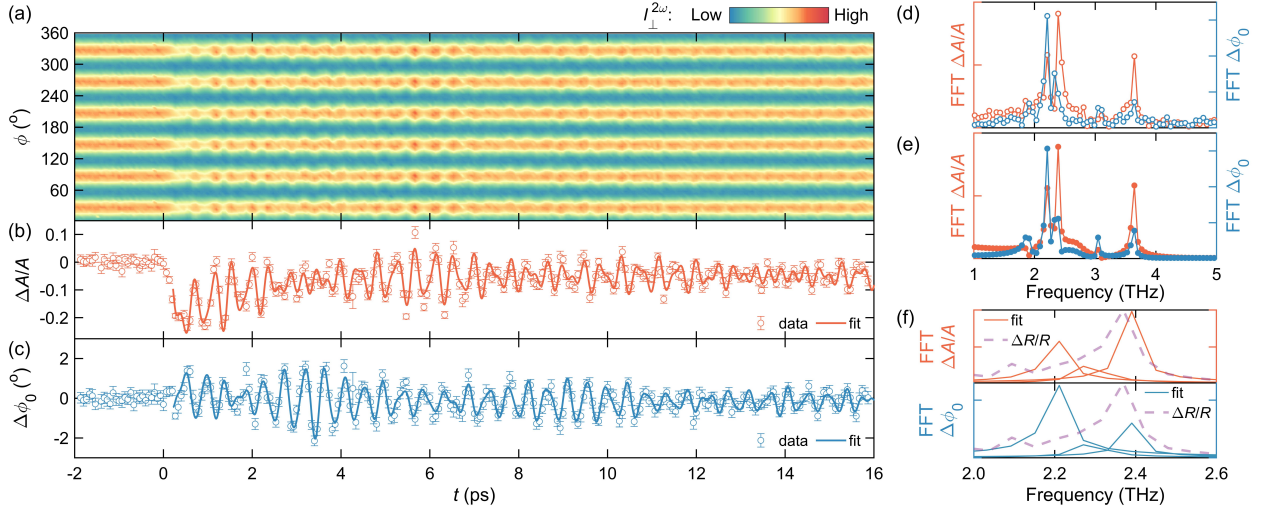
Figure 3.6: (a) Map of tr-RA-SHG intensity $I_\perp^{2\omega}(\phi, t)$ as a function of the polarization ϕ and the delay time t taken at 90 K. (b-c) Time dependent changes of amplitude normalized to the pre-time-zero value (b) and orientation in absolute size (c), after fitting RA-SHG at individual delay time. Solid lines show the fits of both traces to a functional form consisting of one exponential decay $M_\mathrm{B}e^{-t/\tau_\mathrm{B}}$ and six under-damped oscillations $\sum_{i=1}^{6} M_i e^{-t/\tau_i} \cos(\omega_i t + \delta_i)$. (d-e) FFTs of the raw traces (d) and of their fits (e). Orange and blue represent the amplitude and orientation channels, respectively. (f) Zoom-in plots of FFTs of the fitted traces near the CCDW amplitude mode frequency in the amplitude (orange) and orientation (blue) channels, detailing the triplet structure. The FFTs of tr-fundamental reflectivity ($\Delta R/R$) (purple) is plotted as a comparison.

We fit the $\frac{\Delta A(t)}{A(t < 0)}$ and $\Delta\phi_0(t)$ traces simultaneously with one exponential decay background $M_\mathrm{B}e^{-t/\tau_\mathrm{B}}$ and six under-damped oscillations $\sum_{i=1}^{6} M_i e^{-t/\tau_i} \cos(\omega_i t + \delta_i)$. So far this has been the minimum number of modes required to satisfactorily reproduce the spectro-

scopic features in Fig. 3.6(a)–(d). Here, the decay time constants, τ_B and τ_i, and the oscillation frequencies ω_i are kept the same for both fits, whereas the magnitudes, M_B and M_i, and the oscillation phases δ_i are set free. The fits [solid lines in Fig. 3.6(b) and (c)] well capture all key features of $\dfrac{\Delta A(t)}{A(t < 0)}$ and $\Delta\phi_0(t)$ traces, and the FFTs of the fits in Fig. 3.6(e) nicely reproduce those of the raw spectra in Fig. 3.6(d). For the slow incoherent recovery process, indeed it only has a finite magnitude in the amplitude channel with a decay constant of $\tau_B = 1.6\,\mathrm{ps}$ but little magnitude in the orientation channel. For the fast coherent oscillations, six distinguishable frequencies are identified in both channels, three of which at 1.89±0.02, 3.06±0.01 and 3.628±0.006 THz are phonon modes observed in Raman spectra [106] and the other three at 2.201±0.004, 2.29±0.01, and 2.387±0.005 THz are around the CCDW amplitude mode reported by Raman [106], time-resolved reflectivity [107, 108] and ultrafast diffraction [98, 109] measurements.

Of particular interest is the triplet at around 2.4 THz, because of its higher spectral weight than the rest and that only a single CCDW amplitude mode has been observed in tr-fundamental reflectivity spectra [103, 107, 108]. The individual modes of this triplet in the amplitude and the orientation channels are shown in Fig. 3.6(f). It is worth noting that our tr-RA-SHG data reveals that the reported amplitude mode in fact contains a nontrivial triplet structure with distinct weight distributions in the amplitude and orientation channels. The CDW in $1T$-TaS$_2$ is reported to have triple-$\mathbf{q}$ nesting [110, 111] and thus the triplet structure is likely to result from the multiple collective excitations of the ferro-rotational CCDW. Future studies are needed to assign individual modes in the triplet to specific excitations.

3.3.2   Fluence dependence and a possible photo-induced transient CDW state

We carry out the tr-RA-SHG measurements and perform the same analysis as in Fig. 3.6 at five different pump fluences, 0.36, 0.46, 0.58, 0.66 and 0.92 mJ/cm^2. The extracted

$\dfrac{\Delta A(t)}{A(t<0)}$ and $\Delta\phi_0(t)$ traces and their fits are shown in Fig. 3.7(a) and (b), respectively. As the fast coherent oscillations dominate the slow incoherent recovery process in the amplitude channel at high fluences [Fig. 3.7(a)], and that the incoherent recovery time constant shows little fluence dependence, we focus our discussion on the coherent oscillations. We show the fitted frequencies of the triplet near the CCDW amplitude mode in Fig. 3.7(c) and the magnitude of the strongest in the triplet in the orientation channel in Fig. 3.7(d).

The fluence dependent study may have revealed a novel transient CDW state. First, the frequencies of the triplet structure show a sudden shift at a critical fluence of $F_C \sim 0.5\,\mathrm{mJ/cm}^2$, which contributes to the evolution of the beating profile upon increasing the pump fluence as shown in Fig. 3.7(a) and (b). In contrast, such a frequency shift is not detectable in the tr-fundamental reflectivity [Fig. 3.7(c), purple diamonds]. Second, the magnitude of the oscillations experiences a dramatic increase across F_C that is also visible in traces in Fig. 3.7(b). Both anomalous behaviors of the frequency shift and the magnitude enhancement across F_C are indicative of a potential electromagnetic radiation-induced phase transition. Considering the fact that there is no tr-SHG signal observed in the NCCDW phase at $T > T_{\mathrm{CCDW}}$ whereas clear dynamics in tr-SHG is present for all fluences investigated, we can confidently rule out the possibility of this observed photo-induced phase transition resulting from a photo-heating-induced transition from the CCDW into the NC-CDW state. In fact, the photo-heating effect from the pump in this study is minimal as there is no pre-time-zero changes in tr-reflectivity and tr-RA-SHG, nor post-time-zero incoherent exponential decay in $\Delta\phi_0(t)$ observed even at our highest fluence. We thus attribute F_C as the critical value where the pump-induced electron-hole imbalance is large enough to destroy the star-of-David clusters and lead to a transient new CDW phase.

Finally, we would like to discuss the comparison between this photo-induced CDW phase that is transient, short-lived and the previously reported optically manipulated CDWs in $1T$-TaS_2. First, a single femto-second light pulse with an incident fluence of $\geqslant 5\,\mathrm{mJ/cm}^2$ at room temperature was reported to create or destroy metastable mirror-related domains
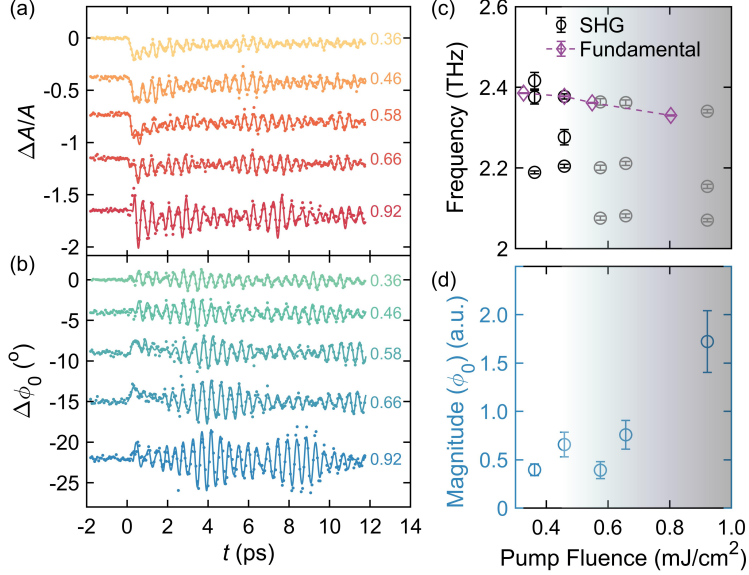
Figure 3.7: (a-b) Fluence dependence of the time dependent amplitude (a) and orientation (b) changes fitted from tr-RA-SHG maps taken at pump fluences of 0.36, 0.46, 0.58, 0.66 and 0.92 mJ/cm². Solid lines are fits to the same functional form as in Fig. 3.6. (c) The fluence dependence of the fitted frequencies for the triplet structure (black and gray circles) around the CCDW amplitude mode in tr-RA-SHG and that of the CCDW amplitude mode (purple diamonds) in tr-fundamental reflectivity. (d) The fluence dependence of the strongest magnitude in the triplet in the orientation channel. The gradient background marks the frequency shift in (c) and the magnitude enhancement in (d) across a critical pump fluence of 0.5 mJ/cm².

in the NCCDW state [109]. In addition to our much lower critical fluence of 0.5 mJ/cm² and much shorter lifetime of a few pico-seconds, the observed collective mode frequency shift above F_C is not compatible with creation or annihilation of energetically degenerated, mirror-symmetry-related CCDW domains because they should host the very same collective excitations as the CCDW phase below F_C. Second, a single 35 fs, $\geqslant 1$ mJ/cm² light pulse below 70 K was shown to induce a hidden metastable, metallic CDW phase whose amplitude mode [77] and wavevector [104] are slightly shifted from those of CCDW. Further studies on this photo-induced hidden metastable CDW phase revealed that its lifetime significantly decreases at higher temperatures [78, 82]. Considering the similar frequency shift but higher temperature and lower critical fluence in our study compared to those in literature, it is likely that our photo-induced transient CDW here is a short-lived version of the hidden

metastable CDW phase, which is observable at the ultrafast timescale thanks to the direct coupling between tr-EQ-RA-SHG and the ferro-rotational nature of this CDW.

<h1 style="text-align: center;">CHAPTER 4</h1>

Magnetic-Field-Induced Quantum Phase Transitions in Bulk CrI$_3$

4.1   Bulk and few-layer CrI$_3$

During the surge of interest in the development of two-dimensional magnetic materials, the transition metal trichalcogenide CrI$_3$ has seen a great success. The isolation of few-layer CrI$_3$ has opened new avenues in the study of low-dimensional systems, revealing novel phenomena such as layered AFM [29] and gate-tunable magnetic phases [112–115] in the earliest studies. Further exploration about the moire engineering of 2D magnetism based on thin-layer CrI$_3$ will be discussed in later Chapter 5.

In addition to the vast potential based on the AFM order in few-layer CrI$_3$, the study of bulk CrI$_3$ remains crucial from several perspectives. First and fundamentally, while few-layer CrI$_3$ has the layered AFM order that develops under $T_N = 45$ K [29], bulk CrI$_3$ is shown to be a FM with Curie temperature $T_C = 61$ K [116]. This direct discrepancy indicates the very intriguing underlying magnetic interactions in this material. Secondly, while bulk CrI$_3$ can also be treated as stacked layers, in the bulk form the layers stack rhombohedrally at low temperature but monoclinically above $T_s = 220$ K [116], as shown in Fig. 4.1. A further experimental observation of the enhanced reduction of interlayer spacing below T_C in bulk CrI$_3$ [116] suggests a strong magneto-elastic coupling. Such flexibility of the lattice, or more specifically the stacking orders, provides great potential towards the tunability of the

spin system that can be exploited to achieve interesting engineering possibilities specifically in the 2D form, as will be presented in Chapter 5. Furthermore, gapped magnon modes have been observed in both bulk [117, 118] and thin-layer CrI_3 [119], indicating the Ising-type exchange anisotropy. Such anisotropy not only is critical for the magnetic stability of monolayer CrI_3, but also can host other interesting magnetic properties such as the Kitaev interaction [120–122] and topological spin excitations [123, 124].
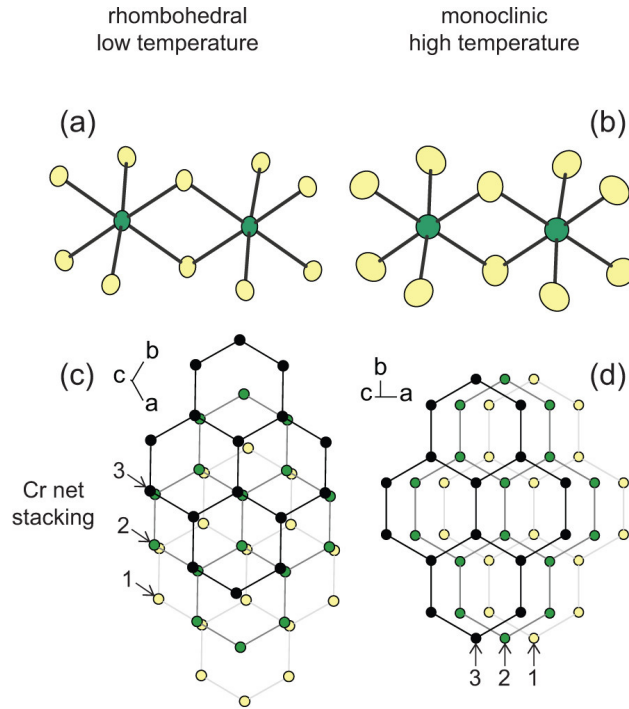
Figure 4.1: Comparison of the stacking orders of CrI_3 layers. (a)(c) Rhombohedral stacking. (b)(d) Monoclinic stacking. Figure adapted from [116].

A magnetic field- and temperature-dependent polarized Raman study is presented in the rest of this chapter. By careful selection rule analysis, a novel mixed state of surface AFM and bulk FM is proposed, and a further magnetic field-induced structural phase transition is revealed. Through studying bulk CrI_3, such intricate interplay between magnetism and crystalline structures provides the baseline for the future engineering of 2D magnetism.

4.2 Coexistence of AFM and FM magnons

The low-lying spin system excitation, namely, magnons provide us with information about the magnetic structure in bulk CrI_3. Figure 4.2(a)–(c) show the external magnetic field dependent Raman spectra at lower wavenumbers measured at low temperature $T = 10$ K and with circular polarizations, where LL denotes the incident light and scattered light are selected to be co-circularly polarized and LR denotes opposite senses of rotation. This way, we eliminate the Faraday rotation caused by the optical components under external magnetic field that could have violated the linear polarization used in a traditional Raman experiment. From Fig. 4.2(a)–(c), we observe several ultra-low frequency modes, referred to as M_0 hereafter, that had not been detected in Raman measurements before this study [125–127], and identify them as magnons for the following three reasons.

First, a clear linear dependence of energy on magnetic field B_z is seen in Fig. 4.2(b). This Zeeman energy shift $\propto B_z$ is a direct result of magnons emergent from collinear spins. Energy-wise, their frequencies of approximately 4 cm^{-1} (0.5 meV) are close to the reported spin wave gap which is on the order of 1 meV [117]. This small spin wave energy is also consistent with the consideration that Cr being a $3d$ metal element should not bring a large spin-orbit coupling that is responsible for the Ising-type anisotropy. Thirdly, those M_0 modes soften towards zero energy upon heating, as shown in Fig. 4.2(d). The comparison to the temperature dependence $\sqrt{T_c - T}$ of an order parameter based on mean-field theory [128] further indicates that such modes are of magnetic origin [Fig. 4.2(e)].

After designating the magnon identity of the M_0 modes, we also note that multiple branches are present in Fig. 4.2(b). With the fact that Stokes side and anti-Stokes side in Raman Scattering generally probe the same excitation but only differ in intensity understood, we shall focus on the anti-Stokes (negative Raman shift) spectrum. We observe that three spin wave branches at magnetic fields lower than 2 T collapse into one branch across $B_c = 2$ T. For further quantification, all the M_0 modes are fitted with a Lorentzian function and their frequencies are summarized in the left panel of Fig. 4.3(a). We note in particular,
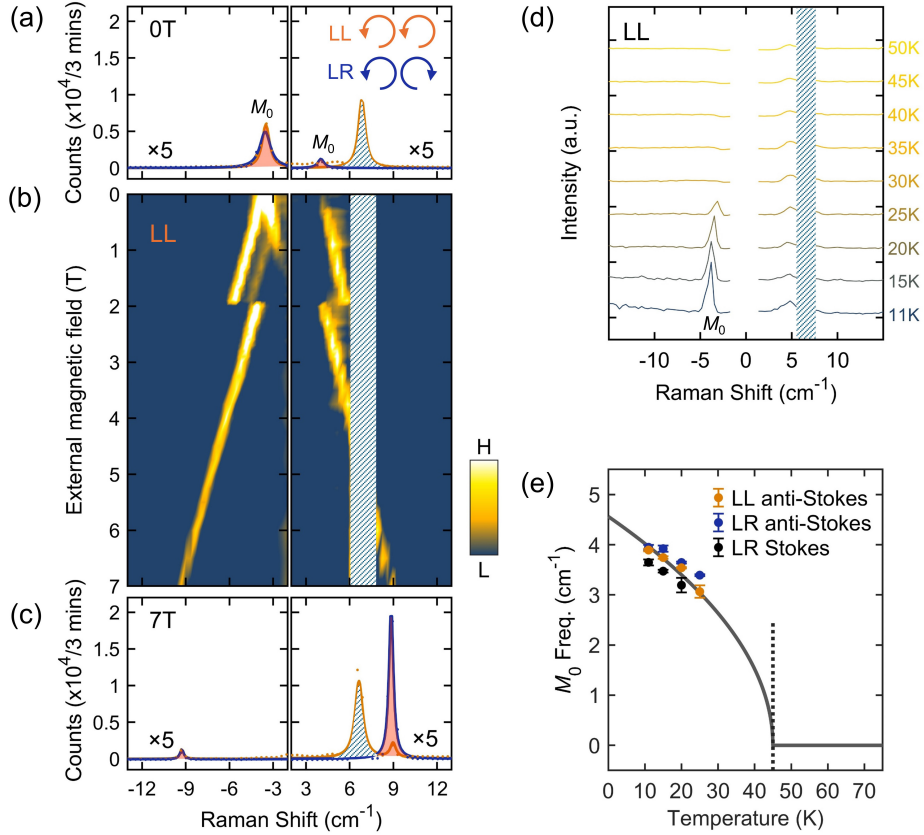
Figure 4.2: Magnon modes in bulk CrI_3 revealed in Raman Scattering. (a) Raman spectra taken at 10 K and 0 T in the LL and LR channels. LL(R) stands for the polarization channel in which the incident and scattered light is left and left (right) circularly polarized, respectively. Solid dots are raw data points and solid lines are Lorentzian fits. (b) A color map of magnetic field-dependent Raman spectra taken over a magnetic field range of 0-7 T at 10 K in the LL channel. The shaded area is to block a noise line. (c) Raman spectra taken at 10 K and 7 T in the LL and LR channels. (d) Temperature dependent Raman spectra taken at 0 T in LL channel. (e) Temperature dependence of the fitted M_0 frequencies measured at 0 T. The solid grey line shows a $\sqrt{T_c - T}$ trend with onsite $T_c = 45$ K.

below 2 T, a pair of the three starts with close frequencies of approximately 3.4 and 3.9 cm^{-1} at 0 T and diverges with increasing magnetic field (M_{0a} and M_{0b}), while the third one increases linearly since its appearance at approximately 1 T and continues after B_c of 2 T with a slight discontinuity of frequency redshift (M_{0c}). The field dependence of M_{0a} and M_{0b} is the typical behavior of AFM spin waves in which the angular momenta of two degenerate spin waves are antiparallel to the external magnetic field. The fact that M_{0c} continues after B_c is otherwise indicative that it corresponds to the overall FM as that is the state at high

magnetic field.
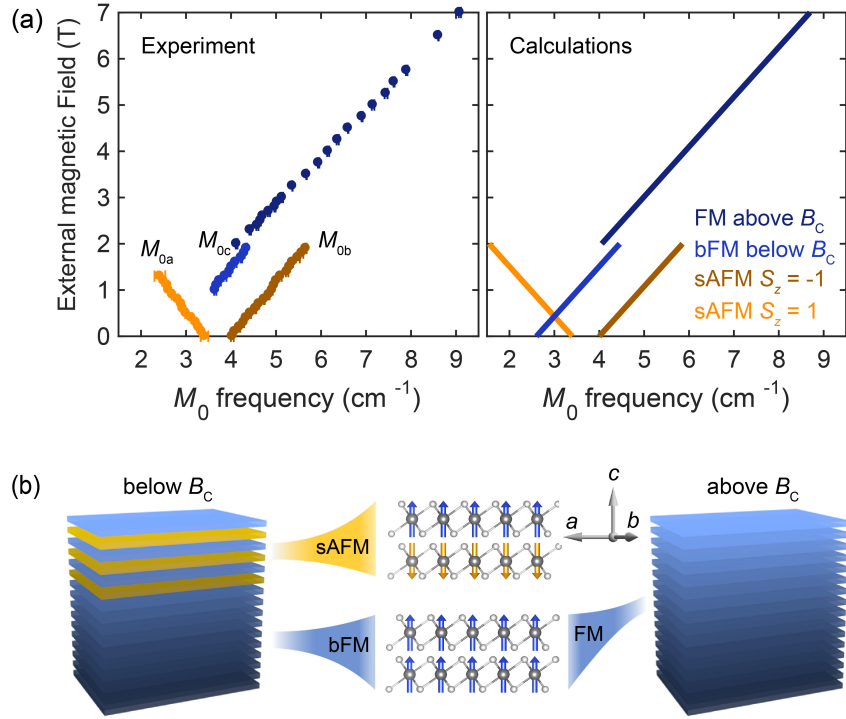
Figure 4.3: Establishing the mixed sAFM and bFM phase in bulk CrI$_3$. (a) Magnon frequencies from fitting experimental data (left) and spin wave calculations (right). M_{0a}, M_{0b} and M_{0c} label the three spin wave branches below the critical magnetic field $B_c = 2$ T. (b) Schematics of the mixed state of the surface layered AFM (sAFM for the state with alternating spin moments in the adjacent layers at the sample surface) and the deep bulk FM (bFM for the state with all the spin moments along one direction) below B_c and the pure FM state above B_c.

Our experimental observations above suggest a mixed state of layered AFM and FM for a CrI$_3$ bulk, in contrast to the literature assignment of a pure FM phase [116]. This suggestion is consistent with the absence of M_{0c} below B_c in CrI$_3$ flakes [129]. As sketched in the left of Fig. 4.3(b), below B_c, top layers of bulk CrI$_3$ host layered AFM (denoted as sAFM) that is similar to what has been reported in 2D CrI$_3$ thin films [112–115], and the deeper bulk exhibits a FM order (denoted as bFM) that is consistent with bulk magnetization measurements [130]. Meanwhile, the small energy scale of about 1 μeV [131] of the long-range magnetic dipole-dipole interactions favoring the interlayer FM is much weaker than the interlayer AFM exchange coupling of 150 μeV. Therefore, we rule out the possibility of pure

magnetic energetic reasons and require surface reconstructions to establish the interlayer AFM coupling at the surface while having FM coupling in the bulk. Hence, the sAFM provides the pair of spin waves with Zeeman splitting (M_{0a} and M_{0b}) while the bFM leads to the third branch with a linearly increasing frequency with increasing magnetic field (M_{0c}). Also note that the bFM provides an effective magnetic field of around 0.27 T to lift the degeneracy of the two sAFM spin waves at 0 T. Above B_c, sAFM transits into FM in the same manner as layered AFM does in CrI_3 thin flakes [112–115], making the entire CrI_3 crystal in an overall FM state as shown in the right of Fig. 4.3(b). This results in a sole spin wave branch above B_c.

4.2.1 Spin wave calculations for sAFM and bFM

We further carry out spin wave calculations for the proposed states. We consider an anisotropic Heisenberg XXZ Hamiltonian for the intralayer spin-spin interaction, together with isotropic interlayer contributions and Zeeman energy. The total Hamiltonian can be separated into

$$H = H_{\text{intra}} + H_{\text{inter}} + H_{\text{Zeeman}} \tag{4.1}$$

to which the contributions are

$$H_{\text{intra}} = -J_1 \sum_{l,\langle i,j\rangle} \left(\boldsymbol{S}_{i,\parallel}^{(l)} \cdot \boldsymbol{S}_{j,\parallel}^{(l)} + \gamma S_{i,z}^{(l)} S_{j,z}^{(l)} \right) \tag{4.2}$$

$$H_{\text{inter}} = -J_2 \sum_{i} \boldsymbol{S}_{i}^{(1)} \cdot \boldsymbol{S}_{i}^{(2)} \tag{4.3}$$

$$H_{\text{Zeeman}} = -g_S \mu_{\text{B}} B \sum_{l,i} S_{i,z}^{(l)} \tag{4.4}$$

where $\boldsymbol{S}_i^{(l)}$ denotes the i-th vector spin in the l-th layer, J_1 (J_2) denote the intra- (inter-) layer exchange interactions, γ represents the anisotropy, g_S is the Landé g factor for pure spin, μ_{B} is the Bohr magneton. The summation in Eq. (4.2) is for nearest neighbors $\langle i,j\rangle$

in the same layer only.

We model the sAFM order in a bilayer lattice, where each unit cell contains 4 spins and J_2 is negative for an AFM coupling. we first apply the Holstein-Primakoff transformation [132] to map the spin operators into magnon operators

- spin-up sublattice A and B

$$S_{i,z}^{A} = S - a_i^\dagger a_i$$

$$S_{i,+}^{A} = \sqrt{2S}\sqrt{1 - \frac{a_i^\dagger a_i}{2S}}\, a_i$$

$$S_{i,-}^{A} = \sqrt{2S}a_i^\dagger\sqrt{1 - \frac{a_i^\dagger a_i}{2S}}$$

- spin-down sublattice C and D

$$S_{i,z}^{C} = -S + c_i^\dagger c_i$$

$$S_{i,+}^{C} = \sqrt{2S}c_i^\dagger\sqrt{1 - \frac{c_i^\dagger c_i}{2S}}$$

$$S_{i,-}^{C} = \sqrt{2S}\sqrt{1 - \frac{c_i^\dagger c_i}{2S}}\, c_i$$

where A and B denote the two up-spins in layer one, C and D denote the two down-spins in layer two. Keep the lowest order in magnon operators and sorting our the total Hamiltonian we have for intralayer couplings

$$H_{\text{intra},2}^{\text{top}} = -3J_1 S \sum_{\boldsymbol{k}} (s_{\boldsymbol{k}} a_{\boldsymbol{k}}^\dagger b_{\boldsymbol{k}} + s_{-\boldsymbol{k}} a_{\boldsymbol{k}} b_{\boldsymbol{k}}^\dagger - \gamma a_{\boldsymbol{k}}^\dagger a_{\boldsymbol{k}} - \gamma b_{\boldsymbol{k}}^\dagger b_{\boldsymbol{k}}) \tag{4.5}$$

where the in-plane structure factor $s_{\boldsymbol{k}}$ is given by

$$s_{\boldsymbol{k}} = \frac{1}{3}\sum_{\delta} e^{i\boldsymbol{k}\cdot\boldsymbol{\delta}} = \frac{1}{3}\left(e^{ik_y d} + 2\cos\frac{\sqrt{3}}{2}k_x d\, e^{-i\frac{k_y d}{2}}\right) \tag{4.6}$$

42

Similar term can be obtained for the bottom layer. Then for the interlayer couplings, there are four nearest neighbor couplings of the form

$$H_{\text{inter},2}^{\text{AC}} = -J_2 S \sum_{\boldsymbol{k}} (e^{i\boldsymbol{k}\cdot\boldsymbol{\rho_1}} a_{\boldsymbol{k}}^\dagger c_{-\boldsymbol{k}}^\dagger + e^{-i\boldsymbol{k}\cdot\boldsymbol{\rho_1}} a_{\boldsymbol{k}} c_{-\boldsymbol{k}} + \gamma a_{\boldsymbol{k}}^\dagger a_{\boldsymbol{k}} + \gamma c_{\boldsymbol{k}}^\dagger c_{\boldsymbol{k}}) \tag{4.7}$$

where $\boldsymbol{\rho_1} = \sqrt{3}/3\hat{\mathbf{x}}$ is the displacement from site A to site C. Similar Hamiltonians can be obtained for couplings between A and D, B and D, B and C. Performing a special diagonalization procedure explained in [132], we find the eigen energies for the Γ point magnons

$$E_{\text{a}} = S\sqrt{3(\gamma-1)J_1\big[3(\gamma-1)J_1 - 4J_2\big]} \pm g_S \mu_{\text{B}} B \tag{4.8}$$

$$E_{\text{o}} = S\sqrt{3(\gamma+1)J_1\big[3(\gamma+1)J_1 - 4J_2\big]} \pm g_S \mu_{\text{B}} B \tag{4.9}$$

where $S = \frac{3}{2}$ and $g_S = \frac{1}{2}$ for Cr^{3+}. The second solution above gives much higher energy and corresponds to the optical magnons. The first solution is the acoustic magnons that are doubly-degenerate at zero magnetic field but split linearly with non-zero fields. To explain the slight non-degeneracy at zero field [Fig. 4.3(a)], we postulate that the bFM should provide an effective field B_0 to the surface layers even without applying external fields. This field is estimated from the energy difference to be around 0.27 T.

Similar calculation is done for the bFM or overall FM cases below or after $B_c = 2$ T, where a single FM layer is considered. This yields the energy of the acoustic magnon

$$E_{\text{a}} = 3S(\gamma-1)J_1 + g_S \mu_{\text{B}} B \tag{4.10}$$

This mode only shows an energy redshift with respect to the external magnetic field, which means the field tends to align the spins and disfavors spin excitation. This also agrees with our observation.

By comparing our calculated and fitted magnon energies in Fig. 4.3(a), we extract the energy parameters for the system and summarize them in Tab. 4.1. Since we only detect

the acoustic magnons where the excited spins in the same layer tilt in the same direction, only the intralayer exchange anisotropy $(\gamma - 1)J_1$ can be extracted. It is desired to measure the optical magnon frequency in a future work such that the individual values of J_1 and γJ_1 can be obtained.

	Below 2 T	Above 2 T
Intralayer exchange anisotropy $(\gamma - 1)J_1$	0.065 meV	0.056 meV
Interlayer exchange coupling J_2	-0.074 meV	
Effective field from bFM B_0	0.27 T	

Table 4.1: Energy parameters for sAFM and bFM states from fitting spin waves measured in bulk CrI$_3$.

4.3 Magnetism-dependent phonon scattering

4.3.1 Phonon selection rules

Noting the reported structural phase transition from monoclinic C_{2h} to rhombohedral S_6, as well as a clear structural response to the formation of the FM order [116], we expect to see certain forms of coupling between the magnetic order and the crystal structure in bulk CrI$_3$. A detailed symmetry analysis based on the structure change helps resolve the outstanding question why and how the FM in bulk CrI$_3$ crosses over to the layered AFM in thin films, as introduced in Section 4.1. In this regard and through polarized Raman measurements with magnetic field dependence, we conduct selection rule analysis on the other Raman modes accessed in our experiments to gather structure information.

In Tab. 4.2 we summarize the Raman tensors for both monoclinic C_{2h} and rhombohedral S_6 structures as well as their Raman selection rules according to Eq. (2.20). Specifically we have included an anti-symmetric (AS) mode as well as its selection rule in the table. This is deduced from two special modes that will be discussed soon in this section.

We compare the selection rules with phonon Raman scattering data in Fig. 4.4(a)–(c),

	LL	LR
S_6	$\mathrm{A_g} = \begin{pmatrix} a & 0 \\ 0 & a \end{pmatrix}$, $\mathrm{AS} = \begin{pmatrix} 0 & b \\ -b & 0 \end{pmatrix}$	$\mathrm{E_g} = \begin{pmatrix} c & d \\ d & -c \end{pmatrix}$
C_{2h}	$\mathrm{A_g} = \begin{pmatrix} a & 0 \\ 0 & b \end{pmatrix}$	$\mathrm{A_g} = \begin{pmatrix} a & 0 \\ 0 & b \end{pmatrix}$, $\mathrm{B_g} = \begin{pmatrix} 0 & c \\ c & 0 \end{pmatrix}$

Table 4.2: Raman tensors and corresponding selections rules for rhombohedral S_6 and monoclinic C_{2h} point groups.

which show external magnetic field dependent Raman spectra of phonons measured at low temperature $T = 10$ K and with circular polarizations. At zero magnetic field with the rhombohedral S_6 symmetry [Fig. 4.4(a)], according to Tab. 4.2, LL and LR channels should probe exclusively $\mathrm{A_g}$ + AS and $\mathrm{E_g}$ modes, respectively. Thus the modes appearing only in LR channels [129] around 109 cm^{-1} and 239 cm^{-1} are attributed to the $\mathrm{E_g}$ irrep, though the latter has slight leakage into LL. From an earlier study [125] it is shown that the two modes M_1 at around 77.3 cm^{-1} and M_2 at around 125.8 cm^{-1} must be associated with an anti-symmetric Raman tensor since they do not appear in the parallel linear polarization channel [see later in Section 5.4 and Eq. (5.16)]. Lastly the two modes at around 79 cm^{-1} and 129 cm^{-1} in the LL channel are left to belong to the $\mathrm{A_g}$ irrep.

It is not expected for a phonon mode to possess anti-symmetry in the Raman process [46]. Early studies in magnetic semiconducting chalcogenide materials EuX (X = S, Se, Te) [133–135] have revealed similar magnetic order dependent activation of Raman modes or scattering intensity increase, which is then attributed to the one phonon-one spin scattering [136–138]. In our case, note that both M_1 and M_2 disappear after pulling the whole system to an overall FM state after $B_c = 2$ T as shown in Fig. 4.4(b) and (c), and that the temperature dependence of their intensities reveal their onsite at the magnetism ordering temperature $T_c = 45$ K. Such observations signal the magnetic origin of these two modes.
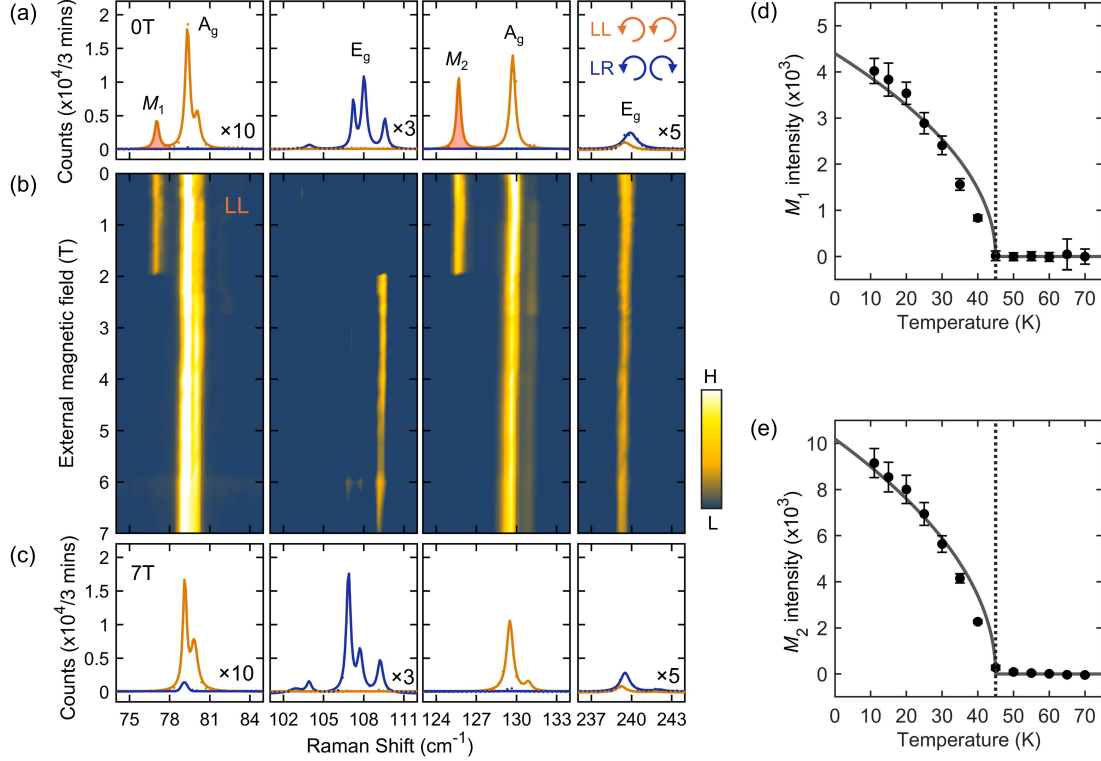
Figure 4.4: Phonon modes in bulk CrI$_3$ measured by Raman Scattering. (a) Raman spectra taken at 10 K and 0 T in the LL and LR channels. (b) A color map of magnetic field-dependent Raman spectra taken over a magnetic field range of 0-7 T at 10 K in the LL channel. (c) Raman spectra taken at 10 K and 7 T in the LL and LR channels. (d)–(e) Temperature dependence of the fitted M_1 and M_2 intensities measured at 0 T. The solid grey lines represent an onsite behavior with $T_c = 45$ K.

4.3.2 Antisymmetric "phonon" modes

We propose that M_1 or M_2 is the composite excitation of the $\boldsymbol{c}^*$ direction zone-boundary phonon $\boldsymbol{X^q}$ at $\boldsymbol{q} = (0, 0, k_c)$ together with the AFM order $\boldsymbol{M^{-q}}$ with wavevector $-\boldsymbol{q}$. This composition preserves the total momentum of zero so that it is detectable by optical Raman scattering. To obtain the selection rule of this excitation $\boldsymbol{X^q M^{-q}}$, we perform an expansion of the Raman polarizability α_{ij} with respect to both the phonon mode and the AFM order. This yields the magnetic dependent contribution

$$\Delta\alpha_{ij} = \left.\frac{\partial^2 \alpha_{ij}}{\partial X_k^{\boldsymbol{q}} \partial M_l^{-\boldsymbol{q}}}\right|_{X_k^{\boldsymbol{q}}=0,\, M_l^{-\boldsymbol{q}}=0} X_k^{\boldsymbol{q}} M_l^{-\boldsymbol{q}} \equiv K_{ijkl} X_k^{\boldsymbol{q}} M_l^{-\boldsymbol{q}} \qquad (4.11)$$

where K_{ijkl} defined above must be invariant under the symmetry operations of the lattice point group S_6. There are in total 27 independent elements for this tensor [40]

$$K_{zzzz}, \quad K_{xxxx} = K_{yyyy} = K_{xxyy} + K_{xyyx} + K_{xyxy},$$

$$K_{xxyy} = K_{yyxx}, \quad K_{xyyx} = K_{yxxy}, \quad K_{xyxy} = K_{yxyx},$$

$$K_{yyzz} = K_{xxzz}, \quad K_{xyzz} = -K_{yxzz}, \quad K_{zzyy} = K_{zzxx}, \quad K_{zzxy} = -K_{zzyx},$$

$$K_{zyyz} = K_{zxxz}, \quad K_{zxyz} = -K_{zyxz}, \quad K_{yzzy} = K_{xzzx}, \quad K_{xzzy} = -K_{yzzx},$$

$$K_{yzyz} = K_{xzxz}, \quad K_{xzyz} = -K_{yzxz}, \quad K_{zyzy} = K_{zxzx}, \quad K_{zxzy} = -K_{zyzx},$$

$$K_{xxxy} = -K_{yyyx} = K_{yyxy} + K_{yxyy} + K_{xyyy},$$

$$K_{yyxy} = -K_{xxyx}, \quad K_{yxyy} = -K_{xyxx}, \quad K_{xyyy} = -K_{yxxx},$$

$$K_{yyyz} = -K_{yxxz} = -K_{xyxz} = -K_{xxyz}, \quad K_{yyzy} = -K_{yxzx} = -K_{xyzx} = -K_{xxzy}$$

$$K_{yzyy} = -K_{yzxx} = -K_{xzyx} = -K_{xzxy}, \quad K_{zyyy} = -K_{zyxx} = -K_{zxyx} = -K_{zxxy}$$

$$K_{xxxz} = -K_{xyyz} = -K_{yxyz} = -K_{yyxz}, \quad K_{xxzx} = -K_{xyzy} = -K_{yxzy} = -K_{yyzx}$$

$$K_{xzxx} = -K_{yzxy} = -K_{yzyx} = -K_{xzyy}, \quad K_{zxxx} = -K_{zxyy} = -K_{zyxy} = -K_{zyyx}$$

The Onsager relation [53] $\Delta\alpha_{ij}(\boldsymbol{X}, \boldsymbol{M}) = \Delta\alpha_{ji}(\boldsymbol{X}, -\boldsymbol{M})$ must hold for the magneto-Raman process. Considering this further constraint, we find the following expressions for the Raman

polarizability

$$\Delta\alpha_{xx} = \Delta\alpha_{yy} = \Delta\alpha_{zz} = 0$$

$$\Delta\alpha_{yx} = -\Delta\alpha_{xy} = -X_z M_z K_{xyzz}$$

$$+\frac{1}{2}\big[(X_y M_x - X_x M_y)(K_{xyxy} - K_{xyyx}) + (X_x M_x - X_y M_y)(K_{yxyy} - K_{xyyy})\big]$$

$$\Delta\alpha_{zx} = -\Delta\alpha_{xz} = \frac{1}{2}\big[(X_x M_x - X_y M_y)(K_{zxxx} - K_{xzxx})$$

$$+(X_y M_x + X_x M_y)(K_{yzyy} - K_{zyyy}) + X_x M_z(K_{zyyz} - K_{xzxz}) \qquad (4.12)$$

$$+X_y M_z(K_{zxyz} - K_{xzyz}) + X_z M_x(K_{zyzy} - K_{yzzy}) + X_z M_y(K_{zxzy} - K_{xzzy})\big]$$

$$\Delta\alpha_{zy} = -\Delta\alpha_{yz} = \frac{1}{2}\big[(X_x M_x - X_y M_y)(K_{yzyy} - K_{zyyy})$$

$$+(X_y M_x + X_x M_y)(K_{xzxx} - K_{zxxx}) + X_x M_z(K_{xzyz} - K_{zxyz})$$

$$+X_y M_z(K_{zyyz} - K_{yzyz}) + X_z M_x(K_{xzzy} - K_{zxzy}) + X_z M_y(K_{zyzy} - K_{yzzy})\big]$$

It is apparent from the above equations that the tensor $\Delta\alpha_{ij}$ in this expansion is anti-symmetric of the form expressed in Tab. 4.2, thus explains the selection rule for modes M_1 and M_2. This finding also gives the second piece of evidence for the existence of an AFM order in the bulk CrI$_3$ system.

4.4 Structural phase transition due to magneto-elastic coupling

We now pay attention to the apparent change of selection rules of those phonon modes across $B_c = 2$ T, as shown in Fig. 4.4(a)–(c) and in [129]. Combining the LL and LR spectra, we note three prominent features. Firstly, the anti-symmetric modes M_1 and M_2 disappear completely, indicating the loss of the AFM order. Second, the previously LL-exclusive A$_g$ modes at 79 cm^{-1} and 130 cm^{-1} become active in the LR channel. Third, the previously LR-exclusive E$_g$ modes, while maintaining part of their intensities in the LR channel, show

noticeable presence in the LL channel. This is a strong indication of the E_g modes splitting due to lowering of symmetry. Indeed, comparing with Tab. 4.2 one find good agreement with the selection rules of point group C_{2h} for the state above $B_c = 2$ T. The intensity change of several typical modes are plotted in Fig. 4.5(a).

We propose the shearing of the van der Waals layers as the origin of the S_6 to C_{2h} structural phase transition, which is realized by the interlayer shift vector deviating from that of an A-B-C stacking order [Fig. 4.1(c) and 4.5(e)]. This type of interlayer shift has been experimentally reported elsewhere as a structural instability for bulk CrI_3 [116, 139]. Interestingly, this magnetic-field-induced monoclinic phase mimics a 3D long-range nematic order with a director as its order parameter which breaks the rotational symmetry but preserves the lattice translational symmetry, indicated by the elongated ellipses in Fig. 4.5(e)]. It is known that such a 3D quantum nematic order must emerge through the first-order phase transition [140], compatible with our proposed structural phase transition. In contrast to conventional structural transitions, the emergence of this 3D quantum nematic order is driven by an external magnetic field that has a much stronger coupling to electrons than to ions, supporting an electronic origin for this structural transition. One natural mechanism for it could be that this interlayer shear deformation increases the distance between the nearest interlayer spins and thereby reduces the exchange energy penalty for the field-induced layered AFM to FM transition. The revealing of this phase transition further demonstrates the rich phase diagram for this material and provides solid evidence of a strong coupling between the structure (stacking orders) and the magnetic interactions. This not only explains the puzzling evolution from the FM in bulk to the layered AFM in 2D CrI_3, but proves CrI_3 as an ideal platform to explore a variety of external controls such as electric field, strain, and charge-carrier doping, on the magnetism and its interplay with other degrees of freedoms.
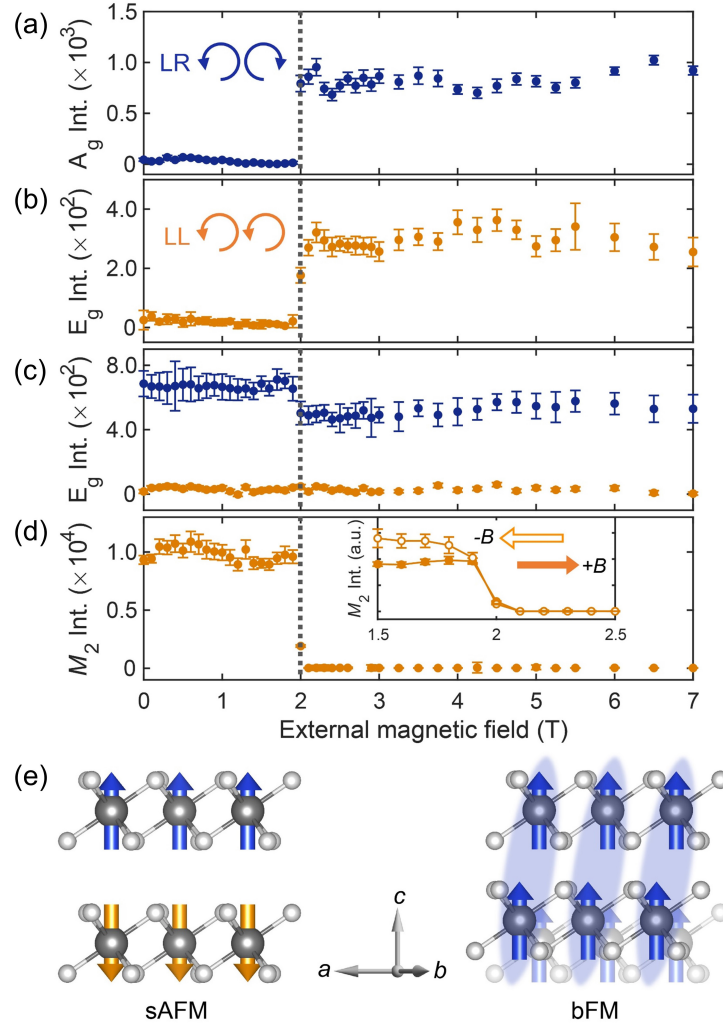
Figure 4.5: Revealing the rhombohedral-to-monoclinic structural phase transition at B_c in bulk CrI_3. Magnetic field dependence of (a) a representative A_g phonon (at 129 cm^{-1}) intensity leakage into the LR channel, (b) an example of an E_g phonon (at 109 cm^{-1}) intensity showing up in the LL channel, which corresponds to the E_g phonon of the S_6 structure becoming the A_g phonon of the C_{2h} structure, (c) an example of the E_g phonon (at 240 cm^{-1}) intensity experiencing a clear discontinuity in the LR channel but remaining absent in the LL channel corresponding to the E_g phonon becoming a B_g phonon, and (d) M_2 mode intensity. Inset shows an enlargement between 1.5 and 2.5 T with both increasing $(+B)$ and decreasing $(-B)$ magnetic fields. (e) Schematic illustration of the shearing of CrI_3 layers across the magnetic phase transition at B_c. The light blue ellipses represent the directors between layers formed as a result of this lattice deformation.

CHAPTER 5

Moiré Engineering in tDB CrI$_3$

5.1   Moiré engineering in the spin degree of freedom

Moiré engineering has revolutionized the field of condensed matter physics by enabling the precise and flexible control [17] of electronic properties through the deliberate stacking of 2D atomic layers at specific angles. This technique has led to the discovery of numerous exotic electronic states, such as flat bands induced strong correlation physics [11, 12, 141–147], nontrivial topological phases [148–153], and exotic exciton properties [154–158]. By creating a moiré superlattice, the periodic potential landscape is modified, resulting in new emergent phenomena that are not present in the parent layers. This concept of moiré engineering, initially explored in the electronic degree of freedom, has now extended its reach to the spin degree of freedom [16, 159–163], offering exciting possibilities in the realm of magnetism.

Moiré engineering provides a powerful platform to manipulate magnetic properties at the nanoscale. By twisting magnetic layers relative to each other, one can introduce frustration and complex magnetic interactions within the moiré supercell, leading to novel magnetic textures and phases formed in beyond atom-to-atom length scales. This approach allows researchers to explore the interplay between moiré patterns and spin arrangements, potentially unveiling new magnetic phenomena such as non-collinear spin textures [159, 161] and topological magnetic states [163]. In addition to the fundamental interests, the ability to engineer and control these magnetic properties opens up new avenues for the development

of advanced spintronic or magnonic applications [164–169].

As partly demonstrated in Chapter 4, the van der Waals magnetic material CrI_3 is particularly well-suited for exploring moiré engineering in the spin degree of freedom. We have shown the strong magneto-elastic coupling in this material as well as specifically its capability of FM to AFM crossover through the change of lateral interlayer shift. Such properties exactly align with what moiré engineering of magnetism is calling for—the modulation of magnetic interactions as a function of local atomic structures.

In summary, the exploration of moiré engineering in the spin degree of freedom using CrI_3 offers a promising pathway to discover and manipulate novel magnetic states. This chapter will delve into the optical characterization of moiré-engineered magnetism in twisted double-bilayer (tDB) CrI_3. By understanding the intricate relationship between various stacking orders and the corresponding magnetic interactions unlocked through twisting, we highlight an experimentally found unexpected FM order rising from parent antiferromagnets together with the formation of noncollinear spin textures.

5.2   tDB CrI_3 and the moiré superlattice

We fabricate tDB CrI_3 homostructures with two individual bilayer CrI_3. The structure of the system is shown in Fig. 5.1(a). Within each parent bilayer, the stacking order is monoclinic. The twist is introduced at the middle interface between the two bilayers and that is the playground where moiré engineering is supposed to happen. In Fig. 5.1(b) top, we show a false-color optical image of a typical tDB CrI_3 sample that was made by tearing a large piece of 2L CrI_3 [Fig. 5.1(b), bottom] into two and then stacking the pieces vertically at a controlled twist angle of α. Before being brought for other characterizations, the sample is further protectively sandwiched between two few-layer hexagonal boron nitride (hBN) flakes to avoid surface reactions with oxygen and moisture in the ambient environment.
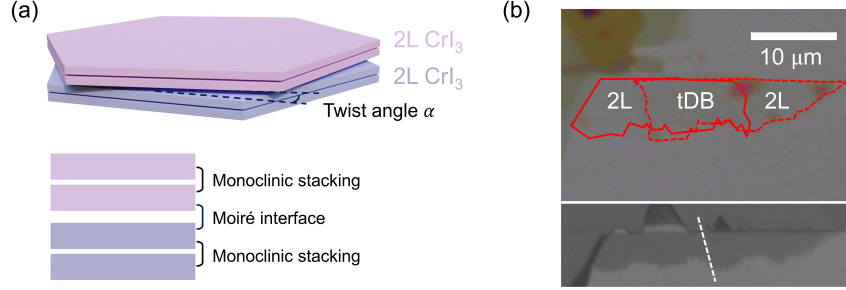
Figure 5.1: tDB CrI$_3$. (a) Sketch of a tDB CrI$_3$ sample made of two bilayer CrI$_3$ with a twist angle α between them. A moiré superlattice forms at the interface between the two bilayers, whereas individual bilayer CrI$_3$ has its own monoclinic stacking. (b) False-colored optical images of a tDB CrI$_3$ homostructure (top) with two bilayer CrI$_3$ constituents outlined with red lines and the original large-size 2L CrI$_3$ flake (bottom) with the tearing boundary marked with a white dashed line.

5.2.1   High quality moiré superlattice imaged by TEM

We verify that our tDB CrI$_3$ sample hosts a high-quality moiré superlattice, using selected area electronic diffraction (SAED) and dark-field transmission electron microscopy (DF-TEM). Figure 5.2(a) shows the zoom-in SAED pattern of tDB CrI$_3$ with a twist angle of $\alpha = 1.4\pm0.1°$, where the uncertainty comes from the fitted Bragg peak width. In addition to the three pairs of Bragg peaks [black circles in Fig. 5.2(a)] from the two constituting bilayer CrI$_3$ lattices, we also observe two additional diffraction peaks [blue circles in Fig. 5.2(a)] located beside the Bragg ones, which correspond to the second-order moiré superlattice diffraction. This clear observation of superlattice peaks in the diffraction pattern is a direct and solid evidence of the formation of moiré superlattices [101].

Figure 5.2(b) further shows three real-space DF-TEM images taken from within the SAED region, acquired by selecting the $(0\bar{3}30)$, $(\bar{3}300)$ and $(30\bar{3}0)$ Bragg and moiré superlattice reflections, respectively. Consistent with the presence of superlattice diffraction peaks, the DF-TEM image for every channel clearly shows the parallelogram feature. We comment that without the two superlattice diffraction peaks one would only observe parallel lines in the same DF-TEM measurements. In that situation the periodicity of the moiré superlattice were absent, and that would indicate a minimal coupling between the two flakes. Figure
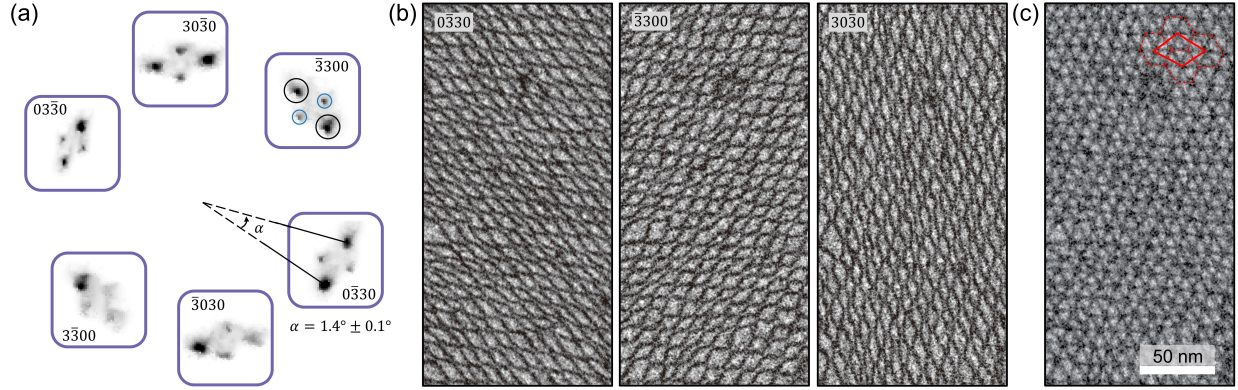
Figure 5.2: SAED and DF-TEM of high-quality moiré superlattice in tDB CrI$_3$. (a) Zoom-in SAED pattern showing the Bragg peaks for the two CrI$_3$ honeycomb lattices (black circles) and the second-order moiré superlattice diffraction peaks (blue circles). The measured twist angle for this sample is $\alpha = 1.4 \pm 0.1°$. (b) DF-TEM images of the same local region on the sample. Each image is acquired by selecting a pair of Bragg and superlattice diffraction peaks, labelled by the corresponding Bragg peak indices. (c) A composite image formed by summing up the three DF-TEM images in (b), showing a uniform, high-quality superlattice. The red parallelogram indicates the moiré supercell whose area is three times that of the original unit cell.

5.2(c) is a composite image made by summing up the three DF-TEM images in Fig. 5.2(b). It shows the superlattice structure marked by the red parallelogram uniformly extending over an area of approximately 250×125 nm^2.

5.2.2 The choice of twisted double-bilayer over twisted bilayer

We briefly comment on our choice of 2L CrI$_3$ as the building blocks to form a twisted double-bilayer, instead of using 1L CrI$_3$ for a twisted bilayer. It has been found in practice, that the phonon mode mostly involving the c-direction vibration of the I ions [170] shows a much narrower linewidth in bilayer CrI$_3$ as opposed to that in a monolayer, as displayed in Fig. 5.3. The satellite peak in the 2L case represents the magnetism-coupled mode whose origin is similar to what is explained in Section 4.3. This side peak is also of narrow linewidth. Similar findings have been reported in other independent studies as well [171, 172]. Such narrow linewidths suggest a much better crystalline and magnetic integrity in 2L CrI$_3$

than in 1L. This helps ensure the high quality moiré superlattice formed by two bilayers as demonstrated in the previous section. We also note few TEM studies have shown moiré superlattices as good as in our tDB sample.
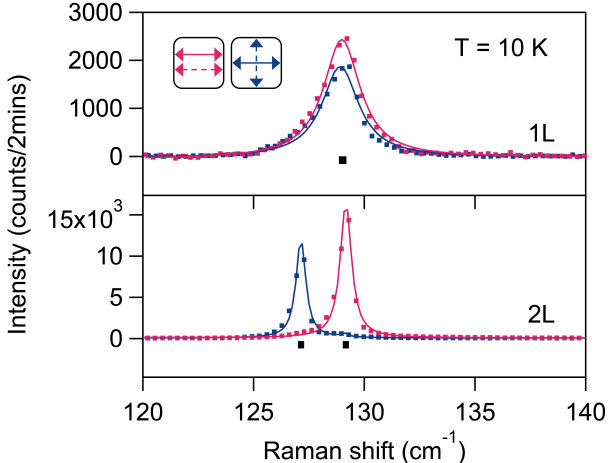
Figure 5.3: Raman spectra of a phonon mode in 1L and 2L CrI$_3$ acquired in linear parallel (red) and crossed (blue) polarization channels at 10 K. The solid curves are fits to the raw data (dots). Figure adapted from [170].

Accompanying the mediocre quality of the Raman fingerprint of 1L CrI$_3$, it is actually challenging to obtain good 1L CrI$_3$ samples at the first place. The practical difficulties include an extremely low yield of 1L CrI$_3$ after exfoliation, small size ($\sim$ a few µm) flakes not suitable for the "tear-and-stack" technique, and the faster degrade whose timescale is usually shorter than the common sample loading and cooling time required for optical characterization.

5.3 Simulated magnetic ground states in tDB CrI$_3$

The magnetic ground state in semiconducting CrI$_3$ (gap size ~ 1.1 eV without too much variation from bulk to thin-film systems [173, 174])—schematically characterized by the periodically ordered arrangement of the spin vectors—is governed by the exchange interaction between the Cr^{3+} spins, mathematically with terms like $-J\mathbf{S}_i \cdot \mathbf{S}_j$. This model provides a framework for understanding how neighboring spins interact, and thus determining the

ground state configuration.

5.3.1 Stacking-dependent interlayer exchange interaction

In CrI_3, with a layered perspective, the intralayer exchange interaction is ascribed to a Cr-I-Cr super-exchange with a somewhat close to 90° bond angle [175], which greatly favors a FM coupling according to the Goodenough-Kanamori rules [176–179]. The interlayer exchange interaction, however, originates from the super-super-exchange through the two I ions across the van der Waals gap. This interlayer orbital pathway is extremely sensitive to the relative displacement between the two layers and thus responsible for a stacking order dependent interlayer exchange interaction [139, 179–182]. As an example, in natural bilayer CrI_3 as shown in Fig. 5.4, the intralayer exchange interaction $J_{intra} = 2.2$ meV/μ_B^2 is strongly FM, whereas the interlayer exchange at this monoclinic stacking $J_{inter} = -0.04$ meV/μ_B^2 is a much weaker AFM interaction [139]. This combination will prefer a layered AFM as the magnetic ground state [113, 183]. On the other hand, in a bulk CrI_3 system where the layers are rhombohedrally stacked, the interlayer exchange is calculated to be 0.6 meV/μ_B^2 [139], which together with the positive J_{intra} will favor an overall FM ground state. This discussion explains the crossover from the bulk FM order to the layered AFM order in 2D CrI_3.
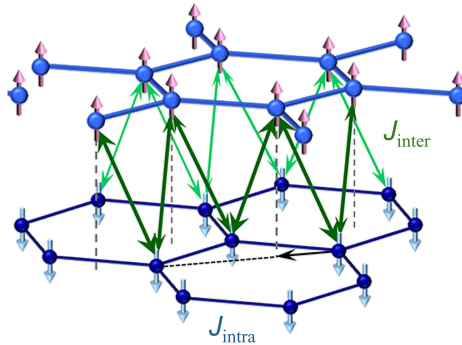
Figure 5.4: Schematic for the intralayer and interlayer exchange couplings in two adjacent layers of Cr^{3+} spins. Figure adapted from [139].

Moiré engineering provides the playground where a continuous distribution of stacking

orders can be introduced at the twist interface, and thus creating a distribution of the interlayer exchange interaction $J_{\mathrm{moiré}}(\mathbf{r})$, where $\mathbf{r}$ runs over the moiré supercell. Looking at two honeycomb lattices with a small angular mismatch illustrated in Fig. 5.5(a), within a moiré supercell indicated by the black parallelogram, one can identify three—overlying (AA), rhombohedral (R) and monoclinic (M)—typical types of stacking orders. In between those specific positions the local atomic registry evolves continuously. We take the following interpolation method to obtain the function $J_{\mathrm{moiré}}(\mathbf{r})$ for next-step simulations. First, from reported *ab*-initio calculations [139], we get the following four interaction values

Stacking order	$\mathbf{r}$	$J_{\mathrm{moiré}}$ (meV/μ_{B}^2)
AA	$(0,0)$	0.11
R	$(0, \dfrac{\sqrt{3}}{3})$	0.6
M	$(\dfrac{1}{3}, 0)$	-0.04
M	$(\dfrac{2}{3}, 0)$	-0.05

Table 5.1: Calculated typical interlayer exchange interaction values in a moiré supercell. Data points taken from [139].

Noting the moiré system still possesses the threefold rotational symmetry and the function $J_{\mathrm{moié}}(\mathbf{r})$ is even with respect to inversion, we use cosine functions up to the second-harmonic as the basis functions for interpolation

$$J(\mathbf{r}) = J_0 + J_1 \sum_{i=1}^{3} \cos(\mathbf{k}_i^{(1)} \cdot \mathbf{r}) + J_2 \sum_{i=1}^{3} \cos(\mathbf{k}_i^{(2)} \cdot \mathbf{r} + \phi) \tag{5.1}$$

where J_0, J_1, J_2 and ϕ are parameters to be determined through interpolation. The two sets

of wavevectors are given by

$$\mathbf{k}_1^{(1)} = \mathbf{b}_2, \qquad \mathbf{k}_2^{(1)} = -\mathbf{b}_1, \qquad \mathbf{k}_3^{(1)} = \mathbf{b}_1 - \mathbf{b}_2$$

$$\mathbf{k}_1^{(2)} = 2\mathbf{b}_2 - \mathbf{b}_1, \quad \mathbf{k}_2^{(2)} = -\mathbf{b}_1 - \mathbf{b}_2, \quad \mathbf{k}_3^{(2)} = 2\mathbf{b}_1 - \mathbf{b}_2$$

(5.2)

where $\mathbf{b}_1 = 2\pi(1, \frac{\sqrt{3}}{3})$ and $\mathbf{b}_2 = 2\pi(0, \frac{2\sqrt{3}}{3})$ are the two in-plane reciprocal primitive vectors. Within each harmonics, the three wavevectors $\mathbf{k}_{1,2,3}^{(i)}$ are mutually $120°$ to each other and thus preserve the threefold rotational symmetry. Interpolating with the target function in Eq. (5.1) and the values in Tab. 5.1 we obtain the distribution function that is plotted in Fig. 5.5(b).
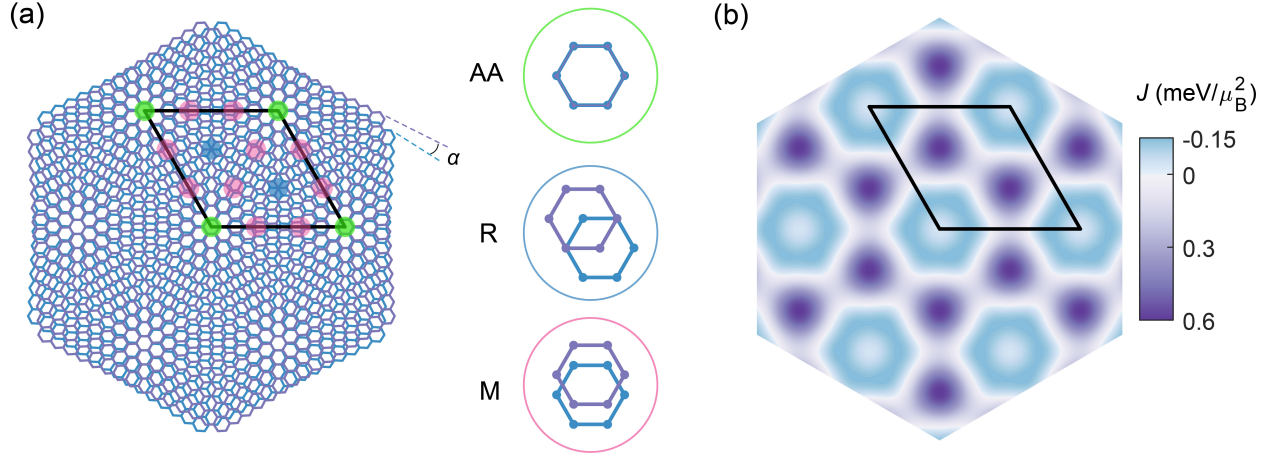
Figure 5.5: (a) The moiré superlattice formed at the interface between two 2L CrI$_3$. Regions of AA- (green), R- (blue) and M-type (red) stacking geometries are marked in one moiré supercell (black parallelogram), and highlighted on the right column. (b) The periodically modulating interlayer exchange interaction $J_{\mathrm{moiré}}(\mathbf{r})$ at the interface between two 2L CrI$_3$, obtained through interpolation.

This moiré interlayer exchange coupling $J_{\mathrm{moiré}}(\mathbf{r})$ periodically varies from AFM type [blue in Fig. 5.5(b)] to FM type [purple in Fig. 5.5(b)]. This means the spins at moiré interface experience spatially modulated J_{inter} "vertically". At the same time, the strong intralayer FM type (2.2 meV/μ_B^2, much stronger than $\max |J_{\mathrm{moiré}}|$) exchange interaction highly favors the configuration of uniform out-of-plane spins within one Cr^{3+} layer. It is the competition between these two exchange couplings that determines the magnetic ground state in tDB

CrI$_3$. Ultimately, this is what moiré engineering in spin systems does—changing the way these layers stack on top of each other and then leading to different magnetic configurations through modulating the interlayer exchange interactions.

5.3.2 Twist angle dependent magnetic ground states

We construct the total magnetic Hamiltonian of a tDB system by including the intralayer exchange coupling, the easy-axis anisotropy, the interlayer AFM exchange coupling within each bilayer, and the modulated interlayer exchange coupling between the two bilayers

$$H = \sum_{l=1}^{4} H_{\text{intra}}^{(l)} + H_{\text{M}}^{(1,2)} + H_{\text{moiré}}^{(2,3)} + H_{\text{M}}^{(3,4)} \tag{5.3}$$

where $H_{\text{intra}}^{(l)}$ denotes the intralayer couplings in the l-th layer, and the following three terms represent the interlayer couplings for all three interfaces. For the coupling between layer 1 and 2, and between layer 3 and 4, the exchange interaction takes the monoclinic value J_{M}; for the coupling between layer 2 and 3, the function $J_{\text{moiré}}(\mathbf{r})$ is used.

We seek to minimize the total energy in Eq. (5.3) in the parameter space of all possible spin orientations. First consider the following intralayer coupling Hamiltonian

$$H_{\text{intra}}^{(l)} = -J_{\text{intra}} \sum_{\langle i,j \rangle} \left(S_{i,x}^{(l)} S_{j,x}^{(l)} + S_{i,y}^{(l)} S_{j,y}^{(l)} + \gamma S_{i,z}^{(l)} S_{j,z}^{(l)} \right) \tag{5.4}$$

where $\langle i,j \rangle$ denotes a pair of nearest-neighbor Cr^{3+} spins. If we ignore the quantum fluctuations, each spin vector on site i can be represented as $\mathbf{S}_i^{(l)} = S\mathbf{n}_i^{(l)}$ where $\mathbf{n}_i^{(l)} = (n_{i,x}^{(l)}, n_{i,y}^{(l)}, n_{i,z}^{(l)})$ is a 3D unit vector and $S = \frac{3}{2}\mu_{\text{B}}$ for Cr^{3+} ions. For the twist angles that we consider (for example, intermediate twist angles such as $\sim 1°$), the moiré wavelength is about ~ 40 nm, and the magnetization in each layer varies slowly in real space. Therefore we can take the continuum limit, replacing $\mathbf{n}_i^{(l)}$ with a smooth 3D function $\mathbf{n}^{(l)}(\mathbf{r})$. Then the Hamiltonian in

Eq. (5.4) becomes

$$H_{\text{intra}}^{(l)} = -J_{\text{intra}}S^2 \sum_{\langle i,j \rangle} \left[n_x^{(l)}(\mathbf{r}_i)n_x^{(l)}(\mathbf{r}_j) + n_y^{(l)}(\mathbf{r}_i)n_y^{(l)}(\mathbf{r}_j) + \gamma n_z^{(l)}(\mathbf{r}_i)n_z^{(l)}(\mathbf{r}_j) \right] \quad (5.5)$$

In this continuum limit, we can perform a Taylor expansion, taking $\delta\mathbf{r} = \mathbf{r}_i - \mathbf{r}_j$ as a small parameter

$$n_m^{(l)}(\mathbf{r}_i)n_m^{(l)}(\mathbf{r}_j) = n_m^{(l)}(\mathbf{r}_i)^2 + n_m^{(l)}(\mathbf{r}_i)\delta\mathbf{r}\cdot\boldsymbol{\nabla}n_m^{(l)}(\mathbf{r}_i) + \frac{1}{2}n_m^{(l)}(\mathbf{r}_i)(\delta\mathbf{r}\cdot\boldsymbol{\nabla})^2 n_m^{(l)}(\mathbf{r}_i) + O(\delta r^3) \quad (5.6)$$

where $m = x, y, z$. Because the anisotropy factor $\gamma = 1.0445$ in CrI$_3$ is close to 1 [184], we take the approximation that, for the leading order term $n_m^{(l)}(\mathbf{r}_i)^2$ we keep $\gamma = 1.0445$, while for higher order terms, we set $\gamma = 1$. This approximation simplifies the Hamiltonian without changing any qualitative features (that is, we use n^2 terms to describe the easy-axis spin anisotropy of CrI$_3$, while the derivatives of $\mathbf{n}(\mathbf{r})$ still preserve the SU(2) spin rotational symmetry). With this approximation, the Hamiltonian in Eq. (5.5) becomes

$$H_{\text{intra}}^{(l)} = -J_{\text{intra}}S^2 \sum_{\text{unit cell}} \left[3\left(n_x^{(l)2} + n_y^{(l)2} + \gamma n_z^{(l)2} \right) - \frac{3}{4}\delta r^2 \left| \boldsymbol{\nabla}\mathbf{n}^{(l)} \right|^2 \right] \quad (5.7)$$

Here, first order derivative terms cancel out, while the second order derivative terms can be written as $\propto |\boldsymbol{\nabla}\mathbf{n}|^2 = \sum_{l=x,y}\sum_{m=x,y,z}(\partial_l n_m)^2$. Higher order terms beyond $O(\delta r^2)$ are ignored. For the honeycomb lattice of Cr^{3+} ions, $\delta r = a/\sqrt{3}$ where a is the lattice constant. The sum in Eq. (5.7) over all unit cells can further be replaced by the real-space integral $\sum_{\text{unit cell}} \to \frac{1}{\mathscr{A}}\iint \mathrm{d}x\mathrm{d}y$ where $\mathscr{A} = \frac{\sqrt{3}}{2}a^2$ is the area of one unit cell. This way the Hamiltonian in Eq. (5.7) becomes

$$H_{\text{intra}}^{(l)} = -\frac{J_{\text{intra}}S^2}{\mathscr{A}} \iint \left[-\frac{a^2}{4}\left| \boldsymbol{\nabla}\mathbf{n}^{(l)} \right|^2 + 3\left(n_x^{(l)2} + n_y^{(l)2} + \gamma n_z^{(l)2} \right) \right] \mathrm{d}x\mathrm{d}y \quad (5.8)$$

Similarly we can write down the interlayer exchange coupling Hamiltonians

$$H_{\mathrm{M}}^{(1,2)} = -\frac{2J_{\mathbf{M}}S^2}{\mathscr{A}} \iint \mathbf{n}^{(1)} \cdot \mathbf{n}^{(2)} \mathrm{d}x\mathrm{d}y \tag{5.9}$$

$$H_{\mathrm{M}}^{(3,4)} = -\frac{2J_{\mathbf{M}}S^2}{\mathscr{A}} \iint \mathbf{n}^{(3)} \cdot \mathbf{n}^{(4)} \mathrm{d}x\mathrm{d}y \tag{5.10}$$

$$H_{\mathrm{moiré}}^{(2,3)} = -\frac{2S^2}{\mathscr{A}} \iint J_{\mathrm{moiré}}\mathbf{n}^{(2)} \cdot \mathbf{n}^{(3)} \mathrm{d}x\mathrm{d}y \tag{5.11}$$

To obtain the spin configuration for the lowest energy in this continuous model, we discretize a moiré unit cell using a triangular grid of $L \times L \times 4$, and define the following effective Hamiltonian on this grid

$$H_{\mathrm{intra}}^{(l)} = -\frac{J_{\mathrm{intra}}S^2}{3} \sum_{\langle i,j \rangle} \mathbf{n}_i^{(l)} \cdot \mathbf{n}_j^{(l)} - \frac{3J_{\mathrm{intra}}S^2}{(\alpha L)^2} \sum_i \left(n_{i,x}^{(l)\,2} + n_{i,y}^{(l)\,2} + \gamma n_{i,z}^{(l)\,2} \right) \tag{5.12}$$

$$H_{\mathrm{M}}^{(1,2)} = -\frac{2J_{\mathbf{M}}S^2}{(\alpha L)^2} \sum_i \mathbf{n}_i^{(1)} \cdot \mathbf{n}_i^{(2)} \tag{5.13}$$

$$H_{\mathrm{M}}^{(3,4)} = -\frac{2J_{\mathbf{M}}S^2}{(\alpha L)^2} \sum_i \mathbf{n}_i^{(3)} \cdot \mathbf{n}_i^{(4)} \tag{5.14}$$

$$H_{\mathrm{moiré}}^{(2,3)} = -\frac{2S^2}{(\alpha L)^2} \sum_i J_{\mathrm{moiré}}\mathbf{n}_i^{(2)} \cdot \mathbf{n}_i^{(3)} \tag{5.15}$$

where α is the twist angle and $L = 60$ is the grid size. The dimensionless quantity $(\alpha L)^2 = \frac{\mathscr{A}}{\mathscr{A}_0}$, where $\mathscr{A}$ and $\mathscr{A}_0$ are the areas of a CrI$_3$ unit cell and a unit cell of this triangular grid, respectively.

We then minimize the total Hamiltonian via the quasi-Newton method in the $L \times L \times 4 \times 3$ parameter space. The magnetic ground states turn out to evolve as the twist angle α increases. The results at three representative twist angles ($\alpha = 0.1°$, $1°$ and $10°$) are shown in Fig. 5.6(a)–(c). At very small twist angles such as $0.1°$ [state I in Fig. 5.6(a)], out-of-plane magnetization M_z is spatially modulated in both the first and second layers, while remaining antiparallel between the two layers. In the third and fourth layers the M_z is homogeneous, being downwards ($\downarrow$, $m_z = -3\mu_{\mathrm{B}}$) in layer 3 and upwards ($\uparrow$, $m_z = 3\mu_{\mathrm{B}}$) in layer 4. We
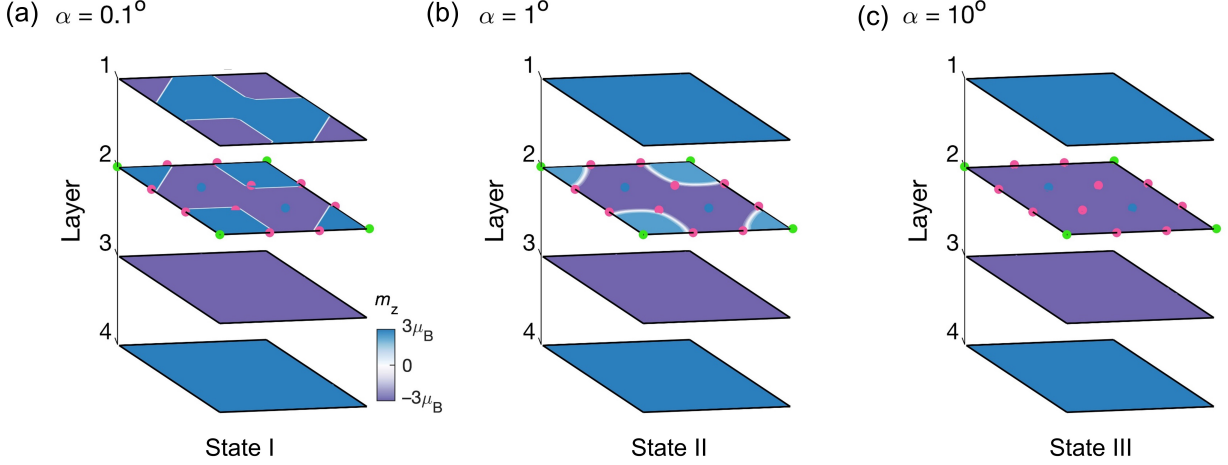
Figure 5.6: (a)–(c), The calculated distributions of the out-of-plane magnetization M_z in a moiré supercell for all four layers of a tDB CrI$_3$ at three representative twist angles $\alpha = 0.1°$ (a), 1° (b), and 10° (c).

further correlate the "vertical", layered spin configurations with the local stacking orders. The islands centering at AA-stacked sites take the $\mathbf{M}_1 = \downarrow\uparrow\downarrow\uparrow$ layered magnetic order, and the large remaining area centering at R-stacked sites has the $\mathbf{M}_2 = \uparrow\downarrow\downarrow\uparrow$ layered magnetism. The boundaries between the two regions in the top bilayer exhibit the non-collinear spin texture ($\searrow\nearrow$ in layer 1 and $\nearrow\searrow$ in layer 2). At intermediate twist angles such as 1°, the computed magnetic ground state [state II in Fig. 5.6(b)] shows modulated spins only in the second layer which features islands with non-compensated magnetization ($\mathbf{M}_3 = \uparrow\uparrow\downarrow\uparrow$) centering at AA-stacked sites. The $\mathbf{M}_2 = \uparrow\downarrow\downarrow\uparrow$ order persists for R-stacked sites. As a result, non-collinear spins form up in layer 2 at the boundaries between the two regions, which primarily consist of M-stacked sites. At large twist angles such as 10°, the calculated result shows homogeneous spins within all four layers [state III in Fig. 5.6(c)] and they take the $\mathbf{M}_2 = \uparrow\downarrow\downarrow\uparrow$ layered magnetic order all over the moiré supercell.

If excluding the domain wall regions where the non-collinear spins reside, we summarize, in Tab. 5.2, the aforementioned layered magnetic orders appearing in the three states shown in Fig. 5.5(a)–(c), where +1 (−1) denotes up- (down-) spins. We note that order $\mathbf{M}_1$ is essentially the layered AFM order reported in natural 4L CrI$_3$ [113]; order $\mathbf{M}_2$ shows

FM alignment between layer 2 and 3 due to the FM exchange interaction around the R-stacked sites; order $\mathbf{M}_3$ is most special in the sense that it exhibits a non-compensated net magnetization and only appears at intermediate twist angles.

state I	$\mathbf{M}_1 = (-1, 1, -1, 1)$	$\mathbf{M}_2 = (1, -1, -1, 1)$	
state II		$\mathbf{M}_2 = (1, -1, -1, 1)$	$\mathbf{M}_3 = (1, 1, -1, 1)$
state III		$\mathbf{M}_2 = (1, -1, -1, 1)$	

Table 5.2: Appearance of different types of layered magnetic orders in the three simulated magnetic ground states.

While the details of the spin configurations may vary depending on the microscopic parameters in the model, the emergence of non-compensated magnetization only at intermediate twist angles and the formation of non-collinear spin textures for small to intermediate twist angles are robust features in our simulated moiré magnetism in tDB CrI$_3$. We shall then turn to the experimental evidence for those moiré engineered novel magnetic states.

5.4 Magnetism-coupled phonons as characterization of the magnetic ground states in tDB CrI$_3$

This section presents the Raman characterization of the moiré engineered novel magnetism in twisted tDB CrI$_3$. Recall the magnetism-dependent phonon scattering visited in Section 4.3 in bulk CrI$_3$, as well as similar Raman studies in 1L to 4L natural few-layer CrI$_3$ systems [170–172, 185], it has been established that the accompanying satellite anti-symmetric Raman modes around the fully symmetric A$_g$ phonon at around 129 cm^{-1} are sensitive to the layered magnetic orders [170].

Indeed as shown in Fig. 5.7 for a tDB CrI$_3$ sample with $\alpha = 1.1°$, U$^t_{2,3,4}$ peaks do not show up in the parallel polarization channel even when changing the azimuth angle. This
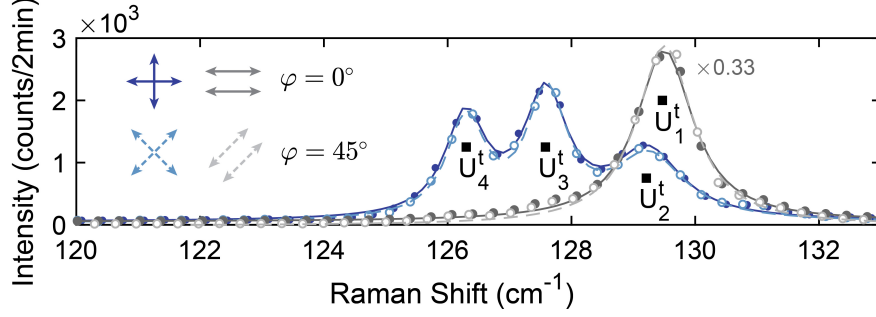
Figure 5.7: Raman spectra of the magnetism-coupled phonon modes taken on a 1.1° tDB CrI$_3$ sample as in both parallel (grey) and crossed (blue) channels at two azimuth angles $\varphi = 0°$ (filled circles and solid lines) and 45° (open circles and dashed lines) at 10 K. The parallel channel spectra are scaled by a factor of 0.33.

requires that for a general Raman polarizability $\left(\begin{smallmatrix} a & b \\ c & d \end{smallmatrix}\right)$ and azimuth angle φ, the term

$$
\begin{pmatrix} 1 & 0 \end{pmatrix} \begin{pmatrix} \cos\varphi & \sin\varphi \\ -\sin\varphi & \cos\varphi \end{pmatrix} \begin{pmatrix} a & b \\ c & d \end{pmatrix} \begin{pmatrix} \cos\varphi & -\sin\varphi \\ \sin\varphi & \cos\varphi \end{pmatrix} \begin{pmatrix} 1 \\ 0 \end{pmatrix} \\
= \frac{a-d}{2} \cos 2\varphi + \frac{c+b}{2} \sin 2\varphi + \frac{a+d}{2}
$$

(5.16)

must vanish for any φ. This implies $a = d = 0$ and $b = -c$. The Raman tensor is then anti-symmetric $\left(\begin{smallmatrix} 0 & b \\ -b & 0 \end{smallmatrix}\right)$. One can also verify that for anti-symmetric modes, the intensity in the crossed polarization channel will stay the same no matter the azimuth angle, in accordance with the observation in Fig. 5.7. As discussed in [170] and Section 4.3.2, the anti-symmetric Raman mode breaks the time-reversal symmetry and corresponds to the magnetism-coupled phonon scattering. This symmetry feature makes those modes the good and sensitive indicator for the magnetic order in the tDB CrI$_3$ system.

Having established the Raman signature for the magnetism of tDB CrI$_3$, we proceed to examine its twist angle dependence. Figure 5.8 shows the Raman spectra of those magnetism-coupled phonon modes taken on tDB CrI$_3$ for $\alpha = 0.5°, 1.1°, 2.0°, 5.0°$, as well as 4L and 2L CrI$_3$ in both crossed and parallel polarization channels at 10 K. Here one may perceive 4L as $\alpha = 0°$, and 2L as very large α due to that the inter-2L coupling strength in very large α tDB is very weak such that the tDB would essentially behave like two decoupled bilayers.

We observe that, as the twist angle α increases, the mode U$_3^t$ in the crossed channel
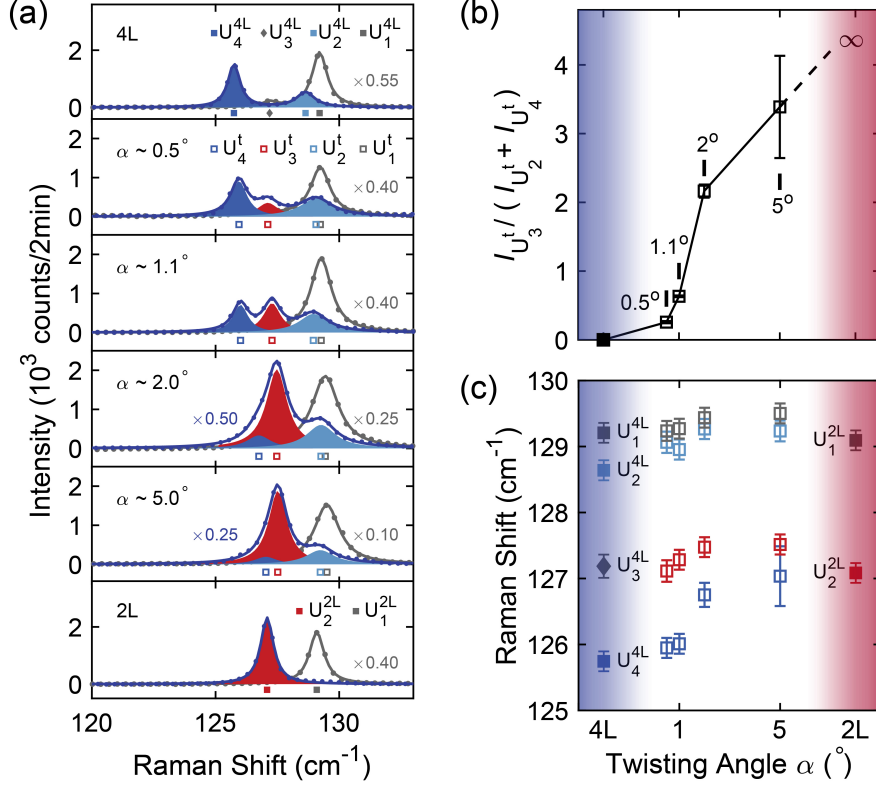
Figure 5.8: Twist angle dependence of the magneto-phonon Raman spectra of tDB CrI$_3$. (a) Raman spectra taken on 4L CrI$_3$; tDB CrI$_3$ with twist angles $\alpha = 0.5°, 1.1°, 2.0°, 5.0°$; and 2L CrI$_3$ in both crossed (blue) and parallel (grey) channels at 10 K. The colored Lorentzian profiles highlight the U$_{2,3,4}$ modes appearing in the crossed channel. (b) Intensity ratio $I_{U_3^t}/(I_{U_2^t} + I_{U_4^t})$ as a function of the twist angle α. (c) Fitted frequencies of the modes shown in (a) as a function of the twist angle α.

increases in intensity while the other two modes U$_{2,4}^t$ decrease, showing a continuous trend that the magneto-Raman spectra of a tDB evolves from resembling natural 4L at lower α to converging towards 2L at larger α. This intensity evolution is quantified in Fig. 5.8(b), where the relative intensity ratio $I_{U_3^t}/(I_{U_2^t} + I_{U_4^t})$ is plotted against α. The line shows a monotonous increase with larger α and thus confirms the modulating of the magnetic state upon twist. Equally informative is the frequency shift of the Raman modes, as shown in Fig. 5.8(c). It is noted that at smaller α, the frequencies of modes U$_{2,3,4}^t$ start very close to their counterparts U$_{2,3,4}^{4L}$ in 4L. Then with increasing α the frequencies of U$_{2,4}^t$ gradually blue-shifts towards those of U$_{1,2}^{2L}$. Note in our indexing, mode U$_2^{2L}$ is the counterpart of U$_3^{t/4L}$. The twist angle dependence of those modes also demonstrates we have successfully introduced moiré

65

engineering to the magnetic system in tDB CrI$_3$.

To relate our observation with the proposed moiré engineered states shown in Fig. 5.6, we take a semi-quantitative model from [170] to characterize the intensity change of, for example, U$_3^t$. Based on a linear-chain model for few-layer transition metal chalcogenides [186–189], the U$_3^t$ mode is attributed to an magnetism-coupled eigen vibration which involves the vertical movement of the I ions. The eigenvector of the vibration itself can be written down in terms the relative amplitudes of the I ions in four layers $\mathbf{u}_3 = \frac{1}{2}(1, -1, -1, 1)^T$.

The scattering amplitude of the anti-symmetric mode U$_3^t$ is then proportional to $\mathbf{u}_3 \cdot \mathbf{M}$ [170] where $\mathbf{M}$ is the layered magnetic order. Recall we have three types of layered magnetic orders $\mathbf{M}_{1,2,3}$ summarized in Tab. 5.2, and each order takes up a faction of area $c_{1,2,3}^{(\mathrm{I,II,III})}$. Here $c_j^{(i)}$ denotes the area fraction of order $\mathbf{M}_j$ in state i, where $i = \mathrm{I, II, III}$ represents the three states shown in Fig. 5.6. We also assume a negligible fraction of domain wall area so that all fractions for a given state sum up to 1. Hence we calculate

$$\mathbf{u}_3 \cdot \sum_{j=1}^{3} c_j^{(i)} \mathbf{M}_j = \begin{cases} 2c_2^{(\mathrm{I})} < 2, & \text{for state I} \\ 2c_2^{(\mathrm{II})} + c_3^{(\mathrm{II})} < 2, & \text{for state II} \\ 2c_2^{(\mathrm{III})} = 2, & \text{for state III} \end{cases} \tag{5.17}$$

The above result explains how the moiré engineered magnetic state can change the U$_3^t$ mode intensity. For example we note the $\mathbf{M}_2 = (1, -1, -1, 1)^T$ order gives the highest contribution to the scattering amplitude but its area fraction is small in states I and II. In states I, the $\mathbf{M}_1 = (-1, 1, -1, 1)^T$ order does not contribute any amplitude, while in state II the $\mathbf{M}_3 = (1, 1, -1, 1)^T$ order does contribute something but the efficiency is lower than that of $\mathbf{M}_2$. Overall, through this we see the twist angle dependence of those magnetism-coupled phonon modes captures the exotic layered magnetic states created by moiré engineering.

5.5 Magnetic field dependent studies of tDB CrI$_3$

In this section we provide magnetic field dependent optical studies of the novel magnetic orders in tDB CrI$_3$. The basis for this discussion lies on the experimental fact that for natural few-layer CrI$_3$ with layered antiferromagnetic order, there exist two spin-flip transitions at $B_{c1} \approx \pm 0.7$ T and $B_{c2} \approx \pm 1.6$ T, as shown in the field dependent MCD measurements in Fig. 5.9. According to the introduction in Section 2.3, one can perceive the normal incidence CD signal at non-resonance as $\propto M_z$. Therefore we would treat the MCD measurements in this section as direct probe of the net out-of-plane magnetization. In this sense, we attribute the sudden jumps shown in the MCD data in Fig. 5.9 to the abrupt change of M_z, or spin-flip transition.
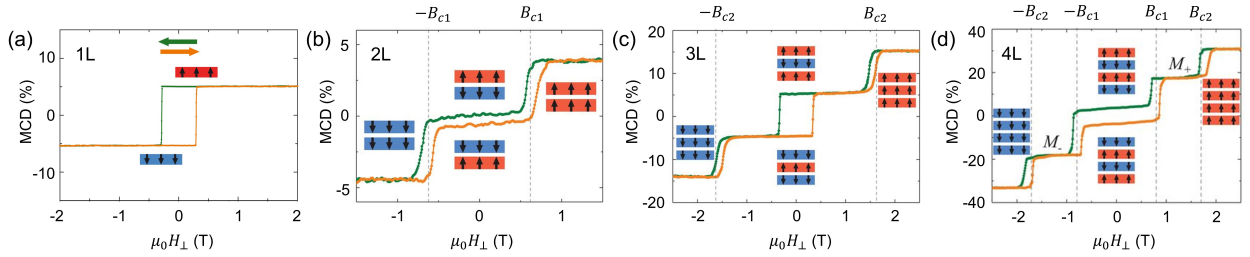
Figure 5.9: Magnetic field dependent MCD measurements on natural 1–4L CrI$_3$ and illustration for the corresponding layered magnetic orders. Figure adapted from [113, 190].

At B_{c1}, the spins in one of the two layers in 2L CrI$_3$, and those in the outermost layer in 4L CrI$_3$ flip. This transition costs one unit of interlayer exchange interaction. At B_{c2}, the spins in the middle layer in 3L CrI$_3$, and those in the third layer in 4L CrI$_3$ flip. This transition costs two units of interlayer exchange interaction. Such energy cost estimation agrees with the observation that B_{c2} is roughly twice B_{c1}. Apart from the spin-flip transitions we also note that for 1L and 3L CrI$_3$ at around 0 T the systems show non-zero MCD signal together with hysteresis. This is due to that for odd-layer CrI$_3$ the system has one extra layer of non-compensated moments which is responsible for the FM-like behavior.

The exploration of magnetic field dependence of tDB CrI$_3$ benefits from those observations in natural few-layer CrI$_3$, in the sense that one would expect changes of the layered magnetic

order at different fields. By comparing the field dependent behaviors in tDB with those basic cases, we aim to extract features characteristic of the novel moiré magnetism.

5.5.1 Magnetic field dependence of the magnetism-coupled phonon Raman Scattering

We further provide the magnetic field dependent Raman spectra of the magnetism-coupled phonon modes discussed in Section 4.3 for bulk CrI_3 and in Section 5.4 for tDB CrI_3. Figure 5.10(a)–(e) presents the false-color maps of raw phonon Raman spectra for 4L, $\alpha = 0.5°, 1.1°, 5°$ tDB and 2L CrI_3, in the crossed channel at 10 K. Figure 5.10(f)–(j) summarizes the corresponding $B_\perp$ dependencies of the fitted intensities of the magnetism-coupled phonons. We first briefly summarize the evolutions of U_{1-4}^{4L} and U_{1-2}^{2L} as the reference for understanding those of tDB CrI_3. For 4L CrI_3, $U_{1,3}^{4L}$ emerge at $B_{c1} \approx 0.7$ T, and then see sudden intensity increase and decrease, respectively, at $B_{c2} \approx 1.6$ T; $U_{2,4}^{4L}$ experience two consecutive steep intensity drops at B_{c1} and B_{c2}. It is understood from Fig. 5.9 that B_{c1} and B_{c2} correspond to two first-order spin-flip transitions for the layered magnetism transiting from $\mathbf{M}_1 = \downarrow\uparrow\downarrow\uparrow$ (layered AFM) first to $\mathbf{M}_3 = \uparrow\uparrow\downarrow\uparrow$ and then to $\uparrow\uparrow\uparrow\uparrow$ (fully polarized FM). For 2L CrI_3, U_1^{2L} appears and U_2^{2L} disappears concurrently at B_{c1}, where B_{c1} denotes the spin-flip transition from $\downarrow\uparrow$ to $\uparrow\uparrow$. We comment that the magnetic field dependent behaviors of these modes have been successfully explained in our earlier study in [170], the theory framework of which has been briefly discussed in Section 5.4.

For U_{1-4}^t modes in tDB CrI_3 at very small ($\alpha = 0.5°$) angle, their behaviors under $B_\perp$ can be well described by a simple weighted linear superposition of those of 4L and 2L CrI_3. Similar to the 4L case [Fig. 5.10(a) and (f)], 0.5° tDB CrI_3 features two transitions at B_{c1} and B_{c2} where sudden intensity changes of the modes U_{1-4}^t occur [Fig. 5.10(b) and (g)]. Different from the 4L case is that, U_3^t of 0.5° tDB CrI_3 is present even below B_{c1}, and the transitions are slightly broadened. We recall as discussed in Section 5.4, mode U_3^t displays the highest Raman efficiency in 2L-like tDB CrI_3 and specifically, in the presence of the
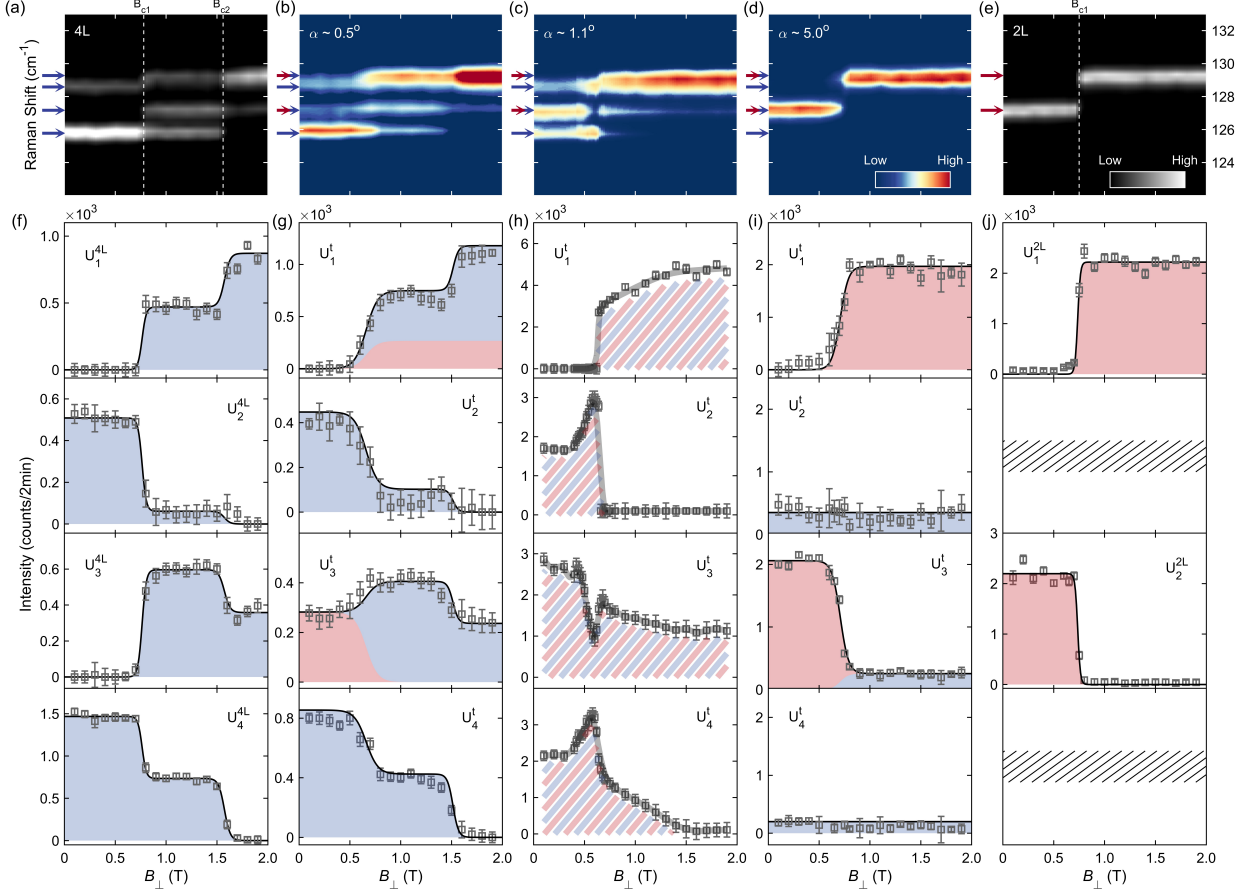
Figure 5.10: Magnetic field dependence of the magnetism-coupled phonon Raman spectra of tDB CrI$_3$ at selected twist angles. (a)–(e) False-colored maps of the raw Raman spectra taken on 4L CrI$_3$ (a); tDB CrI$_3$ homostructures with twist angles $\alpha = 0.5°$ (b), 1.1° (c), 5° (d); and 2L CrI$_3$ (e) in the crossed polarization channel at 10 K. The blue arrows mark the frequencies of U$_{1-4}^{4L}$ and the red ones are those of U$_{1-2}^{2L}$. (f)–(j) Plots of the mode intensities as a function of $B_\perp$ for the samples in (a)–(e), respectively. The thin black lines and solid shaded areas denote the fits to the model of the magnetism-coupled phonon scattering for 4L (f) and 2L (j) CrI$_3$, and to the proposed weighted superpositions of 4L and 2L contributions for tDB CrI$_3$ with $\alpha = 0.5°$ (g) and $\alpha = 5°$ (i). The thick grey lines and striped areas for 1.1° tDB CrI$_3$ in (h) are guides to the eye.

$M_2 = \uparrow\downarrow\downarrow\uparrow$ order. And this M_2 order is exactly predicted in state I in our simulations in Fig. 5.6(a) (see also Tab. 5.2) for small twist angles. Thus, the behaviors of U$_{1-4}^t$ in 0.5° tDB CrI$_3$ can be well accounted for by the weighted addition of the field dependencies of U$_{1-4}^{4L}$ and U$_{1,2}^{2L}$.

On the other hand, 5.0° tDB CrI$_3$ in Fig. 5.10(d) and (i) nearly reproduces the 2L CrI$_3$

results shown in Fig. 5.10(e) and (j), except for a minor remnant of U_3^t above B_{c1}. This observation confirms that $5.0°$ tDB CrI_3 is primarily regarded as two decoupled 2L CrI_3 without much complex spin textures, similar to our simulation in Fig. 5.6(c).

Interestingly, in stark contrast to $0.5°$ and $5.0°$ tDB CrI_3, the magnetic field dependence of those magnetism-coupled phonon modes in $1.1°$ tDB CrI_3 can no longer be simply understood by combining the behaviors of those modes in 4L/2L CrI_3. Figure 5.10(c) and (h) show two features for $1.1°$ tDB CrI_3 that are completely absent in 4L and 2L CrI_3. First, around B_{c1}, the intensities of $U_{2,4}^t$ show a dramatic spike, U_3^t exhibits a sharp dip. None shows the monotonous steps observed in 4L/2L CrI_3. Second, between B_{c1} and B_{c2}, U_1^t gradually increases until saturation, whereas $U_{3,4}^t$ slowly decrease towards a finite intensity or zero. Such behaviors are quite different from the otherwise plateaus observed in 4L/2L CrI_3. It is possible that for the intermediate twist angle like $\alpha = 1.1°$, the very existence of the non-collinear spins have caused these exotic critical behaviors around B_{c1}.

5.5.2   A model for fitting MCD of tDB CrI_3

Similar to Fig. 5.9, we show our MCD data in Fig. 5.11, as a function of the out-of-plane magnetic field $B_\perp$ swept from $+2$ T to -2 T and back to $+2$ T taken on $1.1°$ tDB CrI_3 (top panel), as well as 2L (middle panel) and 4L (bottom panel) CrI_3 for reference. Two prominent features are observed from the comparison between the $1.1°$ tDB data and the reference 2L/4L data, despite similar spin-flip transitions at $B_{c1}^{tDB} = \pm0.67$ T, $B_{c1}^{2L} = \pm0.73$ T, and $B_{c1}^{4L} = \pm0.82$ T. First, in $1.1°$ tDB CrI_3, the MCD signal at 0 T is non-zero, and the magnetic field dependence shows a clear hysteresis loop between B_{c1}^{tDB}, in sharp contrast to the almost zero MCD signal and absence of hysteresis in 2L/4L CrI_3. Second, for $1.1°$ tDB CrI_3, the MCD data show a gradual increase (positive slope) with increasing $B_\perp$, which is distinct from the plateau behavior of constant MCD values for 2L/4L CrI_3 when not in a spin-flip transition. We note that the non-zero MCD at 0 T and the hysteresis are the defining evidence for the existence of net magnetization in $1.1°$ tDB CrI_3. This is the result

of the most prominent, moiré induced $\mathbf{M}_3$ order shown in Fig. 5.6(b). Meanwhile, we point out that the gradual increase in MCD suggests the presence of a spin flop process and thus non-collinear spins in 1.1° tDB CrI$_3$, consistent with the in-plane spin moments residing at the boundaries between the $\mathbf{M}_3$ islands and the $\mathbf{M}_2$ background in Fig. 5.6(b).
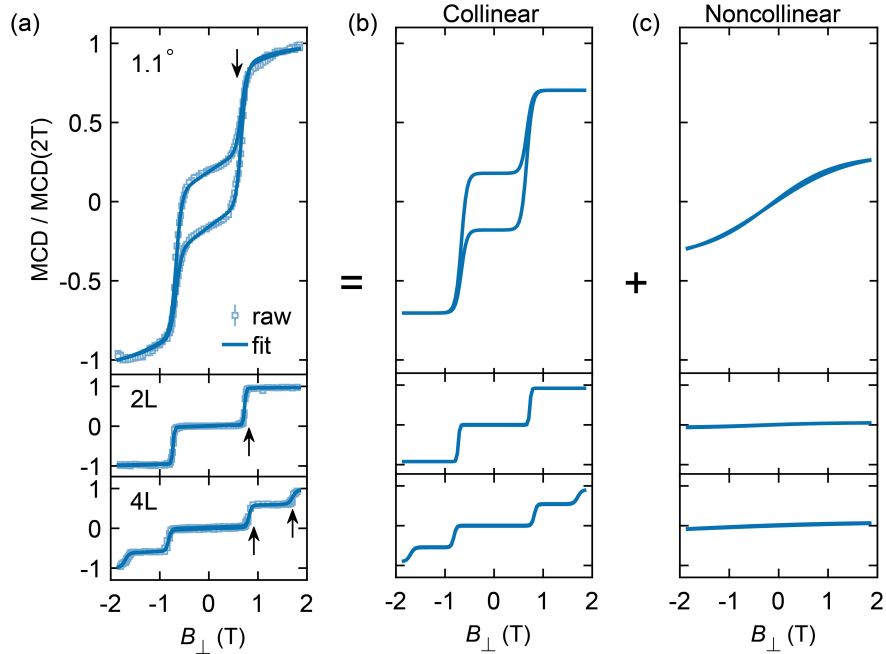
Figure 5.11: Magnetic field dependent MCD data and the fitting model. (a) MCD data and fits normalized to the MCD value at 2 T taken at 10 K under an out-of-plane magnetic field $B_\perp$ sweeping from +2 T to −2 T and then back to +2 T for 1.1° tDB (top), 2L (middle) and 4L (bottom) CrI$_3$. The spin flip transitions are marked by black arrows in all three panels. (b)–(c) Contributions from collinear (b) and non-collinear (c) spins to the total MCD signal, extracted from the fits for 1.1° tDB, 2L and 4L CrI$_3$.

We fit the MCD data of 1.1° tDB CrI$_3$ with the model consisting of two contributions: one from the collinear spins that give rise to the steep spin-flip transitions at B_c, and the other from the non-collinear spins accounting for the gradual spin flop process with increasing $B_\perp$. For the collinear spin contribution, the out-of-plane spins take two possible directions, up and down, with magnetic moments $\mu = \pm 2 \cdot \frac{3}{2}\mu_\mathrm{B} = \pm 3\mu_\mathrm{B}$. Boltzmann statistics dictates

that the mean magnetization under an external field $B_\perp$ follows the tanh dependence of $B_\perp$

$$\langle\mu\rangle = \frac{3\mu_{\mathrm{B}}\mathrm{e}^{\frac{3\mu_{\mathrm{B}}B_\perp}{k_{\mathrm{B}}T}} - 3\mu_{\mathrm{B}}\mathrm{e}^{-\frac{3\mu_{\mathrm{B}}B_\perp}{k_{\mathrm{B}}T}}}{\mathrm{e}^{\frac{3\mu_{\mathrm{B}}B_\perp}{k_{\mathrm{B}}T}} + \mathrm{e}^{-\frac{3\mu_{\mathrm{B}}B_\perp}{k_{\mathrm{B}}T}}} \sim \tanh\frac{3\mu_{\mathrm{B}}}{k_{\mathrm{B}}T}B_\perp \qquad (5.18)$$

For the non-collinear contribution, ideally slow-varying models such as Langevin or Brillouin functions [191] describing high-spin paramagnetic behaviors could be used. Without loss of basic information, we still take a tanh function, which is the essentially a special case of the two, to model the slow-varying non-collinear contribution. If we set x as the external magnetic field and $y_{+(-)}$ as the MCD signal in an increasing-field (decreasing-field) measurement, we use the following model for fitting the MCD curves

$$\begin{cases} y_+ = A_{\mathrm{neg}}\tanh\dfrac{x+B}{C} + A_{\mathrm{pos}}\tanh\dfrac{x-B}{C} + a_+\tanh\dfrac{x-b_+}{c_+} \\ y_- = A_{\mathrm{pos}}\tanh\dfrac{x+B}{C} + A_{\mathrm{neg}}\tanh\dfrac{x-B}{C} + a_-\tanh\dfrac{x-b_-}{c_-} \end{cases} \qquad (5.19)$$

For each equation, the first two terms explain the spin-flip transitions of Ising collinear spins and the third term represents the response of the non-collinear spins. $A_{\mathrm{neg(pos)}}$ describes the magnitude of the spin-flip transition, B and C are the critical field B_{c1} and transition width ΔB_{c1}, respectively. Those parameters are kept common in fitting y_+ and y_- datasets to satisfy the time-reversal symmetry requirement, that is, the increasing-field curve $y_+(x)$ and the decreasing-field curve $y_-(x)$ should map to each other when inverting about the origin at $x = 0$ and $y = 0$. For the non-collinear contribution, $a_\pm$, $b_\pm$ and $c_\pm$ describe the magnitude, center and width of the slowly varying background in either an increasing $(+)$ or decreasing $(-)$ measurement and are independent between the increasing and decreasing field traces.

The fits are shown in Fig. 5.10 for $1.1°$ tDB CrI_3 (top panels), 2L and 4L CrI_3 (middle and bottom panels). The solid fit curves in Fig. 5.11(a) are separated into the collinear and noncollinear components shown in Fig. 5.11(b) and (c), respectively. This fitting for $1.1°$ tDB CrI_3 is independent from but consistent with the simulated results in Fig. 5.6(b) in terms of

the following two aspects. First, the net magnetization as well as the hysteresis is from the collinear spin contribution [Fig. 5.11(b), top panel], consistent with magnetized islands with collinear $\mathbf{M}_3 = \uparrow\uparrow\downarrow\uparrow$ spin arrangements. Second, for the non-collinear spin contribution, the two fitted MCD traces [Fig. 5.11(c), top panel] with decreasing and increasing $B_\perp$ overlap with each other within our fit uncertainties, echoing the computed net zero out-of-plane magnetization at the boundaries between the $\mathbf{M}_3 = \uparrow\uparrow\downarrow\uparrow$ islands and the $\mathbf{M}_2 = \uparrow\downarrow\downarrow\uparrow$ background [white regions in Fig. 5.6(b)]. As a comparison, the fits for 2L and 4L CrI$_3$ are seen to be dominated by the collinear spin contribution with well compensated magnetizations below $B_{c1}^{2L/4L}$ [Fig. 5.11(b), middle and bottom panels]. They also show negligible non-collinear spin contributions [Fig. 5.11(c), middle and bottom panels]. All the consistency here demonstrates that we can take advantage of MCD and this two-component fitting model to gain information about the complicated moiré magnetic states formed upon twist.

5.5.3 Twist angle dependent MCD measurements

We explore the twist angle dependence of moiré magnetism through MCD measurements. Figure 5.12 displays the raw normalized MCD data together with fits (top panel), and contributions from collinear (middle panel) and non-collinear (bottom panel) spins, for 4L, $\alpha = 0.5°, 1.1°, 2°, 5°, 10°$ tDB, and 2L CrI$_3$. A general trend can be seen that, the MCD data resemble those of 4L CrI$_3$ at very small twist angles (for example, 0.5°) in having two spin-flip transitions, then distinguish from both 4L and 2L CrI$_3$ at intermediate twist angles (for example, 1.1°, 2° and 5°) by showing a prominent hysteresis loop as well as appreciable non-collinear spin contribution, eventually converge to those of 2L CrI$_3$ at large twist angles (for example, 10°). To better quantify this trend, we plot the twist angle dependence of five important parameters extracted from the fits: the spin-flip transition field B_{c1} that corresponds to the interlayer coupling strength within each bilayer [Fig. 5.12(b)], the width of the spin-flip transitions ΔB_{c1} that describes the spatial inhomogeneity of moiré magnetism

[Fig. 5.12(c)], the slope $\Delta\mathrm{MCD}/\Delta B_\perp$ at 0 T that depicts the susceptibility of the non-collinear spins [Fig. 5.12(d)], the ratio $W_\mathrm{non-collinear}$ of the non-collinear spin contribution to the total MCD which scales with the weight of the non-collinear spins [Fig. 5.12(e)], and the magnitude of net magnetization at 0 T (remanence) M_z^tDB. We describe the twist angle dependent behaviors of those parameters below.
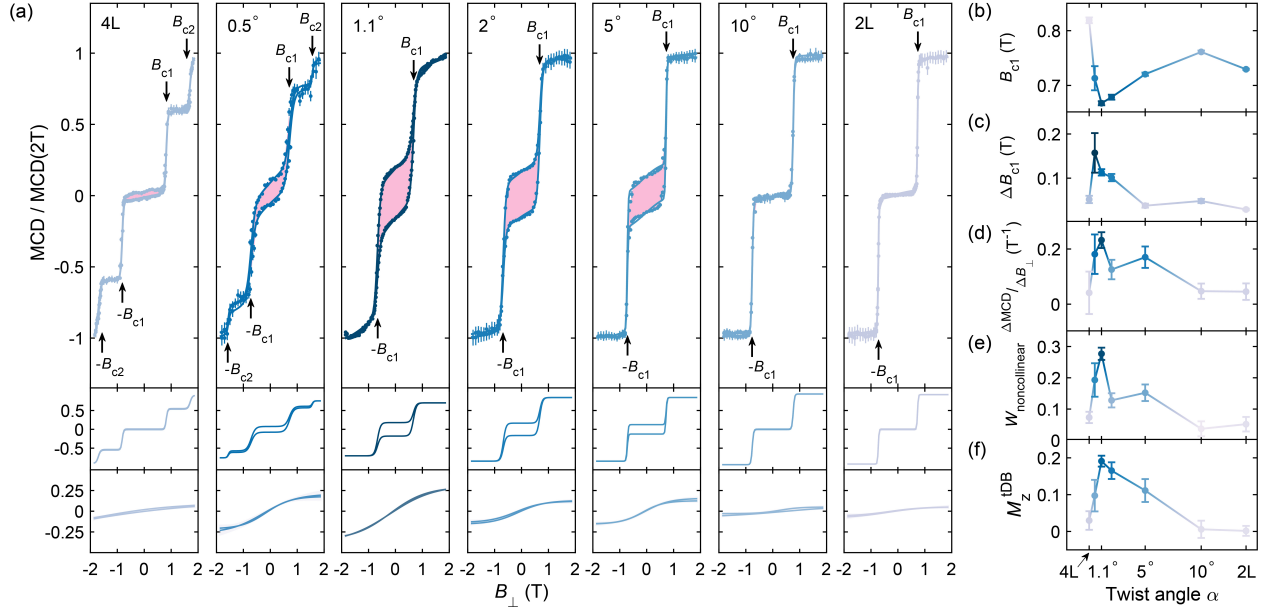
Figure 5.12: Twist angle dependence of MCD data of tDB CrI$_3$. (a) Normalized MCD data and fits (top panel) taken at 10 K under $B_\perp$ sweeping from $+2$ T to -2 T and then back to $+2$ T, for 4L, $\alpha = 0.5°, 1.1°, 2°, 5°, 10°$ tDB, and 2L CrI$_3$, showing hysteresis loops (pink shades) and spin flip transitions (black arrows). Contributions from the collinear (middle panel) and the non-collinear (bottom panel) spins are extracted from the model fitting. (b)–(f) Twist angle dependence of the spin-flip transition field B_{c1} (b), the spin-flip transition width ΔB_{c1} (c), the slope $\Delta\mathrm{MCD}/\Delta B_\perp$ at 0 T (d), the weight of the non-collinear spin contribution $W_\mathrm{non-collinear}$ (e), and the net magnetization M_z^tDB (f), extracted from the fitting.

A minimum in B_{c1} at $1.1°$ in Fig. 5.12(b) shows that the moiré interlayer coupling introduced between layer 2 and 3 actually modifies the uniform interlayer coupling between layer 1 and 2 or 3 and 4, considering this transition should only flip the outermost layer spins. This impact maximizes at $1.1°$. A maximum of ΔB_{c1}, however, happens at $0.5°$ in Fig. 5.12(c), most probably resulting from the extra 4L-like region—the $\mathbf{M}_1 = \uparrow\downarrow\uparrow\downarrow$ order shown in Fig. 5.6(a)— which is marked by the presence of B_{c2} in $0.5°$ tDB CrI$_3$. We note

this magnetic order is shown absent in tDB CrI_3 with higher twist angles. The slope of tDB CrI_3 is obviously larger than those of 2L and 4L CrI_3 and peaks at 1.1° [Fig. 5.12(d)], which evidences the softening of the moiré-induced non-collinear spins. The non-collinear spin weight shown in Fig. 5.12(e) also maximizes at 1.1°, further suggesting the prevalence of those in-plane spins at this twist angle. Lastly, the remarkable net magnetization M_z^{tDB}, a clear indicator of state II moiré magnetism shown in 5.6(b), peaks at 1.1° [Fig. 5.12(f)]. Such systematic non-monotonic twist angle dependence, consistent across almost all the parameters, well demonstrates the key role of twist angle, or equivalently moiré wavelength, in the emergent magnetic properties in tDB CrI_3.

In summary, through magnetic field dependent optical study of tDB CrI_3, we reveal features in both MCD and magneto-Raman scattering for the moiré engineered novel magnetism. Specifically, we highlight the emergence of net FM, out of two antiferromagnet parents, and non-collinear spin textures, out of a simple collinear structure, in tDB CrI_3 with intermediate twist angles such as 1.1°. The plethora of behaviors and properties for different twist angles and under different magnetic fields prove our successful moiré engineering of the spin system in CrI_3 and the versatility of moiré magnetism.

CHAPTER 6

Closing Remarks

In summary, this thesis presents the utilization of three types of optical techniques: second-harmonic generation, Raman Scattering and magnetic circular dichroism. Each emphasizes distinct forms of light-matter interaction, manifested by the modulations of the permittivity tensor that links the controlled incident field polarization and the reflected radiation fields. During the dissertation research, we have carefully chosen proper optical probes to characterize the multivarious dipolar orders in either $1T$-TaS$_2$ or CrI$_3$ systems.

SHG is highly suitable for detecting subtle or non-traditional symmetries due to the distinguishing high-rank tensor forms for different point group symmetries. We selectively study the familiar, yet symmetry-wise less considered ferro-rotational CDW order in $1T$-TaS$_2$. It is noted that, by sending in essentially a tensor field $\mathbf{EE}$ for the SHG process instead of a common electric field or polar vector $\mathbf{E}$, the SI-even, rotational vector that transforms as $\mathbf{r} \times \mathbf{P}$ can be probed. This differs from the traditional philosophy for detecting a ferroic order where a conjugate field is applied. There is currently no well-defined conjugate field for the ferro-rotational or ferro-toroidal orders [192]. The way the ferro-rotational order manifests itself in RA SHG—rotation away from the pristine crystal axes as in Fig. 3.4—is rather straightforward and distinct.

SHG process is of electronic origin. A quantum interpretation of the ED SHG suscepti-

bility tensor reads [193]

$$\chi_{ijk}^{(2),\text{ED}} \propto \sum_{m,f} \frac{\langle g|r_i|f\rangle\langle f|r_j|m\rangle\langle m|r_k|g\rangle}{(E_f - E_g - 2\hbar\omega)(E_m - E_g - \hbar\omega)} + \cdots \tag{6.1}$$

where the summation runs over excited intermediate state (m) and final state (f), and the ellipsis could in principle contain other two-photon pathways where the system does not start from the ground state (g). Unlike diffraction methods directly sensing the charge density distribution, the contributions to the SHG susceptibility tensor elements, which then compose the apparent RA patterns, root in the electronic bands. The "system" we discuss in terms of symmetry should actually refer to the electronic system. In this sense, it is advisable or even beneficial to acquire a methodology where the band structure enters the comprehension of SHG response. In light of early endeavor [194], such work has been carried out specifically in topological systems [195, 196]. To apply the similar formalism in the SHG measurements of the insulating CDW state could be of potential interests. It is admittedly, a harder task to study the EQ process for this purpose, in a centrosymmetric system such as $1T$-TaS_2. A feasible starting point could be, for example, to identity the irreps of the participating SHG susceptibility tensor elements and relate them, through quadrupole transition selection rules, to the calculated band structure. To connect the SHG response to band structure will also help interpret the ultrafast behaviors such as the origin of the triplet modes discussed in Section 3.3.1.

The ferro-rotational order hosts other possibilities. In a thorough group theory analysis [102], 12 pure ferro-rotational species are identified with 8 of them being fully ferro-rotational (namely, the rotational vector can serve as the sole order parameter). This classification provides the map to search for ferro-rotational order candidates based on a pure symmetry consideration. In fact, the reported SHG studies on ferro-rotational orders mostly base on materials with D_{3d} to S_6 phase transition [25, 32, 197, 198], partially because normal incidence SHG would vanish in the presence of an out-of-plane C_2 axis. Therefore, oblique

incident SHG experiments are required to examine other types of ferro-rotational phase transitions.

The study of CrI_3, or the moiré magnetism, is still blooming. To be able to engineer magnetic exchange interaction through a method as handy as twist is fortuitous. In CrI_3 it truly relies on the strong magneto-elastic coupling, which even makes it possible to realize not just strength, but sign changes—variation from AFM to FM—of the exchange interaction. In tDB CrI_3 it is the emergence of FM interlayer interaction at the moiré interface that gives rise to the energy competition/frustration, and essentially the exotic magnetic structure and properties that are discussed in Chapter 5. Specifically, we predict and experimentally evidence the existence of non-compensated FM domains and non-collinear spins residing in the domain walls, through optical signatures. It has then been desired to visualize such domains or domain walls via microscopy, which to some extent however, only sees macroscopic FM domains and due to the current resolution limit is not capable to inspect "sub-moiré" features [190, 199, 200]. The origin of the seemingly disordered large FM domains observed in twisted bilayer CrI_3 in scanning magnetometry experiments is still unclear, though the manifestation of a clear twist angle dependence in our tDB CrI_3 (Fig. 5.12) strongly hints that our systems are very less likely subject to such "random" disorders. It is possible, as briefly argued in Section 5.2.2, that the monolayer CrI_3 tends to have worse crystalline quality that essentially caused twist bilayer samples suffering from various types of strains or defects. Having said so, to study the effects of defects or strains in CrI_3 systems is of fundamental interest and importance as well.

The non-collinear spins embrace more interesting physics. In a sense, the non-collinear spin order comprises longer wavelength structure and includes a large number of spin degrees of freedom. Novel collective spin excitations, such as the long-sought skyrmions or topological magnons [162, 201–203] are predicted to exist in twisted 2D magnetic van der Waals systems. Those excitations are emergent, and very different from spin-flips, which also indicates that they are intrinsically hard to create from, for example a spin-flip process such as in neutron

scattering. moiré engineering benefits from the fact that through a careful examination of the stacking-dependent exchange interaction, the resulting non-collinear magnetic states are very much expected or at least approachable before-hand via theory simulations [161, 163].

Our simulations elaborated on in Section 5.3 are qualitatively robust. The prediction of the exact phase boundaries (namely critical twist angle) as well as the actual fraction of both the FM patches and the non-collinear spins is yet greatly determined by the microscopic parameters. A key consideration here is to solidify the distribution function of the interlayer exchange interaction at the moiré surface. Magnetic moiré engineering is stacking engineering in nature. Nevertheless, the quantification of the stacking orders at the moiré interface may not be as plain as what is shown in Fig. 5.5(a). Atomic reconstruction is widely present in incommensurately-stacked van der Waals materials and has been studied in twist graphene or transition metal dichalcogenide semiconductors [204–208], and is even a signature of good moiré coupling. In our tDB Cr_3 samples this is so well manifested though the existence of the moiré superlattice satellite peaks shown in Fig. 5.2(a). To accommodate this lattice relaxation into the calculation of exchange interactions could be of high priority to advance the study of moiré magnetism in twisted CrI_3.

The study of quantum materials has never been accomplished by just a few experimental probes, while optics does provide a more versatile and multifaceted solution, especially for the current 2D community where the small scattering volume and sample size restrict the usage of other powerful techniques such as neutron scattering or quantum oscillation. Microscopic methods are quickly progressing, though the "sub-moiré" resolution is not yet fully achieved. In this regard, to see through the moiré length scale out of a coarse, large laser beam and the long wavelength of visible light is truly demanding. This mission is not limited to the 2D field but also faced by the study of, for example, altermagnetic materials [209]. But one is never let down by the shining light. It has so many degrees of freedom: polarization, in a sense spin angular momentum; wavelength; photon energy; orbital angular momentum [210]; spatial mode; and even temporal profile in an ultrafast setting. An orchestration of the

versatility of light still opens promising avenues for future research on all kinds of quantum materials.

BIBLIOGRAPHY

[1] Sang-Wook Cheong. 5th Anniversary of npj Quantum Materials. *npj Quantum Materials*, 6(1):68, 2021.

[2] Philip W. Anderson. More is different: Broken symmetry and the nature of the hierarchical structure of science. *Science*, 177(4047):393–396, 1972.

[3] E. M. Lifshitz and L. P. Pitaevskii. *Statistical Physics: Part 2.* Butterworth-Heinemann, Oxford, 1980.

[4] E. Fradkin, Steven A. Kivelson, Michael J. Lawler, James P. Eisenstein, and Andrew P. Mackenzie. Nematic Fermi fluids in condensed matter physics. *Annual Reviews of Condensed Matter Physics*, 1(1):153–178, 2010.

[5] P. Tolédano and J. Tolédano. *The Landau Theory of Phase Transitions*, volume 3. World Scientific Publishing Company, 1987.

[6] J. G. Bednorz and K. A. Müller. Possible high Tc superconductivity in the Ba-La-Cu-O system. *Zeitschrift für Physik B Condensed Matter*, 64(2):189–193, 1986.

[7] K. von Klitzing, G. Dorda, and M. Pepper. New method for high-accuracy determination of the fine-structure constant based on quantized Hall resistance. *Physical Review Letters*, 45(6):494, 1980.

[8] Robert B. Laughlin. Anomalous quantum Hall effect: an incompressible quantum fluid with fractionally charged excitations. *Physical Review Letters*, 50(18):1395, 1983.

[9] Patrick A. Lee, N. Nagaosa, and X. G. Wen. Doping a Mott insulator: Physics of high-temperature superconductivity. *Reviews of Modern Physics*, 78(1):17, 2006.

[10] Y. L. Chen, James G. Analytis, J. H. Chu, Z. K. Liu, S. K. Mo, X. L. Qi, H. J. Zhang, D. H. Lu, X. Dai, Z. Fang, et al. Experimental realization of a three-dimensional topological insulator Bi2Te3. *Science*, 325(5937):178–181, 2009.

[11] Y. Cao, V. Fatemi, A. Demir, S. Fang, Spencer L. Tomarken, Jason Y. Luo, Javier D. Sanchez-Yamagishi, K. Watanabe, T. Taniguchi, E. Kaxiras, et al. Correlated insulator behaviour at half-filling in magic-angle graphene superlattices. *Nature*, 556(7699):80–84, 2018.

[12] Y. Cao, V. Fatemi, S. Fang, K. Watanabe, T. Taniguchi, E. Kaxiras, and P. Jarillo-Herrero. Unconventional superconductivity in magic-angle graphene superlattices. *Nature*, 556(7699):43–50, 2018.

[13] B. Keimer and J. E. Moore. The physics of quantum materials. *Nature Physics*, 13(11):1045–1055, 2017.

[14] D. N. Basov, R. D. Averitt, and D. Hsieh. Towards properties on demand in quantum materials. *Nature Materials*, 16(11):1077–1088, 2017.

[15] Y. Tokura, M. Kawasaki, and N. Nagaosa. Emergent functions of quantum materials. *Nature Physics*, 13(11):1056–1068, 2017.

[16] M. Gibertini, M. Koperski, Alberto F. Morpurgo, and Konstantin S. Novoselov. Magnetic 2D materials and heterostructures. *Nature Nanotechnology*, 14(5):408–419, 2019.

[17] Dante M. Kennes, M. Claassen, L. Xian, A. Georges, Andrew J. Millis, J. Hone, Cory R. Dean, D. N. Basov, Abhay N. Pasupathy, and A. Rubio. Moiré heterostructures as a condensed-matter quantum simulator. *Nature Physics*, 17(2):155–163, 2021.

[18] Y. Ahn, X. Guo, S. Son, Z. Sun, and L. Zhao. Progress and prospects in two-dimensional magnetism of van der Waals materials. *Progress in Quantum Electronics*, page 100498, 2024.

[19] L. D. Landau and E. M. Lifshitz. *Statistical Physics*. Butterworth-Heinemann, Oxford, 3rd edition, 1980.

[20] P. Phillips. *Advanced Solid State Physics*. Cambridge University Press, 2nd edition, 2012.

[21] Y. Nambu. Quasi-particles and gauge invariance in the theory of superconductivity. *Physical Review*, 117(3):648, 1960.

[22] J. Goldstone. Field theories with superconductor solutions. *Il Nuovo Cimento*, 19:154–164, 1961.

[23] N. D. Mermin. The topological theory of defects in ordered media. *Reviews of Modern Physics*, 51(3):591, 1979.

[24] James P. Sethna. Order parameters, broken symmetry, and topology. *arXiv: cond-mat/9204009v3*, 2009.

[25] W. Jin, E. Drueke, S. Li, A. Admasu, R. Owen, M. Day, K. Sun, S.-W. Cheong, and L. Zhao. Observation of a ferro-rotational order coupled with second-order nonlinear optical fields. *Nature Physics*, 16(1):42–46, 2020.

[26] Bas B. Van Aken, J. P. Rivera, H. Schmid, and M. Fiebig. Observation of ferrotoroidic domains. *Nature*, 449(7163):702–705, 2007.

[27] Anne S. Zimmermann, D. Meier, and M. Fiebig. Ferroic nature of magnetic toroidal order. *Nature Communications*, 5(1):4796, 2014.

[28] J. M. Carpenter and C.-K. Loong. Chapter 12: Magnetic scattering: Structures. In *Elements of Slow-Neutron Scattering: Basics, Techniques, and Applications*, page 401–429. Cambridge University Press, Cambridge, 2015.

[29] B. Huang, G. Clark, E. Navarro-Moratalla, Dahlia R. Klein, R. Cheng, Kyle L. Seyler, D. Zhong, E. Schmidgall, Michael A. McGuire, David H. Cobden, et al. Layer-dependent ferromagnetism in a van der Waals crystal down to the monolayer limit. *Nature*, 546(7657):270–273, 2017.

[30] Eva Y. Andrei, Dmitri K. Efetov, P. Jarillo-Herrero, Allan H. MacDonald, K. F. Mak, T. Senthil, E. Tutuc, A. Yazdani, and Andrea F. Young. The marvels of moiré materials. *Nature Reviews Materials*, 6(3):201–206, 2021.

[31] Jose L. Lado. Putting a twist on spintronics. *Science*, 374(6571):1048–1049, 2021.

[32] X. Luo, D. Obeysekera, C. Won, S. H. Sung, N. Schnitzer, R. Hovden, S.-W. Cheong, J. Yang, K. Sun, and L. Zhao. Ultrafast modulations and detection of a ferro-rotational charge density wave using time-resolved electric quadrupole second harmonic generation. *Physical Review Letters*, 127(12):126401, 2021.

[33] S. Li, Z. Ye, X. Luo, G. Ye, H. H. Kim, B. Yang, S. Tian, C. Li, H. Lei, Adam W. Tsen, et al. Magnetic-field-induced quantum phase transitions in a van der Waals magnet. *Physical Review X*, 10(1):011075, 2020.

[34] H. Xie, X. Luo, G. Ye, Z. Ye, H. Ge, S. H. Sung, E. Rennich, S. Yan, Y. Fu, S. Tian, et al. Twist engineering of the two-dimensional magnetism in double bilayer chromium triiodide homostructures. *Nature Physics*, 18(1):30–36, 2022.

[35] H. Xie, X. Luo, Z. Ye, Z. Sun, G. Ye, S. H. Sung, H. Ge, S. Yan, Y. Fu, S. Tian, et al. Evidence of non-collinear spin texture in magnetic moiré superlattices. *Nature Physics*, 19(8):1150–1155, 2023.

[36] Robert W. Boyd. *Nonlinear Optics*. Academic Press, Burlington, 3ed edition, 2008.

[37] John D. Jackson. Chapter 7: Plane electromagnetic waves and wave propagation. In *Classical Electrodynamics*. John Wiley & Sons, Hoboken, 3rd edition, 1998.

[38] Robert W. Boyd. Chapter 13: Ultrafast and intense-field nonlinear optics. In *Nonlinear Optics*, pages 561–587. Academic Press, Burlington, 3ed edition, 2008.

[39] N. W. Ashcroft and N. D. Mermin. Surface effects. In *Solid State Physics*, pages 353–372. Harcourt, Orlando, 1976.

[40] Samuel V. Gallego, J. Etxebarria, L. Elcoro, Emre S. Tasci, and J. Manuel Perez-Mato. Automatic calculation of symmetry-adapted tensors in magnetic and non-magnetic materials: a new tool of the Bilbao Crystallographic Server. *Acta Crystallographica Section A: Foundations and Advances*, 75(3):438–447, 2019.

[41] H. Goldstein, Charles P. Poole, and John L. Safko. Chapter 4: The kinematics of rigid body motion. In *Classical Mechanics*, pages 134–183. Pearson, 3rd edition, 2002.

[42] John D. Jackson. Chapter 10: Scattering and diffraction. In *Classical Electrodynamics*. John Wiley & Sons, Hoboken, 3rd edition, 1998.

[43] M. Fiebig, Victor V. Pavlov, and Roman V. Pisarev. Second-harmonic generation as a tool for studying electronic and magnetic structures of crystals. *Journal of the Optical Society of America B*, 22(1):96–118, 2005.

[44] John D. Jackson. Chapter 9: Radiating systems, multipole fields and radiation. In *Classical Electrodynamics*. John Wiley & Sons, Hoboken, 3rd edition, 1998.

[45] L. Zhao, D. Torchinsky, J. Harter, A. de la Torre, and D. Hsieh. Second harmonic generation spectroscopy of hidden phases. In *Encyclopedia of Modern Optics*, pages 207–226. Elsevier, Oxford, 2nd edition, 2018.

[46] W. Hayes and R. Loudon. *Scattering of Light by Crystals*. John Wiley and Sons, 1978.

[47] John D. Jackson. Chapter 6: Maxwell equations, macroscopic electromagnetism, conservation laws. In *Classical Electrodynamics*. John Wiley & Sons, Hoboken, 3rd edition, 1998.

[48] Mois I. Aroyo, J. M. Perez-Mato, D. Orobengoa, E. Tasci, G. de la Flor, and A. Kirov. Crystallography online: Bilbao crystallographic server. *Bulgarian Chemical Communications*, 43(2):183–197, 2011.

[49] A. Yariv and P. Yeh. Chapter 4: Electromagnetic propagation in anisotropic media. In *Optical Waves in Crystals: Propagation and Control of Laser Radiation*, pages 69–120. John Wiley & Sons, New York, 1984.

[50] M. Born and E. Wolf. Chapter XV: Optics of crystals. In *Principles of Optics*, pages 790–852. Cambridge University Press, Cambridge, 7th edition, 2019.

[51] L. D. Landau and E. M. Lifshitz. Chapter IX - The electromagnetic wave equations. In *Electrodynamics of Continuous Media*, volume 8 of *Course of Theoretical Physics*, pages 257–289. Pergamon, Amsterdam, 2nd edition, 1984.

[52] W. Jin, H. H. Kim, Z. Ye, G. Ye, L. Rojas, X. Luo, B. Yang, F. Yin, J. S. A. Horng, S. Tian, et al. Observation of the polaronic character of excitons in a two-dimensional semiconducting magnet CrI3. *Nature Communications*, 11(1):4780, 2020.

[53] L. D. Landau and E. M. Lifshitz. Chapter XII - Fluctuations. In *Statistical Physics*, pages 333–400. Butterworth-Heinemann, Oxford, 3rd edition, 1980.

[54] J. A. Wilson, F. J. Di Salvo, and S. Mahajan. Charge-density waves and superlattices in the metallic layered transition metal dichalcogenides. *Advances in Physics*, 24(2):117–201, 1975.

[55] C. B. Scruby, P. M. Williams, and G. S. Parry. The role of charge density waves in structural transformations of 1T TaS2. *The Philosophical Magazine: A Journal of Theoretical Experimental and Applied Physics*, 31(2):255–274, 1975.

[56] P. Fazekas and E. Tosatti. Electrical, structural and magnetic properties of pure and doped 1T-TaS2. *Philosophical Magazine B*, 39(3):229–244, 1979.

[57] S. C. Bayliss, A. M. Ghorayeb, and D. R. P. Guy. Thermal and transport evidence for a phase transition in 1T-TaS2 observed at 282K upon warming. *Journal of Physics C: Solid State Physics*, 17(21):L533, 1984.

[58] R. E. Thomson, U. Walter, E. Ganz, J. Clarke, A. Zettl, P. Rauch, and F. J. Di Salvo. Local charge-density-wave structure in 1T-TaS2 determined by scanning tunneling microscopy. *Physical Review B*, 38:10734–10743, 1988.

[59] F. J. Di Salvo, J. A. Wilson, B. G. Bagley, and J. V. Waszczak. Effects of doping on charge-density waves in layer compounds. *Physical Review B*, 12:2220–2235, 1975.

[60] B. Sipos, A. F. Kusmartseva, A. Akrap, H. Berger, L. Forró, and E. Tutiš. From Mott state to superconductivity in 1T-TaS2. *Nature Materials*, 7(12):960–965, 2008.

[61] T. Ritschel, J. Trinckauf, G. Garbarino, M. Hanfland, M. v. Zimmermann, H. Berger, B. Büchner, and J. Geck. Pressure dependence of the charge density wave in 1T-TaS2 and its relation to superconductivity. *Physical Review B*, 87:125135, 2013.

[62] A. W. Tsen, R. Hovden, D. Wang, Y. D. Kim, J. Okamoto, K. A. Spoth, Y. Liu, W. Lu, Y. Sun, J. C. Hone, et al. Structure and control of charge density waves in two-dimensional 1T-TaS2. *Proceedings of the National Academy of Sciences*, 112(49):15054–15059, 2015.

[63] E. Tosatti and P. Fazekas. On the nature of the low-temperature phase of 1T-TaS2. *Le Journal de Physique Colloques*, 37(C4):C4–165, 1976.

[64] P. Fazekas and E. Tosatti. Charge carrier localization in pure and doped 1T-TaS2. *Physica B+C*, 99(1):183–187, 1980.

[65] L. Li, W. Lu, X. Zhu, L. Ling, Z. Qu, and Y. Sun. Fe-doping–induced superconductivity in the charge-density-wave system 1T-TaS2. *Europhysics Letters*, 97(6):67005, 2012.

[66] R. Ang, Y. Tanaka, E. Ieki, K. Nakayama, T. Sato, L. Li, W. Lu, Y. Sun, and T. Takahashi. Real-space coexistence of the melted Mott state and superconductivity in Fe-substituted 1T-TaS2. *Physical Review Letters*, 109(17):176403, 2012.

[67] Y. Liu, R. Ang, W. Lu, W. Song, L. Li, and Y. Sun. Superconductivity induced by Se-doping in layered charge-density-wave system 1T-TaS2-xSex. *Applied Physics Letters*, 102(19), 2013.

[68] Q. Dong, Q. Li, S. Li, X. Shi, S. Niu, S. Liu, R. Liu, B. Liu, X. Luo, J. Si, et al. Structural phase transition and superconductivity hierarchy in 1T-TaS2 under pressure up to 100 GPa. *npj Quantum Materials*, 6(1):20, 2021.

[69] D. Shao, R. Xiao, W. Lu, H. Lv, J. Li, X. Zhu, and Y. Sun. Manipulating charge density waves in 1T-TaS2 by charge-carrier doping: A first-principles investigation. *Physical Review B*, 94:125126, 2016.

[70] M. Kratochvilova, Adrian D. Hillier, Andrew R. Wildes, L. Wang, S.-W. Cheong, and J.-G. Park. The low-temperature highly correlated quantum phase in the charge-density-wave 1T-TaS2 compound. *npj Quantum Materials*, 2(1):42, 2017.

[71] K. T. Law and Patrick A. Lee. 1T-TaS2 as a quantum spin liquid. *Proceedings of the National Academy of Sciences*, 114(27):6996–7000, 2017.

[72] M. Klanjšek, A. Zorko, R. Žitko, J. Mravlje, Z. Jagličić, P. K. Biswas, P. Prelovšek, D. Mihailovic, and D. Arčon. A high-temperature quantum spin liquid with polaron spins. *Nature Physics*, 13(11):1130–1134, 2017.

[73] A. Ribak, I. Silber, C. Baines, K. Chashka, Z. Salman, Y. Dagan, and A. Kanigel. Gapless excitations in the ground state of 1T-TaS2. *Physical Review B*, 96:195131, 2017.

[74] Y. J. Yu, Y. Xu, L. P. He, M. Kratochvilova, Y. Y. Huang, J. M. Ni, L. Wang, S.-W. Cheong, J.-G. Park, and S. Y. Li. Heat transport study of the spin liquid candidate 1T-TaS2. *Physical Review B*, 96:081111, 2017.

[75] S. Mañas-Valero, Benjamin M. Huddart, T. Lancaster, E. Coronado, and Francis L. Pratt. Quantum phases and spin liquid properties of 1T-TaS2. *npj Quantum Materials*, 6(1):69, 2021.

[76] A. Zong. Ultrafast manipulation of mirror domains in 1T-TaS2. In *Emergent States in Photoinduced Charge-Density-Wave Transitions*, pages 193–216. Springer International Publishing, Cham, 2021.

[77] L. Stojchevska, I. Vaskivskyi, T. Mertelj, P. Kusar, D. Svetin, S. Brazovskii, and D. Mihailovic. Ultrafast switching to a stable hidden quantum state in an electronic crystal. *Science*, 344(6180):177–180, 2014.

[78] I. Vaskivskyi, J. Gospodaric, S. Brazovskii, D. Svetin, P. Sutar, E. Goreshnik, Ian A. Mihailovic, T. Mertelj, and D. Mihailovic. Controlling the metal-to-insulator relaxation of the metastable hidden quantum state in 1T-TaS2. *Science Advances*, 1(6):e1500168, 2015.

[79] I. Vaskivskyi, I. A. Mihailovic, S. Brazovskii, J. Gospodaric, T. Mertelj, D. Svetin, P. Sutar, and D. Mihailovic. Fast electronic resistance switching involving hidden charge density wave states. *Nature Communications*, 7(1):11442, 2016.

[80] K. Haupt, M. Eichberger, N. Erasmus, A. Rohwer, J. Demsar, K. Rossnagel, and H. Schwoerer. Ultrafast metamorphosis of a complex charge-density wave. *Physical Review Letters*, 116(1):016402, 2016.

[81] C. Laulhé, T. Huber, G. Lantz, A. Ferrer, Simon O. Mariager, S. Grübel, J. Rittmann, Jeremy A. Johnson, V. Esposito, A. Lübcke, et al. Ultrafast formation of a charge density wave state in 1T-TaS2: Observation at nanometer scales using time-resolved X-ray diffraction. *Physical Review Letters*, 118(24):247401, 2017.

[82] J. Ravnik, I. Vaskivskyi, T. Mertelj, and D. Mihailovic. Real-time observation of the coherent transition to a metastable emergent state in 1T-TaS2. *Physical Review B*, 97(7):075304, 2018.

[83] Yaroslav A. Gerasimenko, P. Karpov, I. Vaskivskyi, S. Brazovskii, and D. Mihailovic. Intertwined chiral charge orders and topological stabilization of the light-induced state of a prototypical transition metal dichalcogenide. *npj Quantum Materials*, 4(1):32, 2019.

[84] A. Zong, A. Kogar, Y. Q. Bie, T. Rohwer, C. Lee, E. Baldini, E. Ergeçen, Mehmet B. Yilmaz, B. Freelon, Edbert J. Sie, et al. Evidence for topological defects in a photoinduced phase transition. *Nature Physics*, 15(1):27–31, 2019.

[85] Th. Pillo, J. Hayoz, H. Berger, M. Grioni, L. Schlapbach, and P. Aebi. Remnant fermi surface in the presence of an underlying instability in layered 1T-TaS2. *Physical Review Letters*, 83:3494–3497, 1999.

[86] X. L. Wu and Charles M. Lieber. Hexagonal domain-like charge density wave phase of TaS2 determined by scanning tunneling microscopy. *Science*, 243(4899):1703–1705, 1989.

[87] A. Spijkerman, Jan L. de Boer, A. Meetsma, Gerrit A. Wiegers, and S. van Smaalen. X-ray crystal-structure refinement of the nearly commensurate phase of 1T-TaS2 in (3+2)-dimensional superspace. *Physical Review B*, 56(21):13757, 1997.

[88] R. E. Thomson, B. Burk, A. Zettl, and J. Clarke. Scanning tunneling microscopy of the charge-density-wave structure in 1T-TaS2. *Phys. Rev. B*, 49:16899–16916, 1994.

[89] R. V. Coleman, B. Drake, P. K. Hansma, and G. Slough. Charge-density waves observed with a tunneling microscope. *Physical Review Letters*, 55(4):394, 1985.

[90] R. A. Pollak, D. E. Eastman, F. J. Himpsel, P. Heimann, and B. Reihl. 1T-TaS2 charge-density-wave metal-insulator transition and Fermi-surface modification observed by photoemission. *Physical Review B*, 24(12):7435, 1981.

[91] N. V. Smith, S. D. Kevan, and F. J. Di Salvo. Band structures of the layer compounds 1T-TaS2 and 2H-TaSe2 in the presence of commensurate charge-density waves. *Journal of Physics C: Solid State Physics*, 18(16):3175, 1985.

[92] G. Grüner. The dynamics of charge-density waves. *Reviews of Modern Physics*, 60(4):1129, 1988.

[93] K Rossnagel. On the origin of charge-density waves in select layered transition-metal dichalcogenides. *Journal of Physics: Condensed Matter*, 23(21):213001, 2011.

[94] Darius H. Torchinsky, F. Mahmood, Anthony T. Bollinger, I. Božović, and N. Gedik. Fluctuating charge-density waves in a cuprate superconductor. *Nature Materials*, 12(5):387–391, 2013.

[95] S. Sugai. Lattice vibrations in the charge-density-wave states of layered transition metal dichalcogenides. *Physica Status Solidi (b)*, 129(1):13–39, 1985.

[96] J. Demsar, L. Forró, H. Berger, and D. Mihailovic. Femtosecond snapshots of gap-forming charge-density-wave correlations in quasi-two-dimensional dichalcogenides 1T-TaS2 and 2H-TaSe2. *Physical Review B*, 66(4):041101, 2002.

[97] T. Onozaki, Y. Toda, S. Tanda, and R. Morita. Coherent double-pulse excitation of charge-density-wave oscillation. *Japanese Journal of Applied Physics*, 46(2R):870, 2007.

[98] M. Eichberger, H. Schäfer, M. Krumova, M. Beyer, J. Demsar, H. Berger, G. Moriena, G. Sciaini, and R. J. Dwayne Miller. Snapshots of cooperative atomic motions in the optical suppression of charge density waves. *Nature*, 468(7325):799–802, 2010.

[99] C. Laulhé, L. Cario, B. Corraze, E. Janod, T. Huber, G. Lantz, S. Boulfaat, A. Ferrer, Simon O. Mariager, Jeremy A. Johnson, et al. X-ray study of femtosecond structural dynamics in the 2D charge density wave compound 1T-TaS2. *Physica B: Condensed Matter*, 460:100–104, 2015.

[100] R. Hovden, P. Liu, N. Schnitzer, Adam W. Tsen, Y. Liu, W. Lu, Y. Sun, and Lena F. Kourkoutis. Thickness and stacking sequence determination of exfoliated dichalcogenides (1T-TaS2, 2H-MoS2) using scanning transmission electron microscopy. *Microscopy and Microanalysis*, 24(4):387–395, 2018.

[101] S. H. Sung, N. Schnitzer, S. Novakov, I. El Baggari, X. Luo, J. Gim, Nguyen M. Vu, Z. Li, Todd H. Brintlinger, Y. Liu, et al. Two-dimensional charge order stabilized in clean polytype heterostructures. *Nature Communications*, 13(1):413, 2022.

[102] J. Hlinka, J. Privratska, P. Ondrejkovic, and V. Janovec. Symmetry guide to ferroaxial transitions. *Physical Review Letters*, 116(17):177602, 2016.

[103] See Supplemental Material in X. Luo, D. Obeysekera, C. Won, S. H. Sung, N. Schnitzer, R. Hovden, S.-W. Cheong, J. Yang, K. Sun, and L. Zhao. Ultrafast modulations and detection of a ferro-rotational charge density wave using time-resolved electric quadrupole second harmonic generation. *Physical Review Letters*, 127(12):126401, 2021.

[104] K. Sun, S. Sun, C. Zhu, H. Tian, H. Yang, and J. Li. Hidden CDW states and insulator-to-metal transition after a pulsed femtosecond laser excitation in layered chalcogenide 1T-TaS2-xSex. *Science Advances*, 4(7):eaas9660, 2018.

[105] K. Nakanishi and H. Shiba. Domain-like incommensurate charge-density-wave states and the first-order incommensurate-commensurate transitions in layered tantalum dichalcogenides. I. 1T-polytype. *Journal of the Physical Society of Japan*, 43(6):1839–1847, 1977.

[106] Oliver R. Albertini, R.i Zhao, Rebecca L. McCann, S. Feng, M. Terrones, James K. Freericks, Joshua A. Robinson, and Amy Y. Liu. Zone-center phonons of bulk, few-layer, and monolayer 1T-TaS2: Detection of commensurate charge density wave phase through Raman scattering. *Physical Review B*, 93(21):214109, 2016.

[107] P. Kusar, T. Mertelj, V. V. Kabanov, J. H. Chu, I. R. Fisher, H. Berger, L. Forró, and D. Mihailovic. Anharmonic order-parameter oscillations and lattice coupling in strongly driven 1T-TaS2 and TbTe3 charge-density-wave compounds: A multiple-pulse femtosecond laser spectroscopy study. *Physical Review B*, 83(3):035104, 2011.

[108] A. Mann, E. Baldini, A. Odeh, A. Magrez, H. Berger, and F. Carbone. Probing the coupling between a doublon excitation and the charge-density wave in TaS2 by ultrafast optical spectroscopy. *Physical Review B*, 94(11):115122, 2016.

[109] A. Zong, X. Shen, A. Kogar, L. Ye, C. Marks, D. Chowdhury, T. Rohwer, B. Freelon, S. Weathersby, R. Li, et al. Ultrafast manipulation of mirror domain walls in a charge density wave. *Science Advances*, 4(10):eaau5501, 2018.

[110] M. Bovet, D. Popović, F. Clerc, C. Koitzsch, U. Probst, E. Bucher, H. Berger, D. Naumović, and P. Aebi. Pseudogapped Fermi surfaces of 1T-TaS2 and 1T-TaSe2: A charge density wave effect. *Physical Review B*, 69(12):125117, 2004.

[111] T. Hirata, Y. Yamakawa, S. Onari, and H. Kontani. Unconventional orbital charge density wave mechanism in the transition metal dichalcogenide 1T-TaS2. *Physical Review Research*, 3(3):L032053, 2021.

[112] Dahlia R. Klein, D. MacNeill, Jose L. Lado, D. Soriano, E. Navarro-Moratalla, K. Watanabe, T. Taniguchi, S. Manni, P. Canfield, J. Fernández-Rossier, et al. Probing magnetism in 2D van der Waals crystalline insulators via electron tunneling. *Science*, 360(6394):1218–1222, 2018.

[113] T. Song, X. Cai, Matisse W.-Y. Tu, X. Zhang, B. Huang, Nathan P. Wilson, Kyle L. Seyler, L. Zhu, T. Taniguchi, K. Watanabe, et al. Giant tunneling magnetoresistance in spin-filter van der Waals heterostructures. *Science*, 360(6394):1214–1218, 2018.

[114] Z. Wang, I. Gutiérrez-Lezama, N. Ubrig, M. Kroner, M. Gibertini, T. Taniguchi, K. Watanabe, A. Imamoğlu, E. Giannini, and Alberto F. Morpurgo. Very large tunneling magnetoresistance in layered magnetic semiconductor CrI3. *Nature Communications*, 9(1):2516, 2018.

[115] H. H. Kim, B. Yang, T. Patel, F. Sfigakis, C. Li, S. Tian, H. Lei, and Adam W. Tsen. One million percent tunnel magnetoresistance in a magnetic van der Waals heterostructure. *Nano Letters*, 18(8):4885–4890, 2018.

[116] Michael A. McGuire, H. Dixit, Valentino R. Cooper, and Brian C. Sales. Coupling of crystal structure and magnetism in the layered, ferromagnetic insulator CrI3. *Chemistry of Materials*, 27(2):612–620, 2015.

[117] L. Chen, J.-H. Chung, B. Gao, T. Chen, Matthew B. Stone, Alexander I. Kolesnikov, Q. Huang, and P. Dai. Topological spin excitations in honeycomb ferromagnet CrI3. *Physical Review X*, 8(4):041028, 2018.

[118] L. Chen, J.-H. Chung, T. Chen, C. Duan, A. Schneidewind, I. Radelytskyi, David J. Voneshen, Russell A. Ewings, Matthew B. Stone, Alexander I. Kolesnikov, et al. Magnetic anisotropy in ferromagnetic CrI3. *Physical Review B*, 101(13):134418, 2020.

[119] J. Cenker, B. Huang, N. Suri, P. Thijssen, A. Miller, T. Song, T. Taniguchi, K. Watanabe, Michael A. McGuire, D. Xiao, et al. Direct observation of two-dimensional magnons in atomically thin CrI3. *Nature Physics*, 17(1):20–25, 2021.

[120] C. Xu, J. Feng, H. Xiang, and L. Bellaiche. Interplay between Kitaev interaction and single ion anisotropy in ferromagnetic CrI3 and CrGeTe3 monolayers. *npj Computational Materials*, 4(1):57, 2018.

[121] I. Lee, Franz G. Utermohlen, D. Weber, K. Hwang, C. Zhang, J. van Tol, Joshua E. Goldberger, N. Trivedi, and P. C. Hammel. Fundamental spin interactions underlying the magnetic anisotropy in the Kitaev ferromagnet CrI3. *Physical Review Letters*, 124(1):017201, 2020.

[122] P. P. Stavropoulos, X. Liu, and H.-Y. Kee. Magnetic anisotropy in spin-3/2 with heavy ligand in honeycomb Mott insulators: Application to CrI3. *Physical Review Research*, 3(1):013216, 2021.

[123] S. A. Owerre. A first theoretical realization of honeycomb topological magnon insulator. *Journal of Physics: Condensed Matter*, 28(38):386001, 2016.

[124] L. Chen, J.-H. Chung, Matthew B. Stone, Alexander I. Kolesnikov, B. Winn, V. O. Garlea, Douglas L. Abernathy, B. Gao, M. Augustin, Elton J. G. Santos, et al. Magnetic field effect on topological spin excitations in CrI3. *Physical Review X*, 11(3):031047, 2021.

[125] W. Jin, H. H. Kim, Z. Ye, S. Li, P. Rezaie, F. Diaz, S. Siddiq, . Wauer, B. Yang, C. Li, et al. Raman fingerprint of two terahertz spin wave branches in a two-dimensional honeycomb Ising ferromagnet. *Nature Communications*, 9(1):5122, 2018.

[126] D. Shcherbakov, P. Stepanov, D. Weber, Y. Wang, J. Hu, Y. Zhu, K. Watanabe, T. Taniguchi, Z. Mao, W. Windl, et al. Raman spectroscopy, photocatalytic degradation, and stabilization of atomically thin chromium tri-iodide. *Nano Letters*, 18(7):4214–4219, 2018.

[127] S. Djurdjić-Mijin, A. Šolajić, J. Pešić, M. Šćepanović, Y. Liu, A. Baum, C. Petrovic, N. Lazarević, Z. V. Popović, et al. Lattice dynamics and phase transition in CrI3 single crystals. *Physical Review B*, 98(10):104307, 2018.

[128] P. Tolédano and J. Tolédano. The Landau theory of magnetic phase transitions. In *The Landau Theory of Phase Transitions*, volume 3, pages 307–373. World Scientific Publishing Company, 1987.

[129] See Supplemental Material in S. Li, Z. Ye, X. Luo, G. Ye, H. H. Kim, B. Yang, S. Tian, C. Li, H. Lei, Adam W. Tsen, et al. Magnetic-field-induced quantum phase transitions in a van der Waals magnet. *Physical Review X*, 10(1):011075, 2020.

[130] B. Niu, T. Su, Brian A. Francisco, S. Ghosh, F. Kargar, X. Huang, M. Lohmann, J. Li, Y. Xu, T. Taniguchi, et al. Coexistence of magnetic orders in two-dimensional magnet CrI3. *Nano Letters*, 20(1):553–558, 2019.

[131] David C. Johnston. Magnetic dipole interactions in crystals. *Physical Review B*, 93(1):014421, 2016.

[132] A. Altland and B. Simons. Second quantization. In *Condensed Matter Field Theory*, pages 40—-90. Cambridge University Press, 2023.

[133] R. P. Silberstein, L. E. Schmutz, V.J. Tekippe, M. S. Dresselhaus, and R. L. Aggarwal. Magnetic phase-dependent Raman scattering in EuSe and EuTe. *Solid State Communications*, 18(9-10):1173–1177, 1976.

[134] R. P. Silberstein, V. J. Tekippe, and M. S. Dresselhaus. Magnetic phase-dependent Raman scattering in EuS and EuSe. *Physical Review B*, 16(6):2728, 1977.

[135] Y. Ousaka, O. Sakai, and M. Tachiki. Theory of Raman scattering in magnetically ordered phases of EuSe and EuTe. *Solid State Communications*, 23(8):589–592, 1977.

[136] S. A. Safran, B. Lax, and G. Dresselhaus. Phenomenological theory of Raman scattering in europium chalcogenides. *Solid State Communications*, 19(12):1217–1220, 1976.

[137] G. Güntherodt. Light scattering in magnetic semiconductors. *Journal of Magnetism and Magnetic Materials*, 11(1-3):394–402, 1979.

[138] G. Güntherodt and R. Merlin. Raman scattering in rare-earth chalcogenides. In *Light Scattering in Solids IV: Electronics Scattering, Spin Effects, SERS, and Morphic Effects*, pages 243–287. Springer Berlin Heidelberg, Berlin, Heidelberg, 1984.

[139] N. Sivadas, S. Okamoto, X. Xu, Craig J. Fennie, and D. Xiao. Stacking-dependent magnetism in bilayer CrI3. *Nano Letters*, 18(12):7658–7664, 2018.

[140] Paul M. Chaikin, Tom C. Lubensky, and Thomas A. Witten. *Principles of Condensed Matter Physics*, volume 10. Cambridge University Press, Cambridge, 1995.

[141] M. Yankowitz, S. Chen, H. Polshyn, Y. Zhang, K. Watanabe, T. Taniguchi, D. Graf, Andrea F. Young, and Cory R. Dean. Tuning superconductivity in twisted bilayer graphene. *Science*, 363(6431):1059–1064, 2019.

[142] X. Lu, P. Stepanov, W. Yang, M. Xie, M. A. Aamir, I. Das, C. Urgell, K. Watanabe, T. Taniguchi, G. Zhang, et al. Superconductors, orbital magnets and correlated states in magic-angle bilayer graphene. *Nature*, 574(7780):653–657, 2019.

[143] Z. Zhang, Y. Wang, K. Watanabe, T. Taniguchi, K. Ueno, E. Tutuc, and Brian J. LeRoy. Flat bands in twisted bilayer transition metal dichalcogenides. *Nature Physics*, 16(11):1093–1096, 2020.

[144] Emma C. Regan, D. Wang, C. Jin, M. I. Bakti Utama, B. Gao, X. Wei, S. Zhao, W. Zhao, Z. Zhang, K. Yumigeta, et al. Mott and generalized Wigner crystal states in WSe2/WS2 moiré superlattices. *Nature*, 579(7799):359–363, 2020.

[145] Y. Tang, L. Li, T. Li, Y. Xu, S. Liu, K. Barmak, K. Watanabe, T. Taniguchi, Allan H. MacDonald, J. Shan, et al. Simulation of Hubbard model physics in WSe2/WS2 moiré superlattices. *Nature*, 579(7799):353–358, 2020.

[146] L. Balents, Cory R. Dean, Dmitri K. Efetov, and Andrea F. Young. Superconductivity and strong correlations in moiré flat bands. *Nature Physics*, 16(7):725–733, 2020.

[147] L. Wang, E.-M. Shih, A. Ghiotto, L. Xian, Daniel A. Rhodes, C. Tan, M. Claassen, Dante M. Kennes, Y. Bai, B. Kim, et al. Correlated electronic phases in twisted bilayer transition metal dichalcogenides. *Nature Materials*, 19(8):861–866, 2020.

[148] F. Wu, T. Lovorn, E. Tutuc, I. Martin, and A. H. MacDonald. Topological insulators in twisted transition metal dichalcogenide homobilayers. *Physical Review Letters*, 122(8):086402, 2019.

[149] Aaron L. Sharpe, Eli J. Fox, Arthur W. Barnard, J. Finney, K. Watanabe, T. Taniguchi, M. A. Kastner, and D. Goldhaber-Gordon. Emergent ferromagnetism near three-quarters filling in twisted bilayer graphene. *Science*, 365(6453):605–608, 2019.

[150] M. Serlin, C. L. Tschirhart, H. Polshyn, Y. Zhang, J. Zhu, K. Watanabe, T. Taniguchi, L. Balents, and A. F. Young. Intrinsic quantized anomalous Hall effect in a moiré heterostructure. *Science*, 367(6480):900–903, 2020.

[151] Kevin P. Nuckolls, M. Oh, D. Wong, B. Lian, K. Watanabe, T. Taniguchi, B. Andrei Bernevig, and A. Yazdani. Strongly correlated Chern insulators in magic-angle twisted bilayer graphene. *Nature*, 588(7839):610–615, 2020.

[152] G. Chen, Aaron L. Sharpe, Eli J. Fox, Y.-H. Zhang, S. Wang, L. Jiang, B. Lyu, H. Li, K. Watanabe, T. Taniguchi, et al. Tunable correlated Chern insulator and ferromagnetism in a moiré superlattice. *Nature*, 579(7797):56–61, 2020.

[153] S. Wu, Z. Zhang, K. Watanabe, T. Taniguchi, and Eva Y. Andrei. Chern insulators, van Hove singularities and topological flat bands in magic-angle twisted bilayer graphene. *Nature Materials*, 20(4):488–494, 2021.

[154] Kyle L. Seyler, P. Rivera, H. Yu, Nathan P. Wilson, Essance L. Ray, David G. Mandrus, J. Yan, W. Yao, and X. Xu. Signatures of moiré-trapped valley excitons in MoSe2/WSe2 heterobilayers. *Nature*, 567(7746):66–70, 2019.

[155] K. Tran, G. Moody, F. Wu, X. Lu, J. Choi, K. Kim, A. Rai, Daniel A. Sanchez, J. Quan, A. Singh, et al. Evidence for moiré excitons in van der Waals heterostructures. *Nature*, 567(7746):71–75, 2019.

[156] C. Jin, Emma C. Regan, A. Yan, M. Iqbal Bakti Utama, D. Wang, S. Zhao, Y. Qin, S. Yang, Z. Zheng, S. Shi, et al. Observation of moiré excitons in WSe2/WS2 heterostructure superlattices. *Nature*, 567(7746):76–80, 2019.

[157] Y. Shimazaki, I. Schwartz, K. Watanabe, T. Taniguchi, M. Kroner, and A. Imamoğlu. Strongly correlated electrons and hybrid excitons in a moiré heterostructure. *Nature*, 580(7804):472–477, 2020.

[158] Evgeny M. Alexeev, David A. Ruiz-Tijerina, M. Danovich, Matthew J. Hamer, Daniel J. Terry, Pramoda K. Nayak, S. Ahn, S. Pak, J. Lee, J. I. Sohn, et al. Resonantly hybridized excitons in moiré superlattices in van der Waals heterostructures. *Nature*, 567(7746):81–86, 2019.

[159] Q. Tong, F. Liu, J. Xiao, and W. Yao. Skyrmions in the Moiré of van der Waals 2D magnets. *Nano Letters*, 18(11):7194–7199, 2018.

[160] Y.-H. Li and R. Cheng. Moiré magnons in twisted bilayer magnets with collinear order. *Physical Review B*, 102(9):094404, 2020.

[161] K. Hejazi, Z.-X. Luo, and L. Balents. Noncollinear phases in moiré magnets. *Proceedings of the National Academy of Sciences*, 117(20):10721–10726, 2020.

[162] M. Akram, H. LaBollita, D. Dey, J. Kapeghian, O. Erten, and Antia S. Botana. Moiré skyrmions and chiral magnetic phases in twisted CrX3 (X= I, Br, and Cl) bilayers. *Nano Letters*, 21(15):6633–6639, 2021.

[163] K. Hejazi, Z.-X. Luo, L. Balents, et al. Heterobilayer moiré magnets: Moiré skyrmions and commensurate-incommensurate transitions. *Physical Review B*, 104(10):L100406, 2021.

[164] X. Li and J. Yang. First-principles design of spintronics materials. *National Science Review*, 3(3):365–381, 2016.

[165] K. F. Mak, J. Shan, and Daniel C. Ralph. Probing and controlling magnetic states in 2D layered magnetic materials. *Nature Reviews Physics*, 1(11):646–661, 2019.

[166] X. Jiang, Q. Liu, J. Xing, N. Liu, Y. Guo, Z. Liu, and J. Zhao. Recent progress on 2D magnets: Fundamental mechanism, structural design and modification. *Applied Physics Reviews*, 8(3), 2021.

[167] M. Hossain, B. Qin, B. Li, and X. Duan. Synthesis, characterization, properties and applications of two-dimensional magnetic materials. *Nano Today*, 42:101338, 2022.

[168] E. Elahi, G. Dastgeer, G. Nazir, S. Nisar, M. Bashir, H. A. Qureshi, D. Kim, J. Aziz, M. Aslam, K. Hussain, et al. A review on two-dimensional (2D) magnetic materials and their potential applications in spintronics and spin-caloritronic. *Computational Materials Science*, 213:111670, 2022.

[169] David D. Awschalom, C. R. Du, R. He, F. Joseph Heremans, A. Hoffmann, J. Hou, H. Kurebayashi, Y. Li, L. Liu, V. Novosad, et al. Quantum engineering with hybrid magnonic systems and materials. *IEEE Transactions on Quantum Engineering*, 2:1–36, 2021.

[170] W. Jin, Z. Ye, X. Luo, B. Yang, G. Ye, F. Yin, H. H. Kim, L. Rojas, S. Tian, Y. Fu, et al. Tunable layered-magnetism–assisted magneto-Raman effect in a two-dimensional magnet CrI3. *Proceedings of the National Academy of Sciences*, 117(40):24664–24669, 2020.

[171] B. Huang, J. Cenker, X. Zhang, Essance L. Ray, T. Song, T. Taniguchi, K. Watanabe, Michael A. McGuire, D. Xiao, and X. Xu. Tuning inelastic light scattering via symmetry control in the two-dimensional magnet CrI3. *Nature Nanotechnology*, 15(3):212–216, 2020.

[172] Y. Zhang, X. Wu, B. Lyu, M. Wu, S. Zhao, J. Chen, M. Jia, C. Zhang, L. Wang, X. Wang, et al. Magnetic order-induced polarization anomaly of Raman scattering in 2D magnet CrI3. *Nano Letters*, 20(1):729–734, 2019.

[173] J. F. Dillon Jr and C. E. Olson. Magnetization, resonance, and optical properties of the ferromagnet CrI3. *Journal of Applied Physics*, 36(3):1259–1260, 1965.

[174] D. Wang and B. Sanyal. Systematic study of monolayer to trilayer CrI3: Stacking sequence dependence of electronic structure and magnetism. *The Journal of Physical Chemistry C*, 125(33):18467–18473, 2021.

[175] H. Wang, F. Fan, S. Zhu, and H. Wu. Doping enhanced ferromagnetism and induced half-metallicity in CrI3 monolayer. *Europhysics Letters*, 114(4):47001, 2016.

[176] John B. Goodenough. Theory of the role of covalence in the perovskite-type manganites [La, M(II)]MnO3. *Physical Review*, 100(2):564, 1955.

[177] John B. Goodenough. An interpretation of the magnetic properties of the perovskite-type mixed crystals La1-xSrxCoO3-λ. *Journal of Physics and Chemistry of Solids*, 6(2-3):287–297, 1958.

[178] J. Kanamori. Superexchange interaction and symmetry properties of electron orbitals. *Journal of Physics and Chemistry of Solids*, 10(2):87–98, 1959.

[179] P. Jiang, C. Wang, D. Chen, Z. Zhong, Z. Yuan, Z.-Y. Lu, and W. Ji. Stacking tunable interlayer magnetism in bilayer CrI3. *Physical Review B*, 99(14):144401, 2019.

[180] S. W. Jang, M. Y. Jeong, H. Yoon, S. Ryee, and M. J. Han. Microscopic understanding of magnetic interactions in bilayer CrI3. *Physical Review Materials*, 3(3):031001, 2019.

[181] D. Soriano, C. Cardoso, and J. Fernández-Rossier. Interplay between interlayer exchange and stacking in CrI3 bilayers. *Solid State Communications*, 299:113662, 2019.

[182] K. W. Song. Interlayer superexchange in bilayer chromium trihalides. *Physical Review B*, 107(24):245133, 2023.

[183] S. Jiang, L. Li, Z. Wang, K. F. Mak, and J. Shan. Controlling magnetism in 2D CrI3 by electrostatic doping. *Nature Nanotechnology*, 13(7):549–553, 2018.

[184] H. H. Kim, B. Yang, S. Li, S. Jiang, C. Jin, Z. Tao, G. Nichols, F. Sfigakis, S. Zhong, C. Li, et al. Evolution of interlayer and intralayer magnetism in three atomically thin chromium trihalides. *Proceedings of the National Academy of Sciences*, 116(23):11131–11136, 2019.

[185] A. McCreary, Thuc T. Mai, Franz G. Utermohlen, Jeffrey R. Simpson, Kevin F. Garrity, X. Feng, D. Shcherbakov, Y. Zhu, J. Hu, D. Weber, et al. Distinct magneto-Raman signatures of spin-flip phase transitions in CrI3. *Nature Communications*, 11(1):3879, 2020.

[186] M. Staiger, R. Gillen, N. Scheuschner, O. Ochedowski, F. Kampmann, M. Schleberger, C. Thomsen, and J. Maultzsch. Splitting of monolayer out-of-plane A' Raman mode in few-layer WS2. *Physical Review B*, 91(19):195419, 2015.

[187] Q. J. Song, Q. H. Tan, X. Zhang, J. B. Wu, B. W. Sheng, Y. Wan, X. Q. Wang, L. Dai, and P. H. Tan. Physical origin of Davydov splitting and resonant Raman spectroscopy of Davydov components in multilayer MoTe2. *Physical Review B*, 93(11):115409, 2016.

[188] G. Froehlicher, E. Lorchat, F. Fernique, C. Joshi, A. Molina-Sánchez, L. Wirtz, and S. Berciaud. Unified description of the optical phonon modes in N-layer MoTe2. *Nano Letters*, 15(10):6481–6489, 2015.

[189] K. Kim, J.-U. Lee, D. Nam, and H. Cheong. Davydov splitting and excitonic resonance effects in Raman spectra of few-layer MoSe2. *ACS Nano*, 10(8):8113–8120, 2016.

[190] T. Song, Q.-C. Sun, E. Anderson, C. Wang, J. Qian, T. Taniguchi, K. Watanabe, Michael A. McGuire, R. Stöhr, D. Xiao, et al. Direct visualization of magnetic domains and moiré magnetism in twisted 2D magnets. *Science*, 374(6571):1140–1144, 2021.

[191] C. Kittel and P. McEuen. Chapter 11: Diamagnetism and paramagnetism. In *Introduction to Solid State Physics*, pages 297–317. John Wiley & Sons, Hoboken, 8th edition, 2005.

[192] Manfred Fiebig. Order! Order!! *Nature Physics*, 16(1):9–10, 2020.

[193] Robert W. Boyd. Chapter 2: Wave-equation description of nonlinear optical interactions. In *Nonlinear Optics*, pages 69–134. Academic Press, Burlington, 3ed edition, 2008.

[194] J. E. Sipe and A. I. Shkrebtii. Second-order optical response in semiconductors. *Physical Review B*, 61(8):5337, 2000.

[195] J. Orenstein, J. E. Moore, T. Morimoto, D. H. Torchinsky, J. W. Harter, and D. Hsieh. Topology and symmetry of quantum materials via nonlinear optical responses. *Annual Review of Condensed Matter Physics*, 12:247–272, 2021.

[196] Q. Ma, Adolfo G. Grushin, and Kenneth S. Burch. Topology and geometry under the nonlinear electromagnetic spotlight. *Nature Materials*, 20(12):1601–1614, 2021.

[197] H. Yokota, T. Hayashida, D. Kitahara, and T. Kimura. Three-dimensional imaging of ferroaxial domains using circularly polarized second harmonic generation microscopy. *npj Quantum Materials*, 7(1):106, 2022.

[198] X. Guo, R. Owen, A. Kaczmarek, X. Fang, C. De, Y. Ahn, W. Hu, N. Agarwal, S. H. Sung, R. Hovden, et al. Ferrorotational domain walls revealed by electric quadrupole second harmonic generation microscopy. *Physical Review B*, 107(18):L180102, 2023.

[199] L. Thiel, Z. Wang, Märta A. Tschudin, D. Rohner, I. Gutiérrez-Lezama, N. Ubrig, M. Gibertini, E. Giannini, Alberto F. Morpurgo, and P. Maletinsky. Probing magnetism in 2D materials at the nanoscale with single-spin microscopy. *Science*, 364(6444):973–976, 2019.

[200] M. Huang, Z. Sun, G. Yan, H. Xie, N. Agarwal, G. Ye, S. H. Sung, H. Lu, J. Zhou, S. Yan, et al. Revealing intrinsic domains and fluctuations of moiré magnetism by a wide-field quantum microscope. *Nature Communications*, 14(1):5259, 2023.

[201] M. Akram and O. Erten. Skyrmions in twisted van der Waals magnets. *Physical Review B*, 103(14):L140406, 2021.

[202] D. Ghader, B. Jabakhanji, and A. Stroppa. Whirling interlayer fields as a source of stable topological order in moiré CrI3. *Communications Physics*, 5(1):192, 2022.

[203] K. M. Kim, D. H. Kiem, G. Bednik, M. J. Han, and M. J. Park. Theory of moire magnets and topological magnons: Applications to twisted bilayer CrI3. *arXiv: 2206.05264*, 2022.

[204] H. Yoo, R. Engelke, S. Carr, S. Fang, K. Zhang, P. Cazeaux, S. H. Sung, R. Hovden, Adam W. Tsen, T. Taniguchi, et al. Atomic and electronic reconstruction at the van der Waals interface in twisted bilayer graphene. *Nature Materials*, 18(5):448–453, 2019.

[205] A. Weston, Y. Zou, V. Enaldiev, A. Summerfield, N. Clark, V. Zólyomi, A. Graham, C. Yelgel, S. Magorrian, M. Zhou, et al. Atomic reconstruction in twisted bilayers of transition metal dichalcogenides. *Nature Nanotechnology*, 15(7):592–597, 2020.

[206] Nathanael P. Kazmierczak, M. Van Winkle, C. Ophus, Karen C. Bustillo, S. Carr, Hamish G. Brown, J. Ciston, T. Taniguchi, K. Watanabe, and D. K. Bediako. Strain fields in twisted bilayer graphene. *Nature Materials*, 20(7):956–963, 2021.

[207] H. Li, S. Li, Mit H. Naik, J. Xie, X. Li, J. Wang, E. Regan, D. Wang, W. Zhao, S. Zhao, et al. Imaging moiré flat bands in three-dimensional reconstructed WSe2/WS2 superlattices. *Nature Materials*, 20(7):945–950, 2021.

[208] S. H. Sung, Y. M. Goh, H. Yoo, R. Engelke, H. Xie, K. Zhang, Z. Li, A. Ye, Parag B. Deotare, Ellad B. Tadmor, et al. Torsional periodic lattice distortions and diffraction of twisted 2D materials. *Nature Communications*, 13(1):7826, 2022.

[209] Igor Mazin and PRX Editors. Altermagnetism—a new punch line of fundamental magnetism. *Physical Review X*, 12(4):040002, 2022.

[210] L. Allen, Marco W. Beijersbergen, R. J. C. Spreeuw, and J. P. Woerdman. Orbital angular momentum of light and the transformation of Laguerre-Gaussian laser modes. *Physical Rreview A*, 45(11):8185, 1992.